

**Multimodal Investigation of The Efficiency and Stability of Microstimulation
Using Electrodes Coated with PEDOT/CNT and Iridium Oxide**

by

Xin Sally Zheng

Biomedical Engineering B.S., Illinois Institute of Technology, 2013

Biomedical Engineering M.S.E., University of Michigan – Ann Arbor, 2014

Submitted to the Graduate Faculty of the
Swanson School of Engineering in partial fulfillment
of the requirements for the degree of
Doctor of Philosophy

University of Pittsburgh

2021

UNIVERSITY OF PITTSBURGH

SWANSON SCHOOL OF ENGINEERING

This dissertation was presented

by

Xin Sally Zheng, Ph.D

It was defended on

January 26, 2021

and approved by

Takashi Kozai, PhD, Assistant Professor, Department of Bioengineering

Lee Fisher, PhD, Assistant Professor, Department of Physical Medicine and Rehabilitation

Robert Turner, PhD, Professor, Department of Bioengineering

Alberto Vasquez, PhD, Research Associate Professor, Department of Radiology

Dissertation Director: Tracy Cui, PhD, Professor, Department of Bioengineering

Copyright © by Xin Sally Zheng

2021

Multimodal Investigation of the Efficiency and Stability of Microstimulation Using Electrodes Coated with PEDOT/CNT and Iridium Oxide

Xin Sally Zheng, PhD

University of Pittsburgh, 2021

Electrical microstimulation is an invaluable tool in neuroscience research to dissect neural circuits, relate brain areas, and identify relationships between brain structure and behavior. In the clinic, electrical microstimulation has enabled partial restoration of vision, movement, sensation and autonomic functions. Recently, novel materials and new fabrication techniques of traditional metals have emerged such as iridium oxide and the conducting polymer PEDOT/CNT. These materials have demonstrated particular promise in the improvement in electrical efficiency. However, the *in vivo* stimulation efficiency and the *in vivo* stability of these materials have not been thoroughly characterized. In this dissertation, we use a multimodal approach to study the efficiency and stability of electrode-tissue interface using novel materials in microstimulation.

Table of Contents

Acknowledgement	xiv
1.0 Introduction.....	1
1.1 Microelectrode Materials for Chronic Electrical Microstimulation	1
1.1.1 Mechanism of Electrical Stimulation	3
1.1.1.1 Activation of Neural Tissue.....	3
1.1.1.2 Faradaic versus Non-Faradaic Charge Transfer.....	4
1.2 Challenges in Chronic Microstimulation	5
1.2.1 Charge Injection Limit	6
1.2.2 Stimulation Induced Adverse Biological Responses	6
1.2.3 Material Stability	8
1.3 Testing Methods of Stimulating Electrodes	9
1.3.1 Electrochemical Methods	9
1.3.1.1 Cyclic Voltammetry	9
1.3.1.2 Electrochemical Impedance Spectroscopy	11
1.3.1.3 Voltage Transient.....	12
1.3.1.4 Equivalent Circuit Modeling	13
1.3.2 Tests for Evaluating Chemical and Mechanical Integrity	16
1.3.3 Thermal Accelerated Aging Test	17
1.3.4 <i>In vitro</i> Electrical Stimulation Test.....	20
1.3.5 Biological Testing	21
1.3.5.1 <i>In vitro</i>	21

1.3.5.2	Histology	22
1.3.5.3	Electrophysiology	22
1.3.5.4	Live Imaging.....	23
1.4	Material Development for Stable Electrical Stimulation.....	25
1.4.1	Metal Materials	25
1.4.2	Conducting Polymer	32
1.4.2.1	Methods to Improve Conducting Polymer (CP) Adhesion	33
1.4.2.1.1	Substrates	33
1.4.2.1.2	Solvents	34
1.4.2.1.3	Dopants	34
1.4.2.2	Drug Delivery to Improve Stimulation Stability.....	37
1.4.3	Carbon Materials	41
1.5	Dissertation Organization.....	51
2.0	Imaging the Efficiency of PEDOT/CNT and Iridium Oxide Electrode Coatings for Microstimulation.....	53
2.1	Chapter Overview	53
2.2	Introduction	54
2.3	Materials and Methods	56
2.3.1	Electrode modification.....	56
2.3.2	Electrochemical characterization of modified electrodes.....	57
2.3.3	Animal Surgery	58
2.3.4	Imaging and electrical stimulation	58
2.3.5	Image analysis	59

2.3.6 Statistics	62
2.4 Results.....	62
2.4.1 Electrode modification and characterization	62
2.4.2 Meso-scale imaging of GCaMP response to electrical stimulation.....	67
2.4.3 Effect of the number of electrode shanks on GCaMP intensity and radius .	72
2.4.4 Material differences in constant voltage versus constant current stimulation	74
2.4.5 Pulse width modulation for microstimulation selectivity	76
2.4.6 Explanted arrays	79
2.5 Discussion	80
2.5.1 Electrochemical features of PC and IrOx	81
2.5.2 Effect of electrode material on the intensity and the spread of the GCAMP response.....	82
2.5.3 Effect of electrode shank number on GCAMP response.....	83
2.5.4 Higher stimulation efficiency from PC than IrOx in both voltage and current controlled stimulation modalities	84
2.5.5 Pulse width modulation on stimulation selectivity in the cortex	85
2.6 Limitations	87
2.7 Conclusion.....	88
3.0 Finite Element Analysis of Electric Fields of PEDOT/CNT and Iridium Oxide	
Electrodes.....	90
3.1 Chapter Overview	90
3.2 Introduction	91

3.2.1 Materials and Methods	92
3.2.1.1 Finite Element Model in COMSOL	92
3.2.1.2 Electrode Preparation	93
3.2.1.3 Scanning Electron Microscopy	93
3.2.1.4 Quantification of Voltage Field Decay	94
3.3 Results.....	94
3.3.1 Electrode Surface Topography	94
3.3.2 2D Finite Element Analysis Using Surface Features Derived from SEM.....	98
3.3.3 Geometric Considerations for Microelectrode Design	102
3.4 Discussion and Conclusion.....	104
4.0 Imaging the Stability of Chronic Electrical Microstimulation Using Electrodes	
Coated with PEDOT/CNT and Iridium Oxide	106
4.1 Chapter Overview	106
4.2 Introduction	107
4.3 Materials and Methods	110
4.3.1 Animal Surgery	110
4.3.2 <i>In vivo</i> Imaging and Electrical Stimulation	110
4.3.3 Image Analysis.....	111
4.3.4 Electrophysiology	112
4.3.5 Electrochemistry and Equivalent Circuit Modeling.....	112
4.3.6 Explant Analysis.....	113
4.3.7 Statistics	113
4.4 Results.....	114

4.4.1 Longitudinal <i>In Vivo</i> Imaging of GCAMP Response to Electrical Stimulation	114
4.4.1.1 Stability of Stimulation Efficiency and GCaMP Response	114
4.4.1.2 Decrease in Neuronal Excitability Over Time	121
4.4.2 Longitudinal Electrophysiology and Changes to Electrode Functions	123
4.4.3 Longitudinal Electrochemical Measurements and Equivalent Circuit Modeling	126
4.4.4 Stimulation Induced Changes to Electrophysiology	132
4.4.5 Explant Investigation	134
4.5 Discussion	136
4.5.1 Fluctuations in Stimulation Efficiency Revealed through <i>In Vivo</i> Imaging	137
4.5.2 Longitudinal Changes in Electrophysiological Measurements	140
4.5.3 PC is a more Energy Efficient Material for Chronic Stimulation	141
4.5.4 Abnormal Cortical Events to Electrical Microstimulation	143
4.5.5 Limitations and Future Research	144
4.6 Conclusion	146
5.0 Conclusion	148
5.1 Summary of Research Findings	148
5.2 Future Directions	150
5.2.1 Directions for the Use of Biomimetic Coatings for Improving Stimulation Stability	151
5.2.1.1 Neural Adhesion Molecule L1	152

5.2.1.2 Superoxide Dismutase Mimic	152
5.2.2 Directions for Further Understanding Stimulation Safety	153
Appendix A Other Significant Contributions	155
Bibliography	158

List of Tables

Table 1 Methods to evaluate biological responses to electrical stimulation.	24
Table 2. Summary of metal and metal oxide materials.....	30
Table 3. Summary of selective CP studies.	40
Table 4. Summary of studies using carbon-based materials.....	50
Table 5. material properties used for finite element modeling.....	93
Table 6. Parameters describing the two-phase exponential decay function representing voltage field distribution nearby PC and IrOx electrodes.	99

List of Figures

Figure 1. Mechanism of neural stimulation.....	5
Figure 2. Electrochemical measurements.	13
Figure 3. Equivalent circuit modeling.....	16
Figure 4. Representative metal based electrode materials.....	29
Figure 5. Representative conducting polymer based electrode materials.	39
Figure 6. Representative CNT and graphene based electrode materials.	42
Figure 7. Representative GC based electrode arrays.....	49
Figure 8. Electrode modification.	65
Figure 9 Electrochemical characterization.....	66
Figure 10. <i>In vivo</i> experimental setup.	68
Figure 11. Mesoscale imaging of GCaMP response to electrical stimulation..	69
Figure 12. Quantification of GCaMP response to electrical stimulation.....	71
Figure 13. Effect of electrode shank number on GCaMP intensity and radius.....	73
Figure 14. Two-photon microscopy investigation of voltage and current controlled electrical stimulation.	75
Figure 15. Effect of pulse width modulation on neural activation.	77
Figure 16. Effect of pulse width modulation on neuronal selectivity.	78
Figure 17. Explant examination.	79
Figure 18. Scanning electron microscopy of acutely explanted Michigan arrays with PEDOT/CNT and IrOx sites.....	95
Figure 19. Estimation of fractal features of the PEDOT/CNT surface.	97

Figure 20. COMSOL simulation environment and electrode geometry.	98
Figure 21. Finite element analysis of PC and IrOx electrode surfaces.	100
Figure 22. Activating function of the 1D extracellular voltage.	101
Figure 23. Geometric factors affecting electrical field distribution of microelectrodes. ...	103
Figure 24. Quantification of geometric factors affecting electrical field distribution.	104
Figure 25. Experimental set up.....	115
Figure 26. GCaMP responses over time.....	116
Figure 27. Example of integrated GCaMP response and binning method.....	117
Figure 28. Quantification of GCaMP response over time.	118
Figure 29. Quantification of stimulation stability.....	120
Figure 30. Two photon microscopy of neuronal excitability over time.	122
Figure 31. Electrophysiology over time.	124
Figure 32. Functions of electrode sites over time.	125
Figure 33. Electrochemistry measurements over time.	127
Figure 34. Equivalent circuit modeling.....	131
Figure 35. Observation of abnormal cortical events during microstimulation.....	133
Figure 36. Explant analysis.	135

Preface

Throughout the preparation of this dissertation, I have received tremendous support and assistance. I would like to thank my advisor, Professor Tracy Cui, whose expertise and experience in neural tissue interface and material design was invaluable in helping me formulate the research questions and methodology. The interdisciplinary nature of our laboratory and our research projects allowed me to acquire skills spanning many disciplines. From electrode surface modification, material surface characterization to electrophysiology, microstimulation, *in vivo* imaging, and data science.

I would like to thank former and current NTE lab members for their generous support with lab tasks. Dr. James Eles was a great mentor as I began at the NTE lab and showing me the ropes in immunohistochemistry and *in vivo* imaging, and most importantly, always exhibiting a positive attitude. Thanks to Kevin Woepfel, who is always there to be a sounding board for data interpretation and answers questions about all things chemistry. Dr. Elisa Castagnola who has a rich background microfabrication and well versed in conducting polymers and carbon-based materials. I have learned so much from her, and she continues to challenge and motivate me to be a better researcher. I would like to thank Emma Yang for her assistance with surgeries. I am incredibly grateful for our new lab members Delin Shi, Vaishnavi Dhawan, Drs Neetu Kushwa, Chao Tan, and Elaine Robbins from whom I have learned so much. Also, I am thankful for the undergraduate students I have mentored, especially Ms Azante Griffith, who was very quick to learn and helped complete tasks that accelerated my progress. Furthermore, my PhD would not have been possible without the help of Dr. Xia Li, our laboratory manager, who is always ahead

with ensuring the availability of lab supplies, who performs impeccable cryosection and immunohistochemistry, who keeps perfect records of everything.

I would like to thank my committee members for sharing their expertise in the completion of this dissertation. I am grateful for Dr. Alberto Vazquez, from whom I have learned so much, from navigating the “Physiology” room at the McGowan Institute, to trouble-shooting instrumentation and developing algorithms for data analysis. Most importantly, along with Mr. Riaz Islam and Dr. James Eles, helped train for (my first) the 2018 Pittsburgh Marathon. I will never forget those 15-mile- Sunday runs around the city, in the coldest of winter. I thank Dr. Takashi Kozai for all the invaluable resources he has compiled during his time at the NTE lab. I am grateful for the insights he has shared with me regarding surviving graduate school. I am particularly grateful and nostalgic about the numerous journal clubs he held, often at the Hofbräuhaus. These critical thinking sessions have helped me improve in formulating research questions and the delivery research results. I thank Dr. Lee Fisher for being a fantastic collaborator and mentor. He has shared with me so much knowledge in peripheral nerve interfaces and played a key role my first two manuscripts on flexible intraneural and intramuscular electrodes. Dr. Rob Turner, who taught a wonderful class in Systems Neuroscience and has given me incredible feedback regarding my dissertation. Furthermore, I thank Dr. Shiguru Amemiya from the Department of Chemistry for generously allowing me to use his COMSOL Multiphysics software for the completion of Chapter 3.

I am incredibly grateful for my peers whom I am privileged to call my best friends. Steven Wellman, Nathan Enick, Michelle Heusser, Nicole McClain, and Erinn Grigsby, all of whom are smart, hard-working scientists who constantly provide moral support and motivate me to do better. Furthermore, this dissertation could not be possible without the support of my parents, Weifa

Zheng and Aiwu Zhang, who have been my role model since day one, and have been providing me with unconditional love. Lastly, I am incredibly grateful for my spouse and one-day Dr. Evan Adcock, for being there for me over the last 10 years, through thick and thin.

1.0 Introduction

1.1 Microelectrode Materials for Chronic Electrical Microstimulation

Electrical microstimulation is a technique in which current is passed through a microelectrode for the excitation of neural tissue. It is an invaluable tool in neuroscience research to dissect neural circuits, relate brain areas, and identify relationships between brain structure and behavior.[1-3] Therapeutically, electrical microstimulation has enabled partial restoration of vision,[4] hearing,[5] movement,[6] somatosensation,[7] and autonomic functions,[8] and has improved organ functions by electrically modulating neural activities.[9] The growing field of neuromodulation is valued approximately at \$8.1 billion in 2019 and is expected to grow more than 13.1% by 2027.[10] Of these, cochlear implants are the most successful and widely deployed, which restore hearing to profoundly deaf patients. As of December 2012, there are 324200 registered devices implanted worldwide.[11]

Microelectrodes are electrodes with geometric surface areas on the order of 2000-10000 μm^2 ,^[12] which are dramatically smaller than macroelectrodes used for traditional deep brain stimulation.[13] The smaller electrode size offers increased spatial selectivity but poses unique challenges in terms of electrode material requirements. The reduction in the electrode area reduces the surface area for electrochemical reactions, which increases impedance and decreases charge injection. To achieve effective activation of neural tissue safely, sufficient charge is required without exceeding potentials for irreversible electrochemical reactions.[12] Platinum (Pt) is widely used for current auditory and visual prosthesis.[14] While smooth Pt has charge injection limit (CIL) below the threshold for activation for these applications, there is a need for increased CIL

for higher resolution next generation devices. Recently, novel materials have been introduced to reduce impedance and improve CIL and new fabrication techniques of traditional metals have emerged. Examples of such materials are iridium oxide (IrOx),[15, 16] titanium nitride (TiN),[17] glassy carbon (GC),[18] nanostructured Pt,[19] and conducting polymer poly (3, 4-ethylenedioxythiophene) (PEDOT) doped with different counter ions.[20-22] These materials have shown dramatic improvement in CIL, on the order of mC/cm^2 , higher than smooth Pt ($35\text{-}100 \mu\text{C cm}^{-2}$) *in vitro*, thanks to the high effective surface area and/or inherently reversible faradaic reactions. However, the CIL of porous Pt and IrOx substantially decreases *in vivo*, and PEDOT, the most stable of the conductive polymers, has shown degradation in chronic practical application.[12, 23] While much progress has been made in understanding and improving the chronic stability of PEDOT based materials [23, 24] other high CIL and stable electrode materials have emerged, including various high surface area carbons and electrodeposited Pt/Ir alloys.[25-29]

Additionally, the implantation of an electrode array into the neural tissue triggers foreign body responses such as inflammation and neuronal loss (reported in detail in [30-32]). Numerous investigations have shed light on the vascular and cellular pathways and time-course of the foreign body response to neural recording devices. [32-34] However, the electrode tissue interface becomes more complex for implants that also deliver electrical stimulation. Not only does the implant itself initiate foreign body response, but the electrical stimulation also has the potential to cause additional damage to both the electrodes and the tissue, which ultimately will lead to decreased stimulation efficacy.[12, 35]

Thus, to achieve stable chronic stimulation, an ideal microelectrode must present (1) low impedance to be able to efficiently deliver charge without exceeding safety limits for both tissue

and electrodes, i.e., high charge injection limit (CIL), (2) small size, to gain high spatial selectivity, (3) biocompatibility, and (4) stable in vivo electrochemical properties for safe and efficacious electrical stimulation.

To meet these requirements, we need to dissect the electrode tissue interface during repetitive electrical stimulation. From a material perspective, we need to understand the mechanism of material failure, and from a biological perspective, the cellular and molecular mechanisms in implantation and stimulation induced tissue responses. This chapter provides details about the challenges in chronic microstimulation. To aid material scientists interested in neural stimulation research, we introduce the in vitro and in vivo testing methods for assessing stimulation performance and provide a detailed overview of the recent research and development in electrode materials for improving performance in electrical stimulation including new fabrication methods.

1.1.1 Mechanism of Electrical Stimulation

1.1.1.1 Activation of Neural Tissue

The neuronal membrane at its resting level is more permeable to potassium ions (K^+) than sodium ions (Na^+). Na^+ - K^+ pumps on the membrane actively pump 2 K^+ in and 3 Na^+ out of the cell for every adenosine triphosphate (ATP) consumed to maintaining a steady K^+ and Na^+ gradient across the neuronal membrane, resulting in a negative resting membrane potential of ~ -70 mV (**Figure 1a**).^[36] When an external anodic electrical stimulation is applied via an extracellular electrode, the membrane voltage becomes less negative, and when this voltage exceeds the threshold (~ 55 mV), voltage-gated Na^+ channels opens and the rapid influx of Na^+ ions initiates an action potential, also called a neuronal spike or firing.^[37] Modulating the neuronal spiking or

action potentials of neuronal populations for a specific brain region can help augment or restore neurological functions. The extracellular voltage (V_e) is directly related to the amplitude of the injected current I_{in} (A), the distance between the cell and the source of the current r (m), and the conductivity of stimulated environment, σ (S m⁻¹) (1-1).[38, 39]

$$V_e = \frac{I_{in}}{4\pi\sigma r} \quad (1-1)$$

1.1.1.2 Faradaic versus Non-Faradaic Charge Transfer

During electrical stimulation, electronic currents that are passed from instrumentation to the electrodes are converted to ionic currents at the electrode/tissue interface. The charge transfer mechanisms at the interface can be either faradaic or capacitive. The faradaic process is a reaction in which surface confined species are oxidized or reduced. These reactions may be irreversible or reversible when an opposite stimulation pulse is quickly applied. For example, the oxidation of the electrode metal into metal ions may be irreversible if the metal ion diffuses away before the reversing pulse is applied (Figure 1b, top panel). On the other hand, IrOx may undergo oxidation and reduction between the different iridium states (Ir²⁺, Ir³⁺, Ir⁴⁺, Ir⁵⁺), and these reactions are reversible (Figure 1b, lower panel).[16] Depending on the materials and stimulation parameter design, reversible faradaic processes can provide high charge injection capability, while irreversible processes can lead to electrode corrosion and release of toxic products and must be avoided.

On the other hand, capacitive charge transfers involve the charging and discharging of an electric double layer, or charge stored across a thin, high-dielectric-constant oxide at the electrode-

electrolyte interface, Figure 1c.^[38] Usually, a capacitive process is a safer charge injection mechanism due to the absence of addition or removal of a chemical species or a morphological change during a stimulation pulse, reducing the likelihood of damage to the electrode or the surrounding tissue.

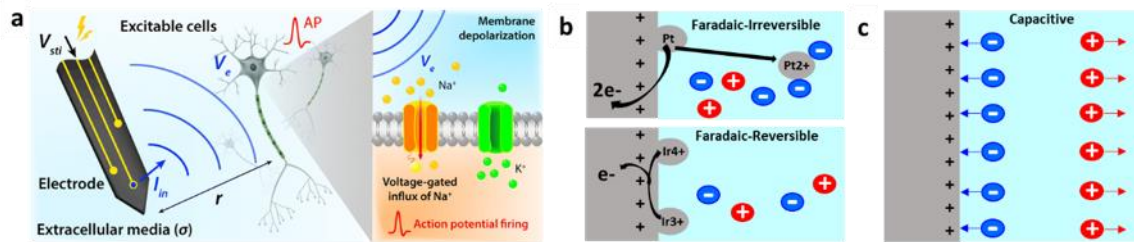


Figure 1. Mechanism of neural stimulation. (a) Schematic showing electrodes stimulate excitable tissues via applying a voltage, the cellular membrane of the targeted neurons was depolarized, which results in firing of action potentials. Adapted from [38] under the creative commons license. (b) Faradaic charge transfer occurs via irreversible and reversible faradaic reactions. (c) Capacitive transfer is achieved via charging and discharging of the electric double layer (EDL) formed by accumulation of ions on the oppositely charged electrode surface.

1.2 Challenges in Chronic Microstimulation

Numerous challenges in chronic electrical stimulation have been reviewed extensively by Merrill et al [35] and Cogan et al [12, 40]. These challenges can be categorized into (1) charge injection limit, (2) tissue health and function, and (3) material stability.

1.2.1 Charge Injection Limit

One of the defining metrics for safe electrical stimulation is the charge injection limit, which characterizes the performance of the electrode in relation to the electrochemical redox window of water. As a conservative estimate for metals like platinum, charge injection limit is the charge density at which -0.6V or $+0.8\text{V}$ are reached at the electrode.[41] To effectively stimulate a functional output, the delivered charge needs to be above the threshold charge density. In human neural prostheses applications, the threshold charge density ranges between $5\text{--}306\ \mu\text{C cm}^{-2}$ ($1000\text{--}2000\ \mu\text{s}$ pulse width) for epi-retinal stimulation.[42, 43] and $190\text{--}2300\ \mu\text{C cm}^{-2}$ ($200\ \mu\text{s}$ pulse width) for intracortical visual stimulation.[44] Traditional stimulating electrode materials like platinum with a CIL of $50\text{--}150\ \mu\text{C/cm}^{-2}$ [41] cannot meet the full range of charge injection requirements for these applications, which drives the need for the development of high charge injection electrode materials.

1.2.2 Stimulation Induced Adverse Biological Responses

Efficacy and safety are important factors for chronic electrical stimulation. The existing inflammation due to electrode insertion can often be exacerbated by electrical stimulations. There have been reports of electrical stimulation induced vasoconstriction, thrombosis in venules and arterioles and blood brain barrier breakdown within $30\ \text{s}$ of stimulation at a charge density threshold necessary for a sensorimotor response or for monophasic pulses at power densities greater than $0.5\ \text{mW cm}^{-2}$. [45-47] Moreover, electrochemical products as a result of faradaic charge injection have been reported to increase the presence of reactive oxygen species which severely damages myelin.[48-53] Furthermore, depending on the stimulation frequency, there may

be persistent depression of neuronal excitability following stimulation of the cortex that last for several days following the cessation of the stimulation.[54] Depending on the desired functional outcome, different metrics are used to evaluate the functional efficacy.[2, 7, 55-57] For the detection of a sensory stimulus in animals, lever press is used to translate an animal's detected electrically evoked sensation.[58] In humans, the detection threshold may be a vocalization of detected sensation to a given stimulus. Depending on the stimulation pulse design, frequency, duty cycle, and duration, varying stability in detection thresholds have been documented. Bartlett et al. reported that with electrodes implanted in the striate cortex in the macaques, when stimulation was applied continuously for 1-8 hours, a temporary or permanent elevation in detection threshold was observed. The main contributor to this phenomenon was hypothesized to be hydrolysis, the evolution of gas from the electrode surface that creates an additional resistive pathway, requiring an increase in currents. However, even by limiting the voltage level of stimulation to be within the range of hydrolysis while also using tantalum pentoxide electrodes which inject charge via predominantly capacitive stimulation, there was still a rise of detection threshold.[59] On the contrary, there have been reports of improved threshold detection over thousands of stimulated trials.[56] In this experiment, electrodes were acutely inserted into the brain and advanced regularly between threshold measurements. This method ensured that each brain region was not subjected to prolonged electrical stimulation. The cause of improved detection threshold over thousands of trials was posited to be due to changes in functional connectivity within the stimulated cortex.[60, 61] Regarding elevated detection threshold, it was hypothesized that the stimulating charge density contributed to potential damage to neuronal tissue. McCreery et al stimulated with iridium microwires with activated IrOx contacts at 4 nC ph^{-1} pulsed continuously for 8 h per day for 30 days and observed neuronal cell loss within $\sim 60 \mu\text{m} - 150 \mu\text{m}$ of a microelectrode. When

stimulating at 2 nC ph^{-1} , no apparent loss in neuronal cells were observed (50 Hz, 50% duty cycle).[62] Conversely, others have reported no significant additional damage to the brain region stimulated via sputtered IrOx on silicon arrays compared to unstimulated arrays, even with up to 20 nC ph^{-1} stimulation for 4 hours per day for 6 months (25-50% duty cycle, train durations of 1 s or 5 s, 300 Hz). While the authors concluded that the ability to stimulate the cortex was maintained over long periods, a small fraction of the stimulated region showed decreased sensitivity to electrical stimulation, likely due to the chronic tissue damage induced by the presence of the implant.[63] The loss of behavioral sensitivity to applied stimulation may be due to potentially harmful by-products of irreversible redox reactions at the electrode surface which may increase oxidative stress, induce pH change, or be toxic. For example, the aforementioned McCreery study reported corrosion of the iridium electrode tip and deposition of elemental iridium in the nearby tissue. While these metal deposit can be speculated to play a negative effect on neuronal health, the corrosion of the electrode is bound to affect stimulation efficiency.

1.2.3 Material Stability

The integrity of the implanted electrode face unique challenges in vivo that often lead to material degradation. Comprehensive analysis of failure modes for various styles of electrode arrays have been extensively studied and reviewed.[30, 64-66] Aside from the most frequently occurring mechanical failure of the I/O connector, other failure mechanisms include mechanical defects from fabrication, chemical, physicochemical and electrochemical reactions, and the interaction of mechanical and chemical stresses.[67] All of these failures can be characterized by varying amounts of fracture, dissolution and delamination of the electrode sites and/or insulation over the implantation duration. For multi-electrode arrays, insulation corrosion and delamination

cause additional interstitial fluid to intrude under existing insulations, resulting in shortages between channels and drastically decreasing electrical impedance.[68-70] For stimulation applications, the excessive fluid under insulation can shunt the stimulating current, requiring an increase in stimulation amplitude to activate the tissue, resulting in poor stimulation efficacy. Additionally, electrical stimulation can also accelerate the rate of corrosion for traditionally used stimulating materials such as tungsten and stainless steel.[71] Even though inert metal such as platinum is considered resistant to corrosion, and IrOx has demonstrated much higher charge injection limit,[72, 73] they can degrade or detach from the substrate upon high charge injection or prolonged stimulation load.[22, 66]

1.3 Testing Methods of Stimulating Electrodes

1.3.1 Electrochemical Methods

Electrochemical measurements such as cyclic voltammetry (CV), electrochemical impedance spectroscopy (EIS) and voltage transient are essential methods for the characterization of an electrically conductive material.

1.3.1.1 Cyclic Voltammetry

Cyclic voltammetry is a powerful tool with which we can investigate the reduction and oxidation processes of molecular species and understand the charge storage capacity of an electrode surface. It is performed by sweeping the voltage between preset range and measuring the resulting current. CV is usually performed with a three-electrode system consisting of a working

electrode (WE, the electrode to be studied), a reference electrode (RE, an electrode with a stable standard potential) and a counter electrode (CE). A potential sweep with respect to a RE is applied to the WE, and the resulting current is then measured between the WE and CE. Figure 2a shows an example of a CV from a Pt surface with and without PEDOT/CNT coating. The PEDOT/CNT coated electrode has a drastically larger cyclic voltammogram. As mentioned above, the current consists of a capacitive and a faradaic portion. The charging current comes from the electrode/solution interface that behaves like a capacitor while the faradaic current is generated by either reduction or oxidation of electro-active compounds on the WE's surface. The anodic and cathodic peaks on a CV reveal the faradic reactions occurring during the potential sweep. In the case of PEDOT/CNT, the anodic peak at -0.15 V and cathodic peak at -0.25 V correspond to the oxidation and reduction of the polymer composite respectively. Using CV, one can define the potential window within which no irreversible reaction occurs (may be called the “water window”), which is useful information for determining the CIL introduced earlier (described in detail later). CV can also be used to characterize charge storage capacity (CSC), which indicates the capacity of the electrode to transfer charge using a combination of capacitive and faradaic mechanisms within a given potential cycle. CSC is typically defined as the charge density transported across the electrode during a CV scan (-0.6 V to +0.8 V vs Ag/AgCl). CSC can be calculated from the integral of a voltammogram (I-V curve) with x-axis being time (s) as x-axis and the y-axis being current (A), Figure 2a (1-2).

$$\text{CSC} = \frac{\int |I| dt}{A} \text{ (C cm}^{-2}\text{)} \quad (1-2)$$

Where I is the measured current (A) and A is the geometric surface area (cm²). CSC may be reported as cathodic or anodic charge storage capacity (CSC_c, CSC_a), when integration is performed for the cathodic or anodic half of the cycle respectively. It is worth pointing out that the speed at which CV is scanned may not be on the same order as the neural stimulation pulse, and the waveforms are also very different (triangular for CV and typically square wave for stimulation). Therefore, the charge transfer mechanism utilized may be very different across the two methods. For example, some of the redox reactions that can occur during a slow CV sweep may not be fast enough to complete in a microsecond long electrical pulse. One should be cautious relating CSC to the charge injection capacity of a stimulation electrode.

1.3.1.2 Electrochemical Impedance Spectroscopy

Electrical impedance is the ratio between an alternating voltage input and the alternating current output. Electrochemical impedance spectroscopy (EIS) is usually performed by applying a small sinusoidal AC potential with varying frequency (10-50 mV, 0.1-10⁵ Hz) to a two or three-electrode system and measuring the resulting phase-shifted current, Figure 2a (1-3).

$$Z(\omega) = \frac{E(\omega)}{i(\omega)} = \frac{E_0 \sin(\omega t)}{I_0 \sin(\omega t + \phi)} = Z_0 \frac{\sin(\omega t)}{\sin(\omega t + \phi)} = Z'(\omega) - jZ''(\omega) \quad (1-3)$$

Where E_0 and I_0 represent the amplitude of the voltage and current signals, respectively, ω is the radial frequency and ϕ the phase shift. $Z'(\omega)$ and $Z''(\omega)$, are the real and imaginary parts of the impedance. The impedance information can be represented using a bode plot, which consists of the impedance magnitude and phase angle as a function of frequency. EIS can be used to

investigate the electrode or tissue properties in vitro or in vivo. Novel material surfaces exhibiting lower interfacial impedance result in a higher S/N ratio in electrophysiology and a more energy efficient electrical stimulation. Figure 2b illustrates a bode plot from a bare Au and Au/CNT surface before and after repeated stimulations. Au/CNT electrodes showed a much lower impedance and were stable after one million stimulations.

1.3.1.3 Voltage Transient

Voltage transient is the change in voltage in response to a current pulse (Figure 2c) CIL is defined as the maximum charge that can be safely injected to electrodes without reaching the water window.

An expression to calculate the CIL of the electrode is:

$$\text{CIL} = \left| \frac{I \times t}{A} \right| \text{ (C cm}^{-2}\text{)} \quad (1-4)$$

Where I is the maximum current (A), t is the pulse width (s), and A is the geometric surface area (cm²). To help better determine the maximum injectable current, the most negative (E_{mc}) and most positive voltage (E_{ma}) in voltage transient curves is usually used in comparison with the water window, which is determined to be the water reduction (-0.6 V) and oxidation potentials (+0.8 V) for conventional metals.[12, 74] E_{mc} and E_{ma} are calculated by subtracting access voltage (V_a) from the maximum cathodic and anodic voltage in the transient curve, as illustrated in Figure 2d. It is worth noting that CIL is dependent on the measurement conditions such as electrode size and stimulation parameters. For example, it was suggested that under shorter pulses, the central part of a circular electrode is underutilized, and therefore the resulting CIL is smaller. The electrode area also plays a role in determining CIL, where the CIL in smaller electrodes is significantly larger

because their diffusion layer is sufficient large to facilitate the counterions and reaction rate is less transport limited.[12] Therefore, a comparison of electrode materials would be unbiased when CILs are measured under the same conditions.

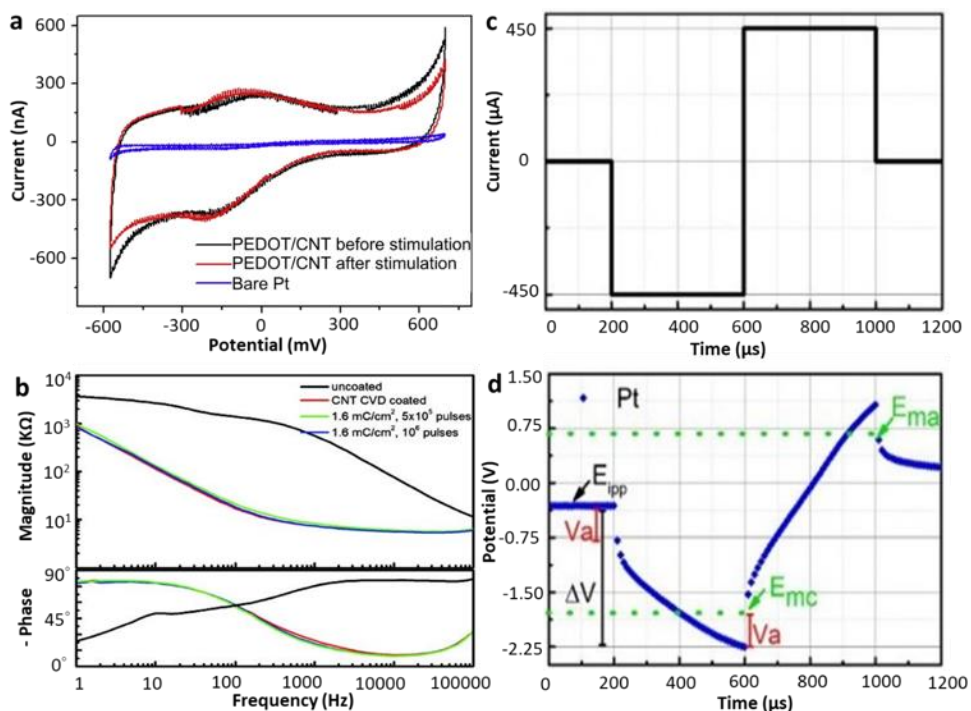


Figure 2. Electrochemical measurements. (a) Cyclic voltammograms of a bare Pt electrode and a PEDOT/CNT coated Pt electrode before and after two weeks of stimulation. Adapted from [23] with permission. (b) Impedance spectra of bare gold, and gold/CNT electrode before and after stimulation experiments. Adapted from [27] with permission. (c) & (d) A biphasic, symmetric 450 μA current pulse and corresponding voltage transient response of Pt microelectrode. Adapted from [18] with permission.

1.3.1.4 Equivalent Circuit Modeling

Equivalent circuit modeling (ECM) is a technique to further quantify the electrode-electrolyte interface. In the model fitting, electrode/tissue interfaces are described in terms of circuit elements such as resistors or capacitors et al. Equivalent circuit models interpret complex

elements at the electrode/tissue interface, charge transfer processes, and surface properties. Below are formulas of some commonly used elements in equivalent circuit models.

The ionic solution R_s is given by:

$$R_s = \rho \frac{l}{A} \quad (1-5)$$

Where ρ is resistivity ($\Omega \text{ m}$), l is distance between the working and counter electrodes (m), and A is the electrode geometric area (m^2). R_s is affected by many factors including ion concentrations, and electrode size. An electrode with larger size or used in high conductivity solution has lower solution resistance.[75, 76]

The theoretical impedance given by a capacitor is described as:

$$Z_c = \frac{1}{j\omega C} \quad (1-6)$$

Where ω is the radial frequency (rad s^{-1}) and C is the capacitance (F). A capacitor's impedance decreases as frequency increases. The current going through ideal capacitor is in -90° phase-shift with voltage. Constant phase element (CPE) represents the electrical component of a non-ideal capacitor that originates from surface inhomogeneity. The impedance of a CPE is given by:

$$Z_{\text{CPE}} = \frac{1}{(j\omega)^{\alpha} Y_0} \quad (1-7)$$

Where ω is the radial frequency (rad/s), Y_0 is the pre-factor of CPE ($F s^{\alpha-1}$) and exponent $0 < \alpha < 1$. When this equation describes a pure capacitor, $\alpha=1$. When this equation describes a pure resistor, $\alpha=0$. For tissue/electrode interface, CPE is often incorporated as the impedance of a non-ideal capacitor response.

Figure 3 gives two examples of equivalent circuit models from literature. Figure 3a,b describes a modified Randle circuit to fit the EIS data from an Ir and activated IrOx (AIROF) microelectrodes. The elements were solution resistance (R_1), charge transfer resistance (R_2) and constant phase element (CPE) representing a dispersive double layer capacitance. The slope in Figure 3a suggest the interface characteristic of a non-ideal capacitor (Figure 3a). The impedance of AIROF at 1 kHz is much lower than un-activated Ir, which is beneficial for electrical stimulation and recording, Figure 3b. They reported a much higher CPE value of AIROF ($1.58 \mu F s^{\alpha-1}$, $0.025 \mu F s^{\alpha-1}$ for Ir), suggesting an increase in pseudo-capacitance. The α value increased from 0.77 to 0.92, indicating that AIROF was closer to an ideal capacitance.[77] Similarly, Figure 3c,d represent the equivalent circuit and impedance spectra obtained from conducting polymer coated electrodes. The circuit elements were solution resistance (R_s), charge transfer impedance (R_{ct}), interface impedance of CPE (Z_{CPE}) and diffusion impedance across the highly porous conducting polymer films (Z_D). In contrast, the model for bare Pt microelectrodes did not contain a Z_D . Here ECM successfully explained the differences of interface impedance between porous PEDOT films and bare Pt.[78]

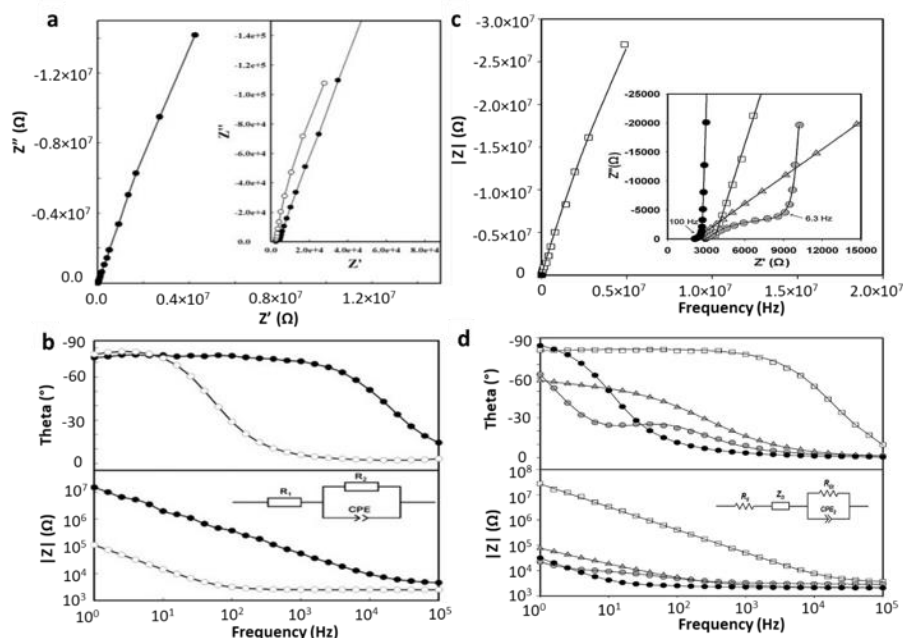


Figure 3. Equivalent circuit modeling. (a) Nyquist plot and (b) Bode plots, impedance, and equivalent circuit model of AIROFs microelectrode (○) and Ir microelectrode (●) in CBS/PBS. Adapted from [77] with permission. (c) Nyquist plot and (d) Bode plot, impedance, and equivalent circuit of Pt (□), PEDOT/PSS (▲), and PEDOT/MWCNT electrode deposited in potentiostatic mode (◻) and galvanostatic mode (◐). Adapted from [78] with permission.

1.3.2 Tests for Evaluating Chemical and Mechanical Integrity

Chemical analyses such as Raman spectroscopy, x-ray photoelectron spectroscopy, SEM-EDAX and inductively coupled plasma mass spectrometry (ICP-MS) are also used to study potential changes to the chemical compositions of material surfaces before and after aging or stimulation, as performed by Negi et al in evaluating the degradation of iridium oxide from continuous electrical stimulation. Using ICP-MS, they quantified the iridium concentration in the solution from stimulating the electrodes at different charge densities and concluded that sputter

coated iridium oxide electrodes have higher damaging threshold (60 —80 nC charge per phase at 1—1.9 mC cm⁻²), compared to activated iridium oxide electrodes (40—50 nC charge per phase at 0.5—0.9 mC cm⁻²).[79-81]

To evaluate the adhesion of a coating to a certain substrate and any possible delamination due to mechanical stress, the Scotch tape test can be performed on coatings deposited on relatively large substrates. As documented in American Society for Testing and Materials (ASTM) standards, cuts are made to the coating before the application of the tape.[82] The tape is then applied and removed, and the integrity of the coating is examined using imaging techniques.[83-85] Furthermore, sonication can be used to test coating integrity. For instance, to evaluate the stability of the PEDOT with NH₂ functional groups in the repeat units, the Martin group ultrasonicated the coating for 1 hour and observed no signs of delamination or cracking whereas typical PEDOT coatings degrade after only seconds of sonication. The stability of PEDOT-NH₂ was attributed to the amine's strong covalent bonding to the metal substrate.[17] Since flexible devices are often subjected to bending forces during handling and *in vivo* use, adhesion needs to be accessed upon bending. Castagnola et al tested flexible ECoG devices coated with PEDOT/CNT. The flexible devices were rolled around a wire with radii of 1.5 and 0.5 mm and electrochemical measurements were used to evaluate the stability of the coating after different degrees of bending.[86]

1.3.3 Thermal Accelerated Aging Test

The vast parameter space in designing an electrode requires rapid understanding of its long-term performance, making it difficult to test each electrode design *in vivo*. To gain understanding of the stability of an electrode material, electrode aging tests have been developed to mimic the *in*

vivo environment. ASTM states that accelerated aging techniques should be based on the assumption that the chemical reactions that occur in the degradation of materials follow the Arrhenius reaction function, which describes that the chemical reaction rate depends on the temperature.

$$k = Ae^{-E_a/RT} \quad (1-8)$$

Where k is the chemical reaction rate, A is a constant, E_a is the activation energy, R is the gas constant, and T is temperature in Kelvin. The aging multiplier, or the accelerating factor, K , at testing temperature T_1 , over body temperature (37 °C), is described as the following:

$$K = 2^{\frac{T_1-37}{10}} \quad (1-9)$$

The equation makes use of the 10-degree (Q10 = 2) rule which states that the rate of chemical reaction doubles for every 10-degrees increased.[87, 88] An upper limit of 60 °C is imposed to exclude possible chemical reactions or physical changes to materials not occurring at body temperature.[89] For mimicking the biological environment in the presence of a foreign body, more aggressive chemical environments may be required. The injury of the neural tissue upon implantation of an electrode triggers a host of immune response, activating microglia and macrophages that secrete pro-inflammatory cytokines and produce various cytotoxic factors such as excitatory amino acids and reactive oxygen species(ROS).[32] Some of these factors such as ROS not only causes tissue damage, they can also be detrimental to the electrode materials.

Takmakov et al designed a rapid accelerated aging (RAA) protocol which includes ROS generated from 10-20 mM hydrogen peroxide with the testing environment maintained at 87 °C.[90] Using this system, they tested commercially available microelectrode arrays with periodic collection of electrochemical impedance spectroscopy data, as well as performing ICP-MS of the soaking solution after RAA to assess elements that may be detached from the electrode surface. Impedances at frequencies 1-10 Hz had the greatest change after the aging process, however there was not a one-to-one correlation with changes in impedances and damages to the electrode surface observed by scanning electron microscopy. These results indicate that impedance may not be the best metric to pinpoint material related damages. A potential explanation is that the impedance frequency spectra are influenced by factors not limited to material related damage. In the frequency range where neural electrodes are typically studied, the lower frequency region (1-10 Hz) is primarily influenced by the electrode double layer capacitance, electrode material surface morphology and topology. The intermediate frequency range (0.1-10 kHz) has a mixed influence from electrode coatings, the implant position and tissue responses. The high frequency range (10 k-10 MHz) reflects electrolyte characteristics and resistance of the conducting materials. The boundaries of these frequency regions are not fixed, and as the electrodes become smaller, the boundary moves towards higher frequencies.[91] Equivalent circuit modeling may be a more comprehensive evaluation of changes to the electrode properties and electrode-tissue interface *in vivo*. [92-94] While the changes in RAA system simulated impedance changes observed after 6 months of *in vivo* implantation, one major limitation lies in the elevated testing temperature (87 °C). While most electrode materials have a high tolerance to heat, other materials such as PEDOT:PSS undergo micro-structural changes as temperatures approach 100 °C and will not

operate in the same condition as it does in the body temperature.[95] Therefore, the RAA system is limited in its use for testing a wide array of electrode materials.

1.3.4 *In vitro* Electrical Stimulation Test

For stimulation applications, electrode materials may be stimulated at physiologically relevant temperature ranges for prolonged periods. For evaluating damaging stimulation thresholds of sputtered IrO_x (SIROF) and AIROF electrodes on Utah arrays, Negi et al subjected these materials to aggressive biphasic stimulations for 7 hours (> 1 million pulses, 50 Hz). In conjunction with electrochemical methods, the authors also performed ICP-MS to examine iridium concentrations in the stimulated solution and concluded that SIROF is better suited for chronic stimulation as it has a higher damage threshold compared to AIROF (damage threshold for SIROF: 60 nC, 1.9 mC cm⁻²; AIROF: 40 nC, 0.5 mC cm⁻², geometric surface area(GSA): 3100 μm²).[80]. Similar methods were employed by Green et al. in investigating the performance of PEDOT/pTs coated electrodes for electrical stimulation. Biphasic pulses with charge densities of 88 μC cm⁻² and with frequencies at 2 kHz were applied to electrodes in 15% serum supplemented cell culture medium for 16 days, totaling 2.8 billion stimulation cycles. Media was refreshed every 48 hours to ensure the presence of active proteins. CSC and SEM evaluations of stimulated PEDOT/p-toluenesulfonate (pTS) showed no significant differences to PEDOT/pTs electrodes without stimulation. Stimulation parameters from other electrical accelerated aging are summarized in Tables 2-4.

1.3.5 Biological Testing

1.3.5.1 *In vitro*

The evaluation of the biological effects of electrical stimulation requires methods that provide read-outs about the health status of the stimulated tissue. From a time and cost-efficient perspective, *in vitro* methods offer tremendous information for the prediction of the cytotoxicity of the stimulating material and the stimulation products *in vivo*. Stimulation material can be immersed in cell culture media to allow leachable toxic compounds to elute out. Stimulation may be applied to collect the stimulation byproduct in the media. The elution can then be added to cultured cells at different doses to assess toxicity using quantitative viability assay such as the MTT assay or live/dead staining.[96, 97] The use of cell cultures also allows for efficient exploration within a large parameter space when microelectrodes are placed in direct contact with the cultured cells.[98, 99]

To be compliant with long term application and clinical use, stimulation devices are required to withstand the sterilization process with the most common being ethylene oxide (ETO) and steam. ETO is often used to sterilize medical devices with components that are sensitive to heat or moisture. When a new electrode material is developed, studies need to be performed to ensure the safety of the material after ETO or steam sterilization. For instance, Green et al sterilized their electrodes using ETO and found that while there were no significant changes to charge storage capacity and electrode potential compared to pre-sterilization condition, the drying conditions in the ETO sterilization process resulted in fine cracks on the PEDOT/pTs coatings.[74] For steam sterilization, Castagnola et al tested stability of PEDOT/CNT coated surfaces at 122 °C and 2 atmospheric pressure for 20 minutes and observed no significant change in the full spectrum electrical impedance.[100] A cell viability assay can be performed using the new material as the

cell culture substrate before and after sterilization to confirm that there is no toxic ETO residue or degradation product.[23] If an electrode material passes the toxicity test, *in vivo* testing will be the next step.

1.3.5.2 Histology

Histological methods such as hematoxylin and eosin as well as immunohistochemistry (IHC) have been used for understanding tissue pathology. Traditional and modern reports of stimulation safety and the *in vivo* biocompatibility of implantable neural devices have utilized various forms of end point histology. Slices of tissue samples containing the electrode location can be stained with desired anti-bodies to observe cellular changes to the electrode tissue interface. IHC has a wide variety of markers that are used to indicate tissue health. NeuN and NF-200 are often used to evaluate quantifiable changes in neuronal cell body and axons near the implant respectively. Meanwhile, IBA-1 and GFAP are used to assess the presence of macrophages and astrocytes near the implant, respectively. The integrity of the blood brain barrier can be interrogated using IgG staining.[24, 101-105] These markers are typically evaluated as either cell count or intensity as a function of distance away from the implant.[33] While histological methods provide pathological information at the sub-cellular level, they do not provide real-time read out of the tissue response to electrical stimulation, potentially missing crucial transient information.

1.3.5.3 Electrophysiology

Electrophysiology can gauge network response to electrical stimulation and may also be used to probe the health of the neurons near the electrodes.[106-108] Unlike *in vitro* and histological methods, electrophysiology does not provide visual observation of the biological tissue near the electrode. Additionally, electrical artifacts evoked by stimulation prevent the

detection of spiking activity adjacent to the electrode, obscuring the interpretation of experimental results. However, artifact removal is a possibility using computational methods.[109] Behavior analysis is a powerful tool for evaluation of functional electrical stimulation as it provides a one-to-one functional response to stimulation.[7, 110] However, it may not directly offer information on inflammatory tissue response or neuronal health.

1.3.5.4 Live Imaging

Imaging has become an increasingly popular method for evaluating electrical stimulation for it allows the direct visualization of events occurring at the electrode-tissue interface in real time. Drawing from an arsenal of voltage- or calcium- sensitive dyes and transgenic tools that label the cells of interest, researchers can gain tremendous information about the transient responses to electrical stimulation. For instance, electrical stimulation induced cell permeability change was studied using brightfield and fluorescence imaging. A change was observed in the porosity of the cellular layer surrounding the electrode which resulted in a change in electrical impedance *in vivo*. [111] The Weiland group assessed stimulation safety pulse paradigm design for safe and selective retinal stimulation using optical coherence tomography and two-photon imaging. [112, 113] Using *in vivo* two-photon calcium imaging in mice, rats, and cat models, Histed et al revealed a sparse, distributed population of cortical neurons by electrical microstimulation via glass pipettes containing tungsten and platinum-iridium microwire electrodes. [114] The Kozai group investigated the calcium responses to prolonged electrical stimulation in Thy1-GCaMP6s mice and reported the effect of stimulation frequency, [115] pulse symmetry, and phase order [116] using Michigan planar arrays. [117] Also using two-photon imaging, the Cui group revealed stimulation induced gas evolution which has led to mechanical deformation and displacement of neurons and altered neural activities. [118] Newly designed behavioral tools for small animals also enabled the

in vivo imaging of brain responses to electrical stimulation in awake mice, closely mimicking scenarios in non-human primates and humans.[119] However, most imaging on stimulation is performed in the acute(weeks 0-2 post implantation) to sub-acute period (weeks 4-5 post implantation) because longer duration studies face the challenges of meningeal regrowth, obscuring the imaging window while reducing the spatial resolution of deep brain regions.[120] To improve imaging depth, multi-photon imaging systems may be used[121]. Pros and cons of methods mentioned above are summarized in Table 1.

Table 1 Methods to evaluate biological responses to electrical stimulation.

Methods	Examples	Advantage	Disadvantage	Solutions
<i>In vitro</i> methods	<ul style="list-style-type: none"> • Cytotoxicity assays • Cell cultures 	Quick turn out, large sample size; allow testing of individual factors ; minimize the use of animals	Cell cultures lack the cellular dynamic <i>in vivo</i> . Substrates can affect cellular morphology	Co- cultures of different cells; varying substrate roughness to mimic <i>in vivo</i> mechanical properties; 3D cell cultures
Histology	<ul style="list-style-type: none"> • Hematoxylin and eosin • Immunohistochemistry 	High resolution evaluation of cellular and molecular changes in tissue	Lack of immediate read out of tissue health; Unable to capture transient changes	Live imaging
Electrophysiology	Simultaneous stimulation and recording	Examine neuronal network responses to electrical stimulation	Issues with stimulation artifact Motion artifact in awake preparations	Improved algorithm for artifact removal; increased recording density
Behavior	<ul style="list-style-type: none"> • Vocalization of sensation (humans) • Lever press (non-human primates) 	Direct read out of functional output in real time	no direct readout on the tissue health near the stimulating electrode; requires extensive training in animals	Automated training protocols paired with <i>in vivo</i> imaging
Imaging	<ul style="list-style-type: none"> • Meso-scale fluorescence imaging • Two-photon microscopy • Optical coherence tomography 	Examine cell responses to stimulation with down to sub-cellular resolution and high temporal resolution in real time	Costly transgenic tools Surgical preparation requires skill Only image down to layers 2-3 of cortex Meningeal regrowth results in poorer image quality over time	Use alternative sealing methods for the cranial window; flexible and transparent arrays for imaging and studying the electrode -tissue interface.

1.4 Material Development for Stable Electrical Stimulation

1.4.1 Metal Materials

Modern microfabrication techniques have expedited the production of multi-electrode arrays (MEA) with high channel counts enabling high spatial resolution stimulation. The penetrating Utah array, the planar Michigan probes and microwire arrays are the most widely used. The Utah array is made by micromachining a monolithic piece of silicon and acid-etching to produce an array of silicon needles that make up the base substrate of the electrode shanks.[122] The Michigan probes are made with traditional photolithography.[123] For microstimulation, noble metal or metal oxide can be sputtered on for both types of arrays, which have been widely used for stimulation application *in vitro* and *in vivo*. [124-127] Microwire arrays are arrays of insulated metal wires with exposed metal tips. Noble metals like Pt, or PtIr wires have been extensively used for stimulating the spinal cord, skeletal muscles, and the cochlea.[128] PtIr wires can be electrolytically etched to a cone shape that terminates in a blunt, hemisphere tip. For some microstimulation studies, the CIL (0.3 mC cm^{-2}) of this conical electrode tip is not sufficient.[129] Boehler et al. deposited a nanostructure Pt from an electrochemical reduction process that used H_2PtCl_6 as the electrolyte and HCOOH as a reducing agent. As the charge density increased, the morphology became fuzzier, more extended, and fractal. Electrochemical characterizations like CV, voltage transient, and impedance were performed on the NanoPt conical electrode. A CIL as high as $3.0 \pm 0.1 \text{ mC cm}^{-2}$ was reported, which was more than 30 times higher than traditional Pt microelectrodes. The high CIL, CSC ($5.3 \text{ mC cm}^{-2} @ 100 \text{ mV s}^{-1}$) and low impedance ($1000 \mu\text{m}^2$, $15 \text{ k}\Omega @ 1 \text{ kHz}$) were attributed to the high electrochemical surface area of the NanoPt. The NanoPt was tested *in vivo* in mice hippocampus. They reported an electrochemically and physically stable

surface even after a 1.5-billion stimulation pulse at a charge density of 1.5 mC cm^{-2} , with only minimal cracking (Figure 4a,b).[19] In another high surface area Pt study by Green et al., a laser-roughened Pt MEAs was continuously measured for 16 days under a $500 \mu\text{A}$, $200 \mu\text{s}$ width stimulation for 2.8-billion cycles. The authors reported some protein debris adsorbed on the Pt surface, with no change in CSC.[130] Soft and flexible polymers have been utilized as electrode substrates to minimize the mechanical mismatch with tissue and reduce inflammation. However, the mechanical mismatch between the metal site and polymer substrate creates a weak link. Arreaga-Salas et al. treated Iridium microelectrodes with electrical aging (2 billion symmetric biphasic pulse, $200 \mu\text{C cm}^{-2}$, $300 \mu\text{m}^2$), which was found to only cause cracking of the neighboring encapsulation layer, with no delamination of the iridium, Figure 4c,d.[131]

IrOx emerged as a more promising material for electrical stimulation in recent decades because of its high charge injection capacity. IrOx electrodes have been tested for in vivo studies in cortex, retinal, basal ganglia nucleus, and others.^[141-143] Various methods can be used to form IrOx. SIROF are deposited through a sputtering system while AIROF are formed by repeated oxidation and reduction of a bare Ir metal through electrical pulsing or potential sweep (referred to as activation).^[12, 144] Novel methods like chemical bath, electrodeposition or thermal treatment have also been reported to fabricate IrOx.[25, 26, 132] Comparing the stability of IrOx in different works is difficult due to the difference in electrode size and pulsing waveform. As suggested by Negi et al, the intrinsic stability of IrOx is likely related to the physical properties of the film, such as density, roughness, and thickness. In their study, SIROF was found to have higher density (7 g cm^{-3}) than AIROF, leading to higher stability in response to strong electrical pulsing.[80] In some other studies, electrodeposited and thermal treated IrOx were also proven to be stable under organic oxidation conditions, ultrasonication, or electrical pulsing.[25, 26] IrOx may inject charge

in the oxide film through a reversible reaction that involves oxidation and reduction between the Ir^{3+} and Ir^{4+} states of the oxide.[16] AIROF and SIROF both permit a more than 30-fold higher level of CIL (3-15 mC cm^{-2}) compared to traditional Pt or PtIr.

The CIL of IrOx can be improved by altering the electrochemical activation waveform. Lu et al. created an AIROF by pulsing an Ir microwire in saline solution. Their SEM images showed that the AIROF activated by symmetric pulses had a smooth surface while asymmetric pulses produced a porous surface. A CIL as high as 4.1 mC cm^{-2} was reported in their study using asymmetric activation pulse and the impedance measured from AIROF ($7850 \mu\text{m}^2$, $2.54 \text{ k}\Omega$, 1 kHz) was 92% lower than bare Ir surfaces ($7850 \mu\text{m}^2$, $32.36 \text{ k}\Omega$, 1 kHz). A significantly lower CIL of 2.3 mC cm^{-2} was found using traditional symmetric method.[77] In addition, pulsing waveforms have been suggested to significantly affect the CIL of iridium oxide. Specifically, reversing pulse polarity, the ratio of relative pulsing time, and changing the potential-bias have been demonstrated as methods to improve the CIL of iridium oxide.[12]

Despite the high charge injection limit, the stability of materials surfaces is also important, and it is related to the parameters of pulsing. An early study by Cogan et al. suggested that high amplitude micro-stimulations and extreme polarization promote delamination. When subjected to a comparatively low current density pulse (2 mC cm^{-2}), the AIROF film remained intact with no Ir deposits to tissues even after a 1.3-million stimulation cycles. However, the electrode subjected to high charge density pulses (3 mC/cm^2) showed poor adhesion of AIROF coating and Ir-containing deposits to adjacent tissues after only 10k pulses, Figure 4e,f.[133]

Capacitive metals like Ta/ Ta_2O_5 and Ti/ TiO_2 were not widely used due to limited charge injection capability.[12, 17, 128] Similarly, TiN also injects charge via the capacitive electrode/electrolyte double layer process. TiN was reported to be a material that was mechanically

and electrochemically stable in the body.[128] Meijs et al. used TiN stimulation electrodes in porcine animal models and reported stable chronic use. No tissue damage was found, and the value of equivalent circuit elements were also stable for up to 50 days.[134] However, smooth TiN had limited charge storage capacity. Weiland et al. created a porous TiN by depositing TiN on a silicon substrate through sputtered titanium in nitrogen/argon atmosphere. The lack of redox peaks in the CV curves indicate the absence of faradaic processes, minimizing the likelihood of ion escaping from the surface. The TiN had a columnar surface morphology that resulted in a high electrochemical surface area. They compared TiN with IrOx surface and reported a similar impedance ($4000 \mu\text{m}^2$, $40 \text{ k}\Omega$, 1 kHz). The highest CIL of TiN was 0.9 mC cm^{-2} , which was lower than a 5.75 mC cm^{-2} CIL obtained from IrOx under the same pulse.[17] Due to the low charge injection limit, TiN has been mostly used as recording electrodes in vivo which takes advantage of its low impedance and high stability.[135, 136] Table 1 summarizes the above-mentioned metal-based work in detail. It can be concluded that IrOx remains an effective material due to its faradaic charge injection nature and high charge density, while TiN has the advantages over traditional metal electrode like Pt, Ir, ITO in terms of higher CIL and comparatively lower impedance. Therefore, TiN can be used in circumstances where a low charge density capability is sufficient.[17] For the purposes of high-demand neural prosthesis, novel material designs utilizing reversible faradaic charge injection and high surface area are encouraged.

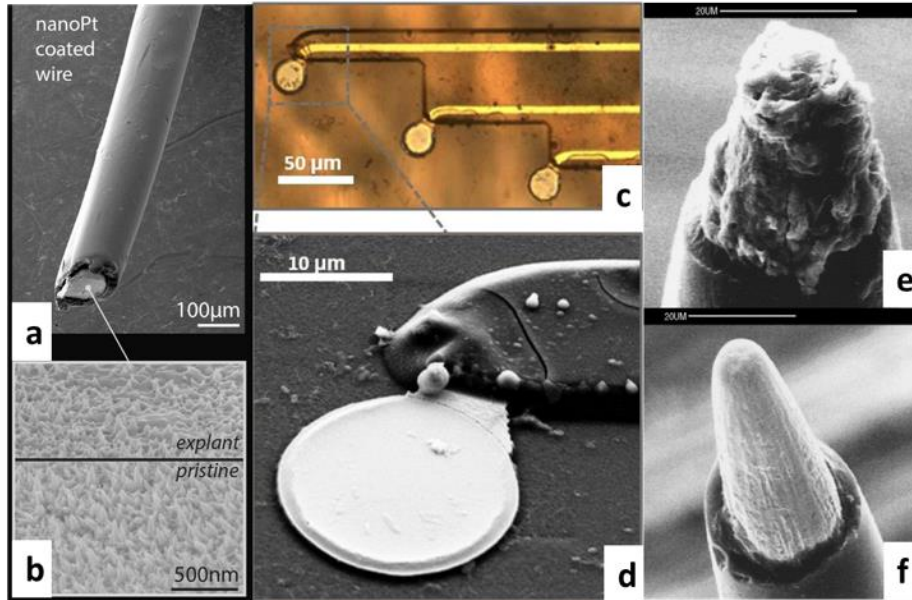


Figure 4. Representative metal based electrode materials. (a) SEM picture of NanoPt coated PtIr wire. Scale bar is 100 μm . (b) SEM of explanted electrode surface in comparison to pristine NanoPt electrode. The surface was not damaged, but some tissue remained on surface. Scale bar is 500 nm. Adapted from [19] with permission. (c) & d) Optical and SEM picture of Iridium microelectrode after 169 hr electrical aging ($6 \mu\text{A}$, $100 \mu\text{s phase}^{-1}$, 2 billion biphasic). Parylene-C layer was delaminated and cracked while Iridium remain intact. Scale bar is 50 μm in panel (c) and 10 μm in panel (d). Adapted from [131] with permission. (e) SEM picture of explanted AIROF conical electrode pulsed for 7 hours at a high current density of 3 mC cm^{-2} ($100 \mu\text{A}$, $600 \mu\text{s phase}^{-1}$, 100 pulse/s, +0.4 V bias), the surface was corroded. Scale bar is 20 μm . (f) SEM picture of explanted AIROF conical electrode after 6 months without pulsing. Adapted from [133] with permission.

Table 2. Summary of metal and metal oxide materials

SIROF	2000 μm^2	EIS 90 days	-	2	34.3 \pm 21.7 @50 mV/s	6.7 \pm 0.2 k Ω	Rs(Rct CPE)	-	124]
SIROF	20 μm^2	-	-	3.33 \pm 0.5	109 \pm 2 @50 mV/s	241 \pm 11 k Ω	-	-	126]
SIROF	1960 μm^2	-	-	1.4 \pm 0.2	49 @50 mV/s	12 \pm 1.4 k Ω	-	-	126]
SIROF	2000 μm^2	9 weeks (1B stim)	Amp:20 A, PW:0.2 ms	3.57	~ 30	~2 k Ω	-	-	137]
SIROF	150 μm^2	-	0.2 ms pulse width, 50 Hz	15.3	35 \pm 2.2	90.2 \pm 26.1 k Ω	-	Rat motor cortex, basal ganglia of Zebra Finch	138]
AIROF	877 μm^2	-	-	3.9	23	-	-	-	129]
AIROF	1130 μm^2	-	-	4.9	12 to 55	-	-	-	16]
AIROF	2024 μm^2	-	-	3.3	29	-	-	-	16]
AIROF	2015 μm^2	-	-	9.6	25.1	-	-	-	16]
AIROF	7850 μm^2	12 hr	V [-0.6, 0.8] 50Hz	4.1	-	2.54 k Ω	Rs(Rct CPE)	-	77]
AIROF	2000 μm^2	7 hrs	2 mC/cm ² 1.3 million or 3 mC/cm ² 100s	-	22	-	-	Cat, sensorimotor cortex	139]
AIROF	78.5 mm ²	3 days (4M stim)	PW:0.2 ms	-	58.57 \pm 0.96	19.43 \pm 0.13 k Ω	-	-	127]
AIROF	4000 μm^2	-	PW:0.2 ms	5.75	100 mV s ⁻¹	~ 38 k Ω	-	-	17]
CIROF (chemical)	1 mm ²	-	-	-	1.26-78.29	-	-	-	132]
TIROF (thermal)	5400 μm^2	-	-	-	-	-	-	-	26]
EIROF/Pt gray(ED)	0.0314 mm ²	4 days (17M stim)	Amp:500 μ A, PW:0.1 ms	0.83	22.29	7802 k Ω	Rs(Rct CPE)	-	25]
RuOx	200 μm^2	21 days	Amp:20 μ A, PW:0.2 ms, IPD:0.1 ms	-	49 \pm 20	73.83 \pm 59.91 k Ω	-	Rat, motor cortex	140]
Pt (nano)	962 μm^2	1.5B stim cycles	PW: 200, 1.5 mC/mm ²	3.0 \pm 0.1	5.333 \pm 0.0208	~ 15 k Ω	-	Mice, medial septum, hippocampus	19]
Pt gray	0.0314 mm ²	-	-	0.13	7.96	20764 k Ω	Rs(Rct CPE)	-	[25]

Table 2. Continued

Pt	0.113 mm ²	16 days (2.8B stim)	Amp:500 μ A, PW:0.2 ms, IPD:0.1 ms	0.05-0.12	~ 8-10	~ 11.3 k Ω	-	Cat visual cortex	[74]
Pt	2000 μ m ²	EIS 90 days	-	0.3	4.4 \pm 3.1	125 \pm 0.25 k Ω	Rs(Rct CPE)	-	124]
Pt	100 μ m ²	-	-	-	10 \pm 1.7	481.3 \pm 67.9 k Ω	-	-	138]
PtIr(20%)	0.014 mm ²	-	Amp:100 μ A, PW:0.1 ms, IPD:0.01 ms	0.018-0.023	-	-	-	Rat motor cortex	125]
PtIr(20%)	1105 μ m ²	-	-	0.3	5.6	-	-	-	129]
Ir	78.5 mm ²	3 days	PW:0.2 ms	-	2.27 \pm 0.24	24.31 \pm 0.62 Ω	-	-	127]
Ir	1250 μ m ²	-	-	-	0.1 \pm 0.5	468.8 \pm 13.3 k Ω	-	-	141]
Ir	300 μ m ²	169 hrs (2.2B stim)	Amp:6 μ A, PW:0.1 ms	-	10	~ 200 k Ω	-	-	131]
Au	100 μ m ²	Acute use	-	-	2 \pm 0.3	2860 \pm 300 k Ω	-	-	138]
Au	800 μ m ²	-	-	-	-	850 k Ω	-	-	142]
Au (nano)	800 μ m ²	-	-	-	-	30 k Ω	-	-	142]
ITO	200 μ m ²	21 days	Amp:20 μ A, PW:0.2 ms, IPD:0.1 ms	-	1 \pm 2	1200 \pm 500 k Ω	-	-	140]
ITO	2500 μ m ²	2 months	-	-	-	270 k Ω	-	-	143]
TiN	150 μ m ²	-	PW:0.2 ms	6.3	12 \pm 2.8	31.1 \pm 7.3 k Ω	-	-	138]
TiN	0.016 mm ²	-	Amp:100 μ A, PW:0.1 ms, IPD:0.01 ms	0.072-0.194	-	-	-	Rat motor cortex	125]
TiN	4000 μ m ²	-	PW:0.5 ms	0.9	2.47	~ 40 k Ω	-	-	17]
Electrode material	GSA	Duration of testing	stimulation paradigm	CIL(mC cm⁻²)	CSC(mC cm⁻²)	Imp @1kHz	ECM	In vivo	Ref
SIROF	200 μ m ²	21 days	Amp:20 μ A, PW:0.2 ms, IPD: 0.1 ms	-	59 \pm 38 @50 mV/s	166.1 \pm 103.1 k Ω	-	-	140]

Rs; solution resistance; R_{ct}: charge transfer resistance; CPE: constant phase element.

1.4.2 Conducting Polymer

Conducting polymers are polymers with a conjugated backbone. Electrical conductivity is achieved by oxidizing the polymer to produce positive charges along the backbone. In this process, negatively charged ions are often referred to as counter ions or dopants, they are incorporated to maintain a charge neutral state. Among many conducting polymers, PEDOT offers superior chemical stability because the dioxyethylene bridging group across the 3- and 4- positions of the heterocycle can prevent α - β coupling, making it chemically and electrochemically stable and suitable for *in vivo* neural electrode applications.[144-146] Owing to its high surface area morphology and high electrical and ionic conductivity, PEDOT drastically reduces electrical impedance and improves signal to noise ratio for neurophysiological recordings.[102] while increasing charge injection limit for stimulation.[22] PEDOT can be electropolymerized or spin coated onto a substrate and is stable under ETO sterilization[130] and steam under pressure.[100]

For *in vivo* applications, Vara et al doped PEDOT with poly(4-styrenesulfonic acid-co-maleic acid) (PSS-co-ma) on carbon microfibers and tested its efficacy for *in vivo* spinal cord stimulation. The polymer coated electrode had an impedance of less than $10 \Omega\text{cm}^2$ (250 μm length and 7 μm diameter carbon fiber substrate), and a low cathodic phase voltage transient of 0.8 V in response to a 100 μA stimulation. Despite its superior electrochemical properties, after being pulsed for 6000 times, the voltage excursion resulted in a charge injection value that surpassed the safety limits.[12] Electrochemical measurements *in vivo* showed an order of magnitude increase in electrical impedance at low frequencies suggesting that the PEDOT coating had delaminated from the underlying substrate.[147]

Table 3 provides a summary of recent developments in using PEDOT and various counterions as stimulating electrodes.

1.4.2.1 Methods to Improve Conducting Polymer (CP) Adhesion

1.4.2.1.1 Substrates

Various methods have been used to modify the substrates for improved adhesion[148] [149] . In 2003, Cui et. al. has shown that roughening the substrate with electrodeposited fuzzy gold improved PEDOT/PSS film adhesion.[150] Similarly, Pranti et al. polymerized PEDOT/PSS on iodine etched gold substrate, the rough and porous morphology of the etched surface increased the PEDOT/PSS film's mechanical stability. The resulting electrode showed stability under an ultrasonic cleaning protocol at 35kHz at 300 W for 11 minutes.[148] Green et al, performed a comprehensive study on doping PEDOT with ClO_4^- , PSS, and pTS on smooth and laser roughened Pt substrates, and concluded that roughening the underlying metal substrate improves post sterilization CSC and post aging CSC for all variants of PEDOT and PEDOT doped, with pTS was found to be the most stable.[151]

Vomero et al demonstrated superior PEDOT/PSS stability on glassy carbon surfaces compared to Pt surfaces on polyimide substrates. Also, the CTC of the PEDOT-PSS-coated GC

electrodes was nearly double the CTC of the PEDOT-PSS-coated Pt ones. This suggests that the nature of the underlayer (i.e., GC or Pt) strongly affects polymer growth and, as a consequence, the properties of the deposited PEDOT-PSS film. For the same geometric surface area (300 μm diameter), GC was intact after 5 million pulses whereas Pt delaminated from the polyimide substrate after 1 million pulses at a charge density of $0.43\text{mC}/\text{cm}^2$. When coated with PEDOT/PSS, the GC based electrodes showed negligible changes in EIS and CV after 5 million pulses. The use of PEDOT/PSS enabled miniaturization of the GC down to $60\mu\text{m}$ diameter while maintaining stable electrochemical properties (impedance at 1kHz $3.6 \pm 0.4 \text{ k}\Omega$, CSC of $893.5 \pm 137.8 \text{ mC cm}^{-2}$) after 1 million aggressive pulses at 10mC cm^{-2} . [152]

1.4.2.1.2 Solvents

Solvent also plays a critical role in PEDOT's stability. Particularly when PEDOT/ BF_4 is polymerized in water and polycarbonate, it showed unfavorable flat morphology and was prone to delamination. On the other hand, PEDOT/ BF_4 polymerized in acetonitrile showed exceptional mechanical and electrochemical stability under the insult of steam sterilization, soaking in PBS for 2 weeks in ambient temperature, and ultrasonication in water for 2-3 minutes. When used in an application for deep brain stimulation, this coating survived up to 15 days stimulating the subthalamic nucleus of rat under daily electrical stimulations consisting 90 minutes of bi-phasic pulses of $20 \mu\text{A}$ at 130 Hz . [153]

1.4.2.1.3 Dopants

For neural stimulation, poly(styrene sulfonate)(PSS), [22, 151] tetrafluoroborate (BF_4), [153] [151] paratoluene sulfonate (pTS), [151] functionalized carbon nanotubes (fCNTs), [23] and ionic liquid 1-ethyl-3-methylimidazolium bis(trifluoromethylsulfonyl)imide have been evaluated by numerous groups for their performances. [154] The material property and stability of PEDOT can be altered by the underlying substrate and the counter ion. [23, 151, 155] PSS is a polymer dopant (~70 kDa) with one sulfonate unit on every monomer unit of styrene. While the sulfonate units make it a suitable dopant for PEDOT, the long polystyrene chains add stiffness making the coating more brittle, and more prone to failure by cracking and delamination, which is less ideal for chronic applications. Alternatively, doping PEDOT with smaller molecules such as ClO_4^- (106 Da), BF_4 (86 Da) and pTS (194 Da) may result in more flexible polymeric films. The flexibility enables PEDOT to effectively anchor into crevices of the substrate, improving adhesion. The disadvantages of having smaller dopants is that there is a high likelihood of them leaching out of the PEDOT coating, either imposing toxicity to the tissue or compromising coating's electrochemical properties. [156] Nevertheless, PEDOT/PSS is still favored by most as an excellent candidate for electrical stimulation. To facilitate water stability of spin coated PEDOT/PSS films, Kim et al. treated PEDOT/PSS films with >95% sulfuric acid to create crystallized PEDOT/PSS films (cPEDOT/PSS). The acid treatment removed excess water soluble PSS chains which would otherwise cause the polymer to swell and degrade in water underwater due to the hygroscopic nature of PSS. The crystallized PEDOT/PSS film showed intact morphology without film delamination or dissolution after 3 weeks of soaking in water, a significant improvement from non-crystallized PEDOT/PSS films. [157]

Nanomaterial based dopants have also been investigated for improving PEDOT properties, including carbon nanotubes, graphene nanosheets and nanoparticles. Carbon nanotubes harness extraordinary strength, electrical conductivity, and chemical stability, and have been shown to promote neuronal differentiation and neurite outgrowth.[158, 159] Luo et al doped PEDOT with multi walled CNTs (MWCNT) on Pt substrates (200 μm diameter), the resulting electrode had a charge injection of 2.5 mC cm^{-2} , charge storage of $61.4 \pm 6.9 \text{ mC cm}^{-2}$, and impedances at 1 kHz ranging from 3 to 7 $\text{k}\Omega$. The electrochemical features and surface morphology of this coating remained stable after 3 months of soaking in PBS and continuous electrical stimulation with biphasic pulses between week 5 to week 7 at 0.35 mC cm^{-2} , 50 Hz. The structural stability of the coating can be explained by the network microstructure formed in the presence of the CNTs, which are evenly distributed across the coating. The CNTs serve as reinforcing elements that prevent cracking of the film when the polymer undergoes expansion and shrinkage.[23] Furthermore, Zhou et al reported that the polymerizing PEDOT/MWCNT galvanostatically results in superior morphology and electrochemical properties compared to PEDOT/PSS and PEDOT/MWCNT coated potentiostatically. For the same Pt substrate, PEDOT/MWCNT films polymerized with a potentiostatic method showed a transverse growth trend, exceeding the diameter of the underlying substrate, increasing the likelihood of crosstalk between electrode sites for high density multielectrode arrays. Whereas galvanostatically polymerized coatings showed a trend of longitudinal growth, and the coating was confined within the $100 \mu\text{m}$ diameter of the substrate and exhibited a 3D cone shape (Figure 5) . Electrochemical testing of the different coating methods showed that the galvanostatic polymerization method is preferred. The CIL reached 6.2 mC cm^{-2} and it is electrochemically stable under 96 hours of stimulation at $3\text{mC}/\text{cm}^2$ biphasic current pulses in bicarbonate and PBS solution (37°C).[78] Another carbon variant, graphene oxide, has been

reported as a dopant for PEDOT for electrical stimulation[160]. While exhibiting high CIL (4.7 mC cm^{-2}), high CSC (86.75 mC cm^{-2}), and low impedance ($2.2 \text{ k}\Omega$ at 1 kHz), the coating showed reduced CSC after 1000 cycles of CV sweeps from -0.6 V to 0.8 V , suggesting that some coating may be lost.[160] Carli et al. investigated the effect of co-doping PEDOT using PSS and oxidized single walled carbon nano horns (ox-SWCNH) and compared with co-doping with PSS and multiwalled carbon nanotubes (ox-MWCNT) polymerized on nanostructured gold substrate for improved adhesion. The small, ox-SWCNH resulted in spherical aggregates with big pores up to 150 nm in diameter, generating a larger electrochemical surface area (CSC $101 \pm 18.6 \text{ mC cm}^{-2}$, CIL: 11.6 mC cm^{-2}) compared to ox-MWCNT which generated a pore size of 30 nm in diameter (CSC: $43 \pm 14.9 \text{ mC cm}^{-2}$, CIL: 7.7 mC cm^{-2}). Despite differences in morphology, both ox-SWCNH and ox-MWCNT had similar impedances across low, medium and high frequency range, and were resilient under 5 million pulses at a charge density of 5 mC cm^{-2} , enough to induce IrOx delamination.[133, 161]

1.4.2.2 Drug Delivery to Improve Stimulation Stability

Unlike traditional metals, the unique properties of CPs enable the incorporation of drugs that may be beneficial for decreasing tissue inflammation while improving the stability at the electrode-tissue interface. Dexamethasone(Dex) is an anti-inflammatory steroid that reduces inflammation.[162] It can be electrochemically released from the bulk of the conducting polymer using CVs.[163, 164] The drug loading capacity of CPs can be further improved by doping the polymer with nano drug carriers, such as CNTs,[165] graphene oxide[166] and nanoparticles for targeted and on-demand drug delivery.[167] Kolarcik et al stimulated the dorsal root ganglion with

electrodes coated with PEDOT co-doped with CNTs and Dex. Electrical stimulation was delivered for 1 hour per day for 10 days using biphasic pulses consisting of 20 μA of 200 μs cathodic phase and 400 μs anodic phase with half the amplitude. PEDOT/CNT/Dex coated electrodes showed significantly less neuronal death compared to non-coated electrodes.[24] Woeppel et al doped PEDOT with sulfonate modified particles (SNP). The selective inclusion of hexadecyltrimethylammonium bromide (CTAB) allows for the creation of porous and non-porous SNPs. Nonporous SNP doped PEDOT films had significantly lower interfacial impedance than PEDOT/PSS of the same dimensions, high CIL (4.8 mC cm^{-2}) and are significantly more stable than PEDOT/PSS under 24 hours of stimulation at 85% CIL at 50 Hz (4.32 million pulses). Porous SNPs enable the loading of various drugs that may be otherwise sensitive to electrochemical reactions or possess positive ions making it unsuitable as the lone dopant for PEDOT. The authors demonstrated successful release of doxorubicin and melatonin and their maintained bioactivity in the released environment. Additionally, successful suppression of neuron activity via the release of DNQX in the cortex of GCAMP6s mice was demonstrated *in vivo*. [167]

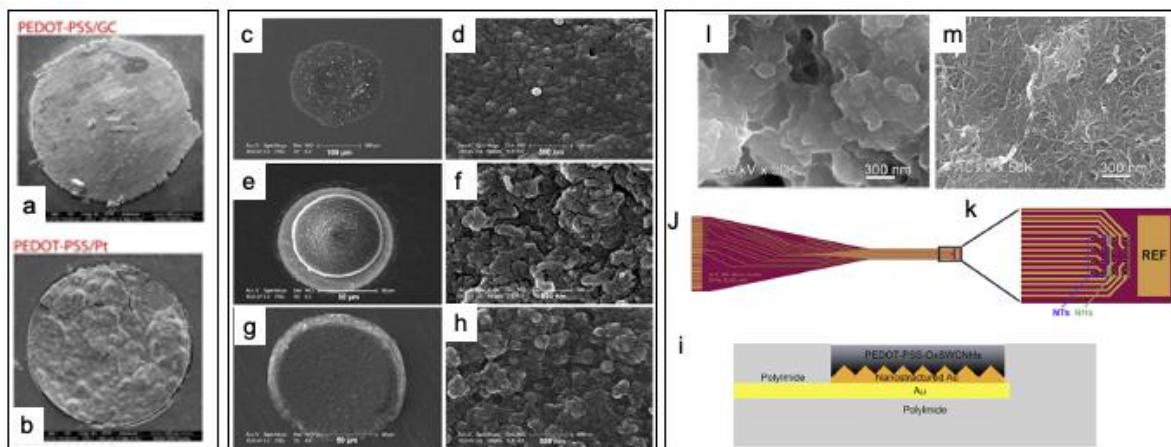


Figure 5. Representative conducting polymer based electrode materials.(a) Scanning electron microscopy of PEDOT-PSS on GC substrate after 5 million pulses vs. (b) scanning electron microscopy of PEDOT-PSS on Pt substrate after 1 million pulses of stimulation. Note the crack formation in PEDOT-PSS/Pt due to poor adhesion in (b). Adapted from [152] under the creative commons license. (c-h) PEDOT/CNT polymerized on Pt substrate with potentiostatic method and galvanic method respectively. Potentiostatically polymerized coating resulted in a relatively flatter surface d) and exceeded the bounds of the underlying substrate whereas in (e) the galvanostatically polymerized PEDOT/CNT formed a 3D cone shape with increased porosity (f). (g-h) SEM of the same substrate coated with PEDOT-PSS for reference. Adapted from [78] with permission.(i-m) polyimide-based electrode with gold traces was patterned with nanostructured gold polymerized with PEDOT/ ox-SWCNH and PEDOT ox-MWCNT. NTs: nanotubes, NH: nanohorns (j-k). (l,m) Nanoporous morphology of NHs and NTs respectively. Adapted from [161] with permission.

Table 3. Summary of selective CP studies.

Electrode Material	Substrate	Deposition	GSA	Stim Duration	Stim Paradigm	CIL (mC cm ⁻²)	CSC(mC cm ⁻²)	Imp @ 1KHz(Ω)	ECM	In vivo	Ref
PEDOT:pTS	Pt (smooth); Pt (rough)	ED	0.31 mm ²	16 days (2.8 billion stimulation cycles)	Amp: 500 μA W:200 μs PD: 100us	2.09±0.2 (smooth); 2.01±0.4 (rough)	245.59 (smooth) 402.23 (rough)	-	-	-	[151]
PEDOT:ClO ₄	Pt (smooth); Pt (rough)	ED	0.31 mm ²	16 days (2.8 billion stimulation cycles)	Amp: 500 μA W:200 μs PD: 100us	2.39±0.4 (smooth); 2.09±0.5 (rough)	98.49 (smooth) 389.88 (rough)	-	-	-	[151]
PEDOT:PSS	Pt (smooth); Pt (rough)	D	0.31 mm ²	16 days (2.8 billion stimulation cycles)	Amp: 500 μA W:200 μs PD: 100us	1.36±0.1 (smooth); 1.52±0.5 (rough)	105.17 (smooth) 243.48 (rough)	-	-	-	[151]
PEDOT:PSS	Stainless Steel	D	1-2mm ²	300-600hrs	-0.7 – 0.7 V at 50mV/s	-	100	1k	-	Rat, hippocampus	[168]
PEDOT:PSS	ITO	C	0.0025 mm ²	2 mo.	Amp: 0.2V; PW:100μs	-	-	5k	-	-	[143]
PEDOT:PSS	Glassy carbon	ED	300μm. 60μm	65 million cycles	Amp: 1mA; PW: 300μs	-	25.7± 41.6 (300μm) 93.5±137.8 (60μm)	0.9±0.1 (300 μm) 3.6±0.4(60 μm)	Rs(CPE R(W))	Rat, cortex (recording)	[152]
PEDOT:PSS-co-MA	Micro carbon fiber	ED	1076.47 μm ² 472.47 μm ²	6000 pulses	Amp: 50-100 μA PW: 200μs	-	0.5μC; 1.5 μC	~3 Ωcm ²	-	Rat, spinal cord	[147]
PEDOT:PSS-chitosan	Chitosan nano fiber	SC	0.5mm dia.	3 hr	Amp:400mV/cm Freq: 0.5Hz	-	5.704μC	8k	-	-	[169]
PEDOT:PSS	PET/ITO	SC	30μm dia.	-	-	-	-	0.1M	-	-	[157]
PEDOT:PSS + swCNH; PEDOT:PSS + mwCNT	Au	ED	60μm dia. 100μm dia.	5 million pulses	Amp: 6.33mC/cm ² PW: 500μs Freq: 500Hz	NH: 11.6 NT: 8.7	NH: 101.0 ± 18.6 NT: 43.0 ± 14.9	NH: 1.6 ± 0.5 NT: 1.4 ± 0.2	Rs((R1 c1)(R2 CPE1)CPE2(W))	Rat, cortex	[161]
PEDOT:CN T	Pt	ED	200 μm dia.	2 weeks of stimulation after 3 mo. soaking	Amp:0.35mC/cm ² Freq:50Hz	2.5	61.4 ± 6.9	3-7k	Rs(Zd(Cd));	-	[170]

PEDOT:mw CNT	Pt	ED	100 μm dia.	96 hr	Amp: 1mC/cm ² PW: 200 μs . Freq: 50Hz	6.2	38.9 (pot.); 202.9 (galv.)	3.3 \pm 0.2 (pot) 2. 8 \pm 0.1(galv.)	Rs(Zd(Rct CPE2)	Rat, cortex	78]
PEDOT:BF₄	Pt/Ir	ED	6000 μm^2	90min/ day for 15 days	-	-	2.5	20k	-	Rat, STN	153]

Table 3 (continued)

PEDOT:GO	Au	ED	100 μm dia.	1000 cycles	V: -0.6 – 0.8V	4.7	86.75	2.2k	Rs(Cdl Rct)Zd(Cd))		160]
PEDOT:SNP	Au;	ED	2mm ² dia.	24 hrs (4.32 million pulses)	Amp: 4.08 mC/cm ² PW: 1ms PD: 200 μs Freq: 50Hz	4.8 (800s deposition)	1 – 13.1	100	-	CAMP6s Mice, somatosens ory cortex	167]

Rs: series resistance; W: Warburg element; $\Delta\Phi$ indicates the rate of change of phase from capacitive to resistive behaviour of the electrode; Cd: bulk capacitance of electronics

1.4.3 Carbon Materials

Carbon materials offer intriguing properties for electrical micro-stimulation, such as electrochemical stability, capacitive electrochemical behavior, wide electrochemical window, and fast electron transfer kinetics,[18, 152] combined with chemical inertness and biocompatibility.[152] Glassy carbon (GC) electrodes have more than 70% wider electrochemical window and 70% higher CTC (charge transfer capacity) than Pt microelectrodes of similar geometry.[152] Furthermore, they demonstrated a purely capacitive behavior with exceptional stability over prolonged electrical stimulation *in vitro*.[18, 171] sustaining more than 3.5 billion cycles of bi-phasic pulses at a charge density of 0.25 mC cm⁻² without failure.[18] However, smooth carbon materials, such as the flat surface of GC flat surface or 2D graphene, present relatively high impedance and low charge storage capacity compared to high surface area coatings,

and this factor can limit miniaturization. Therefore, high-surface area carbon-based nanomaterials, including carbon nanotube (CNT),^[27] and porous graphene,^{[29] [172] [28]} that combine the properties of carbon with a high surface area, are considered very attractive and have been investigated for microstimulation.^[27, 173]

Table 4 provides a summary of the most recent development in stimulating electrodes using carbon-based materials.

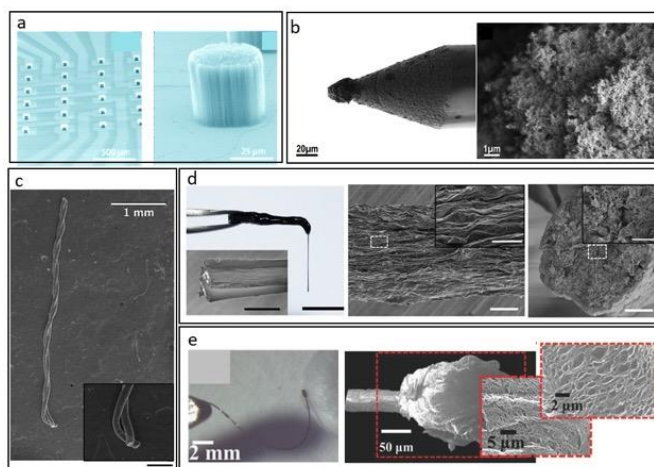


Figure 6. Representative CNT and graphene based electrode materials. (a) Vertically aligned multiwalled CNT pillars microelectrode arrays (left) and magnification on a single pillars microelectrode (right). From ^[173]. (b) Scanning electron microscopy images of microelectrodes coated with carbon nanotubes grown by chemical vapor deposition. From ^[27]. (c) Scanning electron microscopy imaging of two-channel CNT fiber microelectrodes, fabricated by twisting single filaments of a 43 μm diameter CNT fiber, coated with a 3 μm layer of PS-b-PBD; inset shows a close view of the active site. From ^[174]. (d) GF fibers from ^[29] under creative commons licencing: picture of a GF bipolar microelectrode assembly. Inset, SEM image of the GF bipolar microelectrode tip, showing two GFs (bright core) with each one insulated with Parylene-C film (dark shell). Scale bar, 1 cm; inset, 100 μm (left). SEM image of the axial external surface of a GF fiber. Inset, magnified image of the region in the dashed box. Scale bar, 20 μm ; inset, 5 μm . (center). SEM image of the exposed cross

section acting as the active stimulating site of a GF electrode. Inset, magnified image of the region in the dashed box. Scale bar, 20 μm ; inset, 5 μm (right). From [29]. (e) liquid crystal graphene oxide (LCGO) fiber with parylene-C insulation: electrode pressed into clay to demonstrate flexibility and elastic deformation (left). Laser treatment leads to an amorphous electrode with extraordinary surface roughness and porosity (right). From [172].

Vertically aligned multiwalled CNT pillar microelectrode arrays, synthesized by thermal chemical vapor deposition (CVD) presented a relatively high CIL of 1–1.6 mC cm^{-2} , without faradic reactions, and have been demonstrated to be effective in electrical stimulation of primary neurons.[173] (Figure 6a). Fluffy CNT directly synthesized by CVD on the tip of sharp metal microelectrodes (Figure 6b) showing a superior electrochemical stability to electropolymerized CNT nanocomposite coatings through direct comparison on similar microelectrodes.[27] Thanks to the larger exposed CNT morphology, they presented a CIL of 4 mC cm^{-2} , superior to that previously reported for vertical pillars [173], and they withstand a million pulses without any degradation, while all of the other coatings (PPy-CNT and Au-CNT) showed different degrees of impedance variation after stimulation.[27] Nevertheless, CNT synthesis via CVD is not always selective to the microelectrode sites and usually requires very high temperatures ($>650\text{ }^{\circ}\text{C}$) that polymer substrates cannot withstand.[27] Additionally, the catalysts used for CVD, such as nickel, iron, cobalt, and copper, are potentially cytotoxic if not completely removed.[27, 175-177] These limitations do not enable fabrication scalability, and, despite some promising attempts,[27, 178, 179] the acute and long-term performance of these CNT microelectrodes *in vivo* has not yet been demonstrated.

Carbon fiber microelectrodes (CFEs)[180] and CFE arrays[181-185] have demonstrated promising results in seamless electrode tissue interface with markedly reduced immune response due to the subcellular size of each fiber ($\sim 7\text{ }\mu\text{m}$). Indeed, the small feature size of CFE is similar to

the size of a single trace of a conventional silicon neural probe, but they are sufficiently robust and flexible as a stand-alone electrode. For example, single CFEs with parylene C insulation and PEDOT:PSS recording site, have been used as subcellular-scale probes for electrophysiological recordings, demonstrating promising results in chronic *in vivo* recordings [180]. Furthermore, these micro-invasive probes provided stable monitoring of sub-second evoked DA fluctuations in rats for over a year [186] and in non-human primates for over 100 days [183]. However, due to the smooth surface of the carbon fiber, CFEs require low impedance coating such as PEDOT:PSS, [180] PEDOT/pTS,[187], or electrodeposited Pt/Ir [187] to enable high SNR recordings and their CIL is insufficient for stimulation (0.05 mC cm^{-2}).^[29] CNT fibers (18 μm diameter, Figure 6C), consisting of bulk-grown CNTs, have been produced by high-throughput wet spinning, and then individually insulated with a $\sim 3 \mu\text{m}$ layer of a copolymer of polystyrene–polybutadiene (PS-b-PBD), leaving only the tip exposed. The resulting electrically active sites, due to the porous surface area, have shown remarkable electrochemical properties, i.e., low impedance ($20.44 \pm 8.2 \text{ M}\Omega\mu\text{m}^{-2}$), wide water window (-1.5 to 1.5 V), high CIL (6.5 mC cm^{-2}),^[174] and excellent electrochemical stability under prolonged current pulsing (97M cycles beyond the water window limits).^[174] *In vivo*, CNT fiber microelectrodes were demonstrated to be able to deliver efficacious DBS in a Parkinsonian rat model and presented a superior biocompatibility in comparison to PtIr microwires implanted in the same animals for 6 weeks.^[174] This study highlighted the promising potential of using CNT fiber for effective long-term stimulation use. Additionally, in the same study, CNT fibers have been successfully used to record stable neural activity for weeks, showing potentiality for bidirectional access to the brain. However, as mentioned before, common CNT production and fiber assembly via wet spinning are laborious and involves the use of metal catalysts, limiting the widespread use. A dry spinning method which directly synthesizes CNT arrays free of catalyst may eliminate this

concern. Further, the dry spun CNT fibers can be assembled at up to 16 m s^{-1} linear speed, offering great potential for mass production. The proof of concept dry-spun CNT fiber arrays (CIL:15.09 mC cm^{-2}) for neural stimulation in Madagascar hissing cockroach has been demonstrated recently,[188] motivating future testing for long-term stimulation performance in higher order animal models.

Similarly, porous graphene fibers (GF, $\sim 75 \mu\text{m}$ diameter)^[29] have been prepared through a dimension-confined hydrothermal process from aqueous graphite oxide (GO) suspensions, and then individually insulated with parylene-C film of $\sim 5 \mu\text{m}$ thickness (Figure. 6d). They have a wide water window of -1.5 to 1.3 V , a CIL of 10.1 mC cm^{-2} , capacitive charging/discharging mechanism, and excellent electrochemical stability under overcurrent pulsing (total of 205.2 M pulses, 19 days).^[29] *In vivo*, these fibers microelectrodes demonstrated the capability for efficacious DBS in hemi-Parkinsonian rats, verified during artifact-free MRI image acquisition.^[29] The high charge-injection-capacity of the GF electrodes enabled the use of relatively small electrodes without compromising the stimulation efficacy, important for maintaining a small artifact size of the MRI and providing high selectivity and spatial resolution of microstimulation.^[29] Graphene fibers have also been fabricated using wet spinning of graphene oxide (GO) liquid crystal phases,^[172, 189] also in this case, they presented highly porous surface area, high CIL, low impedance and have been used to stimulate live retina *in vitro* (Figure 6e).^[172]

A common issue for carbon, CNT and graphene fiber is that current methods of assembling fibers into multielectrode arrays is semi-manual and does not permit reproducible high-density 3D microelectrode array configuration or production scale up. The promising micro-stimulation performance and stability of porous carbon materials present an urgent need to develop scalable synthesis and fabrication process for carbon-based MEAs. While growing porous carbon on metal

electrode sites had demonstrated the benefit of carbon, the bonding between porous carbon and the underlying metal may be prone to delamination under repeated stimulation or mechanical bending due to the electrical and mechanical mismatch. Additionally, the high temperature required for the synthesis of carbon and nanocarbon limits the choice of the substrate materials, making patterning nanocarbon materials on multi-channel large scale configurations on flexible substrate extremely challenging.[27, 190]. Thus, most demonstrations have been performed on single wire penetrating electrodes [27] or *in vitro* non implantable MEAs on silicon wafers [173].

The best scenario may be to fabricate carbon based MEAs that integrates high density carbon microelectrode arrays and interconnections on flexible polymeric substrates, eliminating the mismatched layers, such as intermediate adhesion of conductive metal layers. This possibility will remove the sources of potential mechanical or electrical discontinuities and failure under prolonged electrical and mechanical solicitations, improving the microstimulation performance together with the device biocompatibility.

There have been recent attempts to develop microfabrication techniques to yield arrays of carbon electrodes on flexible substrate for microstimulation applications. These attempts use the pattern transfer technique of pre-pyrolyzed GC microelectrodes on polyimide substrates (Figure 7a,b),[18, 171, 191] direct laser pyrolysis of porous graphene on polyimide substrate (Figure 7d-f),^[28] or laser carbonization of parylene C (Figure 7c).[192] As previously mentioned, GC shows outperforming properties compared with Pt microelectrodes of similar geometry in terms of electrochemical stability.[152] The GC microelectrodes have been recently miniaturized and GC MEA intracortical probes demonstrated the capability to record high quality single-unit neural activity and to detect low dopamine concentrations *in vitro* and *in vivo*,[18, 191, 193, 194] offering great promise for multimodal interaction with the brain. Besides glassy carbon, porous graphene

electrodes obtained by laser pyrolysis and subsequent doping with nitric acid exhibited a CIL of 3.1 mC cm^{-2} and very low impedance (519Ω at 1 kHz for $250 \mu\text{m}$ diameter electrodes), which remained relatively stable in PBS solution over 28 days, and showing no physical degradation after 1 million cycles.[28] Additionally, graphitic carbon obtained by inducing the laser carbonization of parylene C on top of robust metal sheets (e.g., platinum/iridium tracks) has maintained stability by aging in $30 \text{ mM H}_2\text{O}_2$ for one week, or by 10 million pulse (biphasic, $39.5 \mu\text{C cm}^{-2}$) of electrical stimulation.[192] To date, laser pyrolysis fabrication has been reported only for micro-ECoG devices with relatively big electrodes ($200\text{-}700\mu\text{m}$ diameter).[192] Indeed, the main limitation of this technology is the laser resolution which needs to be drastically improved for miniaturization and high-density arrays.

Most of these mentioned MEAs use metal interconnections, which present mechanical and electrical mismatch issues between the metal interconnections and the carbon electrodes under prolonged electrical stimulation and mechanical stresses. To the best of our knowledge, there is only one case of a microfabricated MEA that uses GC for the microelectrodes, traces, and bonding pads, made by a single and homogeneous GC material integrated on a flexible polyimide substrate (Figure 7g-j). These all-GC probes were fabricated using a double-sided 2-step lithographic technique that allows transferring pre-patterned GC structures into a polymeric substrate and insulation layers.[18] Other than recording and sensing capability, these MEAs demonstrated to be capable of delivering charge-balance current pulsing over 3.5 billion cycles in extended accelerated aging process lasting more than 1000 hours, without failure at the GC and polyimide interface.[18] This study suggests a stronger electrochemical and mechanical robustness of probes made from a single carbon material without any metal interconnection or surface coating and

encourage the investigation of new and simplified technique for the scale up and batch-fabrication of all-carbon devices.

Looking into this direction, the optimization of laser technique would allow for fast, low-cost batch-fabrication of patterned microelectrode arrays and conducting traces on free-standing polymeric films, without the need of high-temperature carbon synthesis, such as pyrolysis or chemical vapor deposition, or multistep photolithographic microfabrication processes. Furthermore, a localized rapid heating by laser rastering can potentially enable a precise control of the atomic structure, nanoscale morphology, and micron-scale geometry of nanocarbon microelectrodes, opening the door for unprecedented ability to tune and optimize the morphology and performance of nanocarbon MEAs.

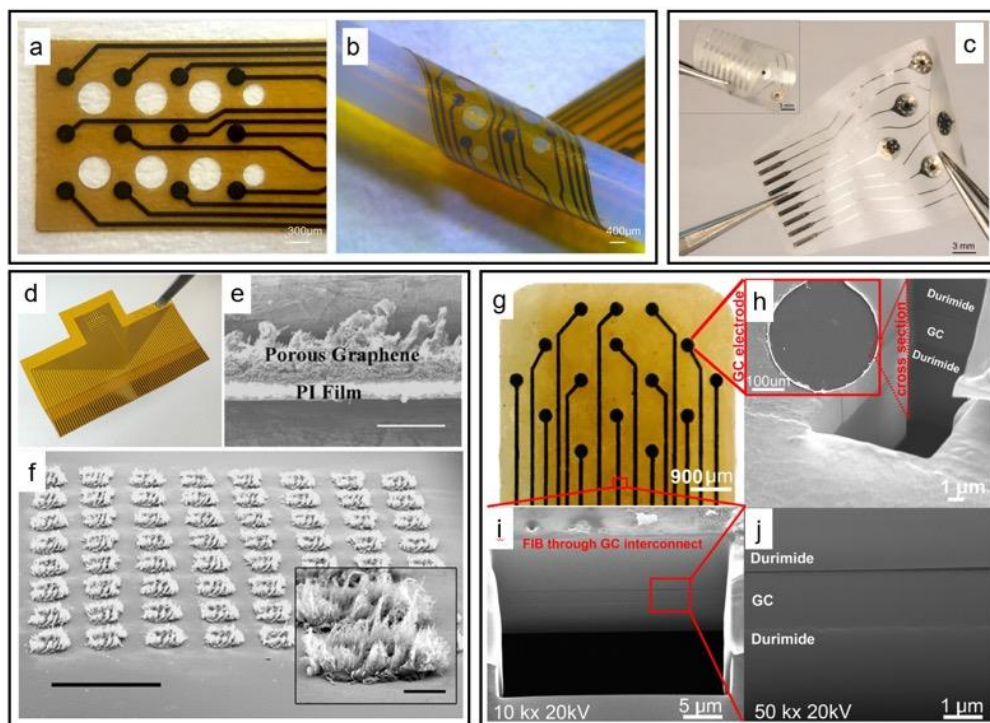


Figure 7. Representative GC based electrode arrays. (a) GC 12 electrode array and (b) the device is folded to show its flexibility. From [152]. (c) 9-electrode array (curled in the inset) From [192] under creative commons licensing. (d) Photograph of a fabricated 64 porous graphene electrode array. (e) SEM image of the cross-section view of porous graphene. Scale bar: 100 µm. (f) Tilt SEM image of a 64-spot porous graphene array. Scale bar: 1mm. The inset is the SEM image of an individual spot. Scale bar: 100 µm. From [28] under the creative commons licensing. (g) 15-channel GC ECoG probe, (h) In inset: Magnified SEM image of a single microelectrode in the ECoG probe. Also, FIB cross-section of the GC microelectrode taken at the edge between GC and Durimide is shown revealing a seamless integration of the layers. (i) Expanded view of FIB cross-section taken at a GC wire trace leading to one of the microelectrodes, (j) High-resolution (50,000×) FIB image of a cross-section taken through a GC wire trace. Box in bottom of (i) shows the location where FIB through GC interconnect was taken. Note that there are no adhesion layers or metal layers in all GC (aGC) probes. From [18] under the creative commons licensing.

Table 4. Summary of studies using carbon-based materials

Electrode Material	Substrate	Deposition Method	GSA [cm ²]	Stim Duration	Stim Paradigm	CIL [mC cm ⁻²]	CSC [mC cm ⁻²]	Impedance @ 1kHz [kΩ]	ECM	In vivo	Ref
GC	GC	pyrolysis	70650 (300 μm dia.)	3.5 billion cycles (1000 hours)	0.25 mC cm ⁻² , Ampl.: 450 μA Pw: 400 μsec		61.4 ± 6.9	5.8 ± 1.2	Rs (CPE (Rct)(W))	-	[18]
porous graphene	-	direct laser pyrolysis	62500	1 million cycles.	Amp: 0.75 mA Pw: 400 μs	3.1	50 100 mVs ⁻¹	2 to 8	-	pial surface of the motor cortex	[28]
CNT fibers	-	high-throughput wet spinning of bulk grown CNTs	1450	97M cycles (9 days)	Pw: 60 μs Freq: 130 Hz.	6.52	372 ± 56	11.2 ± 7.6	-	psilateral entopeduncular nucleus	[174]
Graphene fibers	-	one-step dimensionally confined hydrothermal process using suspensions of graphene oxide	1406.2 (75 μm dia.)	19 days	Pw: 60 μs Freq: 130 [Hz].	10.1 ± 2.25	889.8 ± 158.0 (cathodic)	15.1 ± 3.7	-	Yes subthalamic nucleus (STN) in Parkinsonian rats	[29]
Reduced Graphene Oxide	-	wet-spun from liquid crystal line (LC) dispersions of GO and Laser treatment	1923 (50 μm dia. Before laser treatment)	-	Amp: 103 ± 87 μA Pw: 500 μs	14 ± 0.9 to 6 ± 2.9	-	4	Rs CPE	Retinal ganglion	[172]
CNT	Pt	CVD	923 ± 70 μm ²	1 million pulses	1.6 mC cm ⁻² mp.: A P w: 100 and 500 μs.	4	58.5 ± 10.6	59.6 ± 11.2	-	-	[27]
MWCNT pillars	polysilicon	CVD	5700 μm ²	-	Amp. 80 μA Pw: 1 ms	1–1.6	-	-	Rs (Zf CPE)	primary neurons cultures	[173]

Table 4 continued

Hybrid diamond/ carbon fiber	-		3200	-	-	25.08 ± 12.37	-	-	Rs(Cc Rp (Ccor Re))	retinal cell culture s	195]
------------------------------------	---	--	------	---	---	------------------	---	---	-------------------------	---------------------------------	------

Rs: solution resistance; Rct: charge transfer resistance; CPE: constant phase element; W: Warburg element; Zf: spreading resistance

1.5 Dissertation Organization

The design for chronic and stable stimulating neural interfaces requires understanding of electrical properties of emerging novel materials and biological responses these materials under electrical stimulation. This dissertation employs a multimodal approach from electrochemistry, electrophysiology, *in vivo* imaging, and finite element modeling to study electrical stimulation efficiency and stability.

In chapter 2, the work is focused on studying the efficiency of electrical stimulation with high performing thin-film coatings—iridium oxide and PEDOT/CNT, using *in vivo* imaging in mice with transgenic expression of a fluorescent calcium indicator in neurons. *In vivo* imaging affords the opportunity to directly visualize the effect of electrical stimulation. We analyze the image data to understand the intensity and spread of electrical stimulation. In this study, we also investigated the effect of the number of shanks of planar electrodes on electrical stimulation. The results from this chapter provide visualization and quantification of stimulation efficiency of electrical stimulation from novel materials, and electrodes with different shank numbers which has not been investigated previously.

Chapter 3 focuses on understanding electric field distribution from stimulating IrOx and PEDOT/CNT electrodes, using finite element analysis. In this chapter we expand upon the

discussions in Chapter 2 and create a simulation of voltage field resulting from stimulating disk electrodes with different roughness to emulate IrOx and PEDOT/CNT in brain tissue. Results from this chapter will provide a theoretical basis and understanding for observations and conclusions in Chapter 2.

In chapter 4, we report results from chronic investigations of *in vivo* microstimulation using a multimodal approach. Specifically, we imaged electrically evoked brain activation from IrOx and PEDOT/CNT, additionally, we collected electrochemical measurements, awake spontaneous electrophysiological recording, weekly, up to three months. Results from this work will provide insight into the stability of electrical stimulation, particularly the time course of change in stability from acute, sub-acute, and the chronic time point.

2.0 Imaging the Efficiency of PEDOT/CNT and Iridium Oxide Electrode Coatings for Microstimulation

2.1 Chapter Overview

Electrical microstimulation has shown promise in restoring neural deficits in humans. Electrodes coated with materials like the conducting polymer poly(3,4-ethylenedioxythiophene) doped with acid functionalized carbon nanotubes (PEDOT/CNT, or PC) exhibit superior charge injection than traditional metals like platinum. However, the stimulation performance of PC remains to be fully characterized. Advanced imaging techniques and transgenic tools allow for real time observations of neural activity *in vivo*. Herein, microelectrodes coated with PC and iridium oxide (IrOx) (a commonly used high-charge-injection material) are implanted in GCaMP6s mice and electrical stimulation is applied while imaging neuronal calcium responses. Results show that PC coated electrodes stimulate more intense and broader GCaMP responses than IrOx. Two-photon microscopy reveals that PC coated electrodes activate significantly more neuronal soma and neuropil than IrOx coated electrodes in constant-voltage stimulation and significantly more neuronal soma in constant-current stimulation. Furthermore, with the same injected charge, both materials activate more spatially confined neural elements with shorter pulses than longer pulses, providing a means to tune stimulation selectivity. PC coating can significantly improve energy efficiency for electrical stimulation applications.

2.2 Introduction

Electrical microstimulation is a technique to activate a small population of neurons by passing currents through a micro-electrode. In neuroscience research, microstimulation is used to study neural circuits, evaluate connected networks and modulate behaviors.[1-3] In humans, electrical microstimulation has been used to partially restore vision,[11, 14, 90, 196-198] hearing,[199] movement,[6] and sensation.[7, 200] Moreover, electrical stimulation, or bioelectronic medicine, has become an emerging alternative or complement to costly biologic drugs for the treatment of health issues such as arthritis, [201]asthma,[202] diabetes,[203] and digestive disorders. [9]

Traditionally, microelectrodes are made up of metals with geometric surface areas between $2000\text{-}10000\mu\text{m}^2$ [12], which are much smaller than macroelectrodes used for deep brain stimulation[13]. This small electrode size offers increased spatial selectivity of the neural tissue but requires higher charge density which often exceeds charge injection limits for safe stimulation. Efficient and safe electrical stimulation requires sufficient charge without exceeding potentials for irreversible chemical reactions[12]. Platinum (Pt) is widely used for auditory[204] and visual prostheses [14]. However, new generations of auditory and visual prostheses are requiring higher channel counts with smaller electrodes for increased spatial selectivity and the charge injection limit (CIL) of conventional Pt electrodes is below the threshold for activation of these applications. Therefore, there is a critical need for higher CIL electrode materials. Examples of such materials are iridium oxide (IrOx)[15, 16, 73, 133], titanium nitride (TiN)[17], glassy carbon[152], and nanostructured Pt[205]. These materials have shown dramatic improvement in CIL, on the order of mC/cm^2 , higher than smooth Pt ($35\text{-}100\mu\text{C}/\text{cm}^2$) *in vitro*, owing to the increased electrochemical surface area. Particularly, IrOx has become more prevalent for neural stimulation electrodes in a

variety of animal and human stimulation studies. [206, 207] However, the high CIL of IrOx has been reported to decrease substantially over time and long-lasting high CIL stimulation (for over 7 hrs) has led to IrOx degradation with adjacent neuronal degeneration [208], highlighting the importance of developing and evaluating new materials for electrical microstimulation. Conducting polymers (CP) such as poly(3,4-ethylenedioxythiophene) (PEDOT) are polymers with a conjugated backbone of alternating double and single bonds. Electrical conductivity is achieved by doping the polymer with negatively charged ions (counter ions or dopants). By coating CPs onto metal substrates, we have drastically reduced electrical impedance and improved neurophysiological recording capabilities [86, 102, 145, 209-211]. The increased electrochemical surface area and decreased impedance make PEDOT an ideal candidate for electrical stimulation [74, 130, 151, 169, 170, 212]. Functionalized carbon nanotubes (CNTs) have been increasingly popular for their intriguing properties as a dopant for PEDOT [23, 24, 86, 161, 213, 214]. The incorporation of CNTs not only significantly increases the electrochemical surface area thereby increasing the electrical conductivity of the electrode surface, but also improves the mechanical and electrochemical stability of the PEDOT coating during prolonged stimulation. [23, 24] For most of these emerging stimulation materials, comprehensive evaluation of their microstimulation efficiency, safety, and longevity *in vivo* remain to be completed.

Examining the effects of electrical stimulation *in vivo* have been limited to electrophysiology [213, 215, 216], behavior [57, 63, 217, 218], and endpoint histology [63, 101, 219, 220]. While these robust methods provide users with a functional and histological understanding of electrical stimuli, they do not provide direct visualization of the cellular response in real-time. Recent advancements in *in vivo* imaging techniques, such as mesoscale fluorescence microscopy and two-photon microscopy (TPM), coupled with newly developed genetically

engineered rodent models expressing fluorescent calcium indicators allow for the direct visualization of neuronal activity in response to electrode implantation and stimulation *in vivo*. [118, 221] Using *in vivo* two-photon calcium imaging in mice, rats, and cat models, Histed et al revealed a sparse, distributed population of cortical neurons by electrical microstimulation via glass pipettes containing tungsten and platinum-iridium microwire electrodes [114]. In more recent studies, the Kozai group utilized mesoscale fluorescence microscopy and two-photon imaging to investigate the calcium responses to prolonged electrical stimulation in Thy1-GCaMP6s mice and reported the effect of stimulation frequency, [115] pulse symmetry, and phase order, [116] using Michigan planar arrays. [117] These studies demonstrate the capability of fluorescence imaging to characterize the neuronal response to stimulation at cellular and mesoscopic spatial scales *in vivo*.

In this work, we evaluated the effects of intra-cortical microstimulation from electrode arrays coated with PEDOT/fCNT (referred to as PC from hereon) and IrOx using mesoscale fluorescence imaging and two-photon imaging in awake, head-fixed Thy1-GCaMP6s mice. In particular, we aimed to examine and characterize differences in stimulation efficiency from these two materials determined by the cortical response amplitude, radius and selectivity of the stimulated region to various stimulation paradigms.

2.3 Materials and Methods

2.3.1 Electrode modification

Two probe geometries were used in this study, both from NeuroNexus (Ann Arbor, MI), four-shank iridium probes with 4 sites per shank (A4x4-3mm-100-125-703; n=5) and single-shank

iridium probes with 16 sites (A1x16-3mm-50-703; n=5). Both probes were 3 mm long with 703 μm^2 site area. The shank pitch for the four-shank probes was 125 μm . Each electrode site was cleaned with isopropanol and rinsed with deionized water before electrode surface modification. Activation of iridium was done by delivering voltage-controlled biphasic pulses from -0.8 V to 0.9 V at a 50% duty cycle for 3200s per site to maximize charge storage capacity. PC was prepared in 0.02M EDOT and 2mg/ml of acid functionalized carbon nanotubes (CNTs) using chronocoulometry using our published protocols[23].

2.3.2 Electrochemical characterization of modified electrodes

All *in vitro* measurements were performed using a three-electrode set up in PBS using Ag/AgCl as reference and Pt foil as the counter electrode. *In vitro* characterizations consisted of electrical impedance spectroscopy (EIS), cyclic voltammetry (CV), and charge injection limit (CIL). EIS was measured by applying a 10-mV signal from 10-40,000 Hz. CV was measured to calculate the charge storage capacity and to identify the electrochemical signatures of the coated materials (-0.7 V to 0.8 V at 1V/s scan rate). CIL was performed by delivering a bi-polar asymmetric current-based waveform (identical to the ones used for *in vivo* experiments in this work) and measuring the voltage excursion. From the voltage excursion, we can determine the charge density at which the Emc (defined as the difference in between the maximum cathodic voltage and the access voltage) exceeded -0.6 V for IrOx[12]. The Emc for PC was estimated to be -0.9V based on CV. [222] *In vivo* electrochemical characterization followed the same parameters as the *in vitro* set up except that a two-electrode set up was used with the reference and counter electrodes shorted to a skull screw in the contralateral cortex. All electrochemical data were collected using the Autolab potentiostat.

2.3.3 Animal Surgery

Ten male GCaMP6s mice, C57BL/6J-Tg(Thy1-GCaMP6s) GP4.5Dkim/J (also known as GP4.3) mice were purchased from the Jackson Laboratory (Bar Harbor, ME). Animals were anesthetized with 75mg/kg ketamine and 7.5 mg/kg xylazine cocktail for cranial window surgery and electrode implantation following aseptic procedures. The electrode arrays were sterilized by ethylene oxide gas 48 hrs prior to surgery. A reference screw was placed in the contralateral hemisphere and secured using UV-curable dental cement (# 062066 Henry Shein). A high-speed dental drill was used to remove the parietal bone over the somatosensory cortex. Electrodes were implanted at a 30° angle and inserted at a speed of 100-200 $\mu\text{m/s}$ for 600 μm . Upon electrode implantation, a transparent silicone elastomer was used to seal the cranial window, covered by a 3x3mm² glass coverslip. The electrode was dental cemented in place and the animal was allowed to recover and followed up with three days of analgesic and antibiotics.

2.3.4 Imaging and electrical stimulation

Images sensitive to GCaMP fluorescence over the exposed brain including the implanted electrode were acquired by widefield fluorescence imaging using a macroscope (MVX-10, Olympus, Inc.) and high-sensitivity camera (CoolSnap HQ2, Photometrics, Inc) controlled by MetaMorph software. Time series images were acquired at 10 Hz. In addition, images of neurons expressing GCaMP6s around the implanted electrode were acquired by two-photon microscopy (Ultima IV, Bruker Nano, Inc) coupled to an ultra-fast laser (Insight X3, Newport Spectra-Physics, Inc.) using a 16x 0.8NA objective lens (Nikon, Inc.). The laser was tuned to 920nm and time

series were acquired with $1.27 \times 1.27 \mu\text{m}/\text{pixel}$ resolution at 3 fps to capture GCaMP temporal responses.

Electrical stimulation was delivered using the Ripple GrapeVine system (Nano2+stim Ripple LLC, Salt Lake City, Utah) via a 32 channel to 16 channel Omnetics adapter. The stimulation waveform was a charge-balanced cathodic leading waveform (cathodic width: $100 \mu\text{s}$; interphase delay: $100 \mu\text{s}$; anodic phase: $200 \mu\text{s}$). Stimulation was delivered at 50 Hz varying the amplitude of the cathodic phase from $5 \mu\text{A}$ to $60 \mu\text{A}$ over different trials in the same session. Each stimulation trial consisted of a 1-second ON period, and 3-second OFF period, repeated six times per electrode site. The energy for current controlled stimulation was calculated by integrating absolute value of the product of voltage and current over a single pulse duration ($300 \mu\text{s}$ ON period). For the delivery of a voltage-controlled stimulus, an Autolab potentiostat (PGSTAT302N) was used in galvanostatic mode. The voltage pulse was biphasic with cathodic leading followed by an anodic phase twice the duration at half the amplitude, with the same pulse duration and trial repetition parameters. The electrical stimulus was synced to beginning of both imaging methods using a National Instruments board (PCI-6601, Austin, TX) to monitor the start-of-frame trigger from each system to deliver TTL pulses for each stimulation trial.

2.3.5 Image analysis

All analyses were performed in MATLAB. Wide-field fluorescent time series were binned by a factor of 2 for a final resolution of $15 \mu\text{m}/\text{pixel}$ to increase signal to noise ratio and reduce computational load. Quantification of GCaMP response to electrical stimulation were performed on the mean of the six trials from each stimulation amplitude and stimulating electrode. Amplitude and extent of activation were extracted from the stimulation evoked responses. For this analysis,

the images were cropped centered on the electrode for a final square region covering (1.2 x1.2 mm²). The response amplitude (change in GCaMP fluorescence or $\Delta F/F_0$) was calculated by subtracting and dividing the mean of the initial 30 s baseline before electrical stimulation. Z-scores were calculated by dividing by the standard deviation during this baseline period. For each stimulated trial, A 2-D exponential decay function (1) was fitted to the maximum GCaMP response during the 1-second stimulation period. Where A is the amplitude of the background subtracted GCaMP response, \mathbf{r} is a vector representing the space of the activated region, \mathbf{r}_0 represents the position of the center of the GCaMP response and w is the radius of GCaMP response. We report the amplitude and extent (radius) of stimulation-evoked GCaMP responses for those trials where the model explained at least 25% of the variance. Additionally, for instances where the GCaMP response amplitude is small or indifferent from noise, the algorithm ascribed near-flat profiles to the data with artificially large radii (w). Considering that the model can reliably capture radii (w) up to 1/3 of the half width of the field of view, we labeled trials with GCaMP radii larger than 1/6 the width of the field-of-view as noise and excluded them from further analyses.

$$Y(\mathbf{r})= Ae^{-(r-r_0)/w} \quad (2-1)$$

Neuronal expression of GCaMP across the mouse cortex is not homogeneous[223]. To enable comparison between PC and IrOx in nearby but different depth location, we normalized the GCaMP intensity and radius from PC sites to their immediate distal IrOx sites for linear arrays. For four-shank arrays, the normalization was performed by taking the ratio of PC sites to their parallel IrOx sites in the same position. For example, in 4x4 arrangement where sites (1,1) and (1,3) are coated with PC and sites (1,2) and (1,4) are coated with IrOx, the normalizations were (1,1) / (1,3) and (1,2) / (1,4).

The two-photon imaging was analyzed to quantify the number and location of electrically activated somas using custom MATLAB algorithms. The time-series images were corrected for motion before analysis. Change in fluorescence was calculated by subtracting and dividing the 30 s of baseline period before electrical stimulation. Neuronal somas were segmented from the average time series image based on a local intensity threshold. Low-frequency intensity variations were removed from the average image using a high-pass filter to help identify and segment GCAMP-expressing neuronal soma. Electrically activated neurons were determined by correlating the stimulus temporal waveform with the time series from segmented neuronal ROIs resulting in an r-score (r), which were transformed to t-scores to evaluate significance (one-sided t-test $p < 0.05$). [224] We Bonferroni corrected the p value by the total number of ROIs to account for multiple comparisons. Neuropil fluorescence consists of the dense network of dendrites and synapses and out of plane cell bodies within the field of view. We quantified neuropil fluorescence by subtracting the segmented somas from the time series.

Maps of the threshold current for activating neural elements near the electrode were generated by first obtaining a binary map of pixels that are significantly activated by electrical stimulation and labeling the activated pixels by the lowest current amplitude at which they are activated. To obtain the change in threshold current as a function of distance away from the electrode center, the images were binned with concentric circles in intervals of $15\mu\text{m}$ per bin ($1.27\mu\text{m}$ per pixel). We define the average spatial selectivity ($\mu\text{A}/\mu\text{m}$) as the slope of threshold current versus distance away from the center of the electrode for each pulse width.

2.3.6 Statistics

Two-way ANOVA was used for the following statistical comparisons: (1) the effect of electrode material on GCaMP intensity and radius as a function of increasing stimulation current amplitude, (2) the effect of electrode geometry on GCaMP intensity and radius as a function of increasing stimulation current amplitude, and (3) the effect of electrode material on activated neuron soma and neuropil intensity for different stimulation pulse widths. A *p-value* of less than 0.05 was deemed significant. A Wilcoxon signed-rank test was used for testing the effect of electrode material on normalized GCaMP intensity and radius. A two-tailed student t-test was used for testing the effect of electrode material on activated soma and neuropil intensity for voltage controlled and current controlled stimulations. A *p-value* of less than 0.05 was deemed significant. Linear regression was used to investigate the relationship between the average spatial selectivity and pulse width, a *p-value* of less than 0.05 for the slope was deemed significant. All sample sizes are denoted in the captions of respective figures.

2.4 Results

2.4.1 Electrode modification and characterization

Electrode modification consisted of first electrically activating the iridium to form IrOx thin films on half of the sites, followed by coating on alternating sites with PC (Figure 8a, see materials and methods for details). IrOx and PC were coated on four-shank (Figure 8b) and single-shank (Figure 8c) arrays, respectively. Modified electrode sites have contrasting features under a

brightfield microscope, IrOx thin films appear blue and PC coatings have a characteristic black and fuzzy appearance (Figure 8(b-d)).Before implantation, the electrochemical properties of the IrOx and PC were characterized since modified electrodes have distinct electrochemical signatures (Figure 9). Error! Reference source not found.a,b shows the impedance modulus and phase of IrOx and PC coated sites, respectively. The impedance modulus of IrOx sites was reduced with increases in frequency and absent of a frequency-independent region. Additionally, the IrOx sites exhibited a relatively stable phase shift ranging between 60 to 30 (-degrees) over the frequency spectrum. In contrast, PC sites showed significantly lower impedance modulus than IrOx, with a frequency-independent region of impedance modulus between 100 to 40kHz, as well as a shift in phase angle from 80 (-degrees) at low frequencies to ~15-20 (-degrees) at high frequencies. The lower cut-off frequency of PC (the frequency at which the impedance becomes purely resistive) indicates a higher capacitive charge transfer likely due to increased effective surface area of the PC electrodes which is consistent with the SEM observation (Figures S1). Figure 9d shows Nyquist plots of PC and IrOx. The linear region for both materials represents a constant phase element with a phase angle of 45 degrees, indicating a highly contorted surface. Moreover, we characterized the IrOx and PC coating with cyclic voltammetry (CV). Figure 9c shows a representative CV curve of an IrOx site (blue) and a PC site (black). PC CV curves demonstrate a shape that is stereotypical of PEDOT based coatings in that the curve has broad shoulders and no distinct redox peaks within the CV potential limits (-0.7V to 0.8V). On the other hand, IrOx undergoes reversible oxidation and reduction within this potential window. Particularly peaks A, C indicates the oxidation (0.3V) and reduction (-0.25V) of iridium between Ir³⁺ and Ir⁴⁺ states respectively, peaks B, D indicate the oxidation and reduction of iridium at 0.6 V between Ir⁴⁺ and Ir⁵⁺ states, respectively. The charge storage capacity is similar between the two site materials. Relevant electrochemical quantifications

are reported in Table 5. Voltage transients to applied current are shown in Figure 9e. Charge injection limits for IrOx were estimated by dividing the cathodic charge at which E_{mc} reaches -0.6V by the geometric surface area of the electrode(Table 5). *In vivo* measurements of IrOx and PC electrodes show similar electrochemical features as observed *in vitro* Figure 9f,g. Additionally, the peak-to-peak voltage in response to current pulsing results in a smaller amplitude than IrOx. Furthermore, by pulsing both materials with the same biphasic voltage pulse, the resulting current excursion shows a higher peak to peak amplitude in PC than IrOx (Figure 9i).

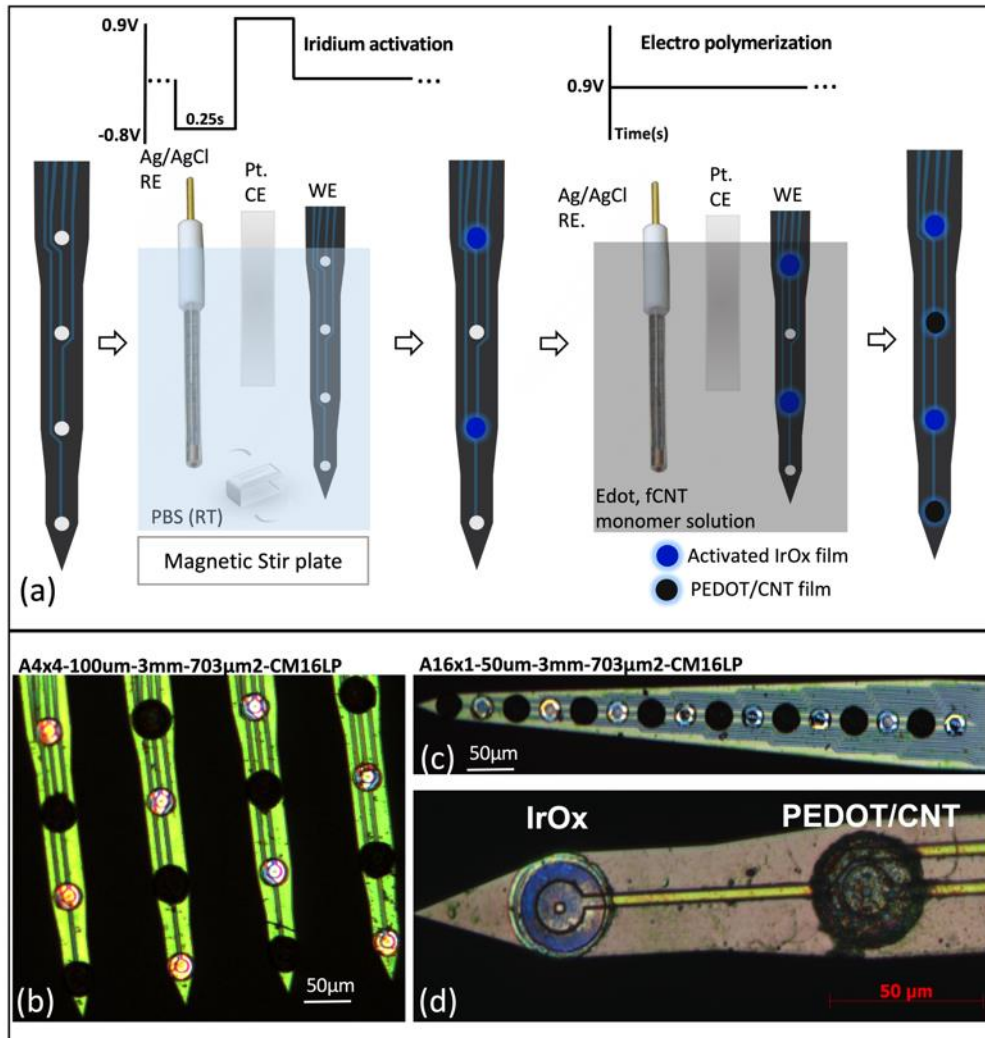


Figure 8. Electrode modification. (a) schematic depicting the electrode modification procedure. (b-c) Optical micrograph of a four-shank and a single-shank electrode with alternating sites coated with IrOx or PC. (d) Higher magnification of IrOx and PC sites showing surface features under a brightfield microscope. IrOx appears blue and PC appears black and fuzzy.

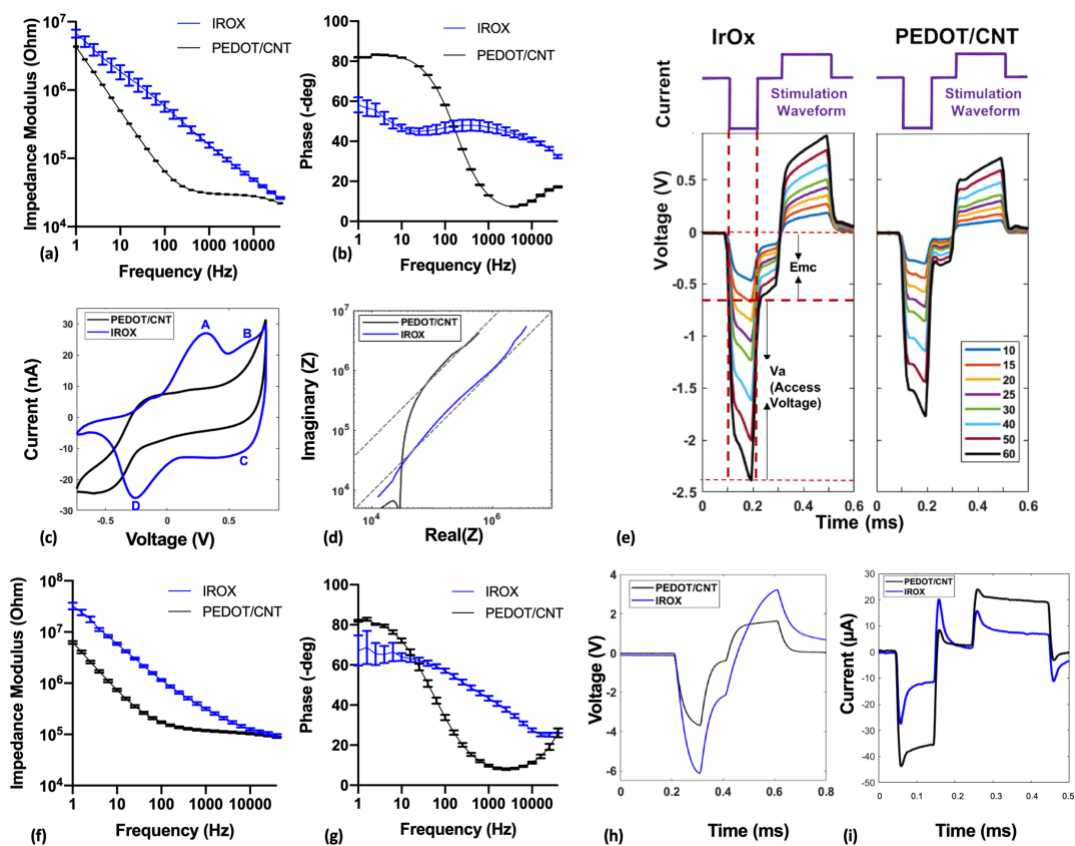


Figure 9 Electrochemical characterization. (a, b) Impedance modulus and phase of IrOx and PC (denoted PEDOT/CNT in the legends) electrodes ($n = 8$ for each material type) in PBS. Error bars represent the standard error of the mean. (c) Cyclic voltammetry of a representative PC and IrOx electrode site in PBS. A, D, B, C denote the oxidation and reduction peaks of iridium between Ir^{3+} to Ir^{4+} and Ir^{4+} to Ir^{5+} states, respectively (d) Mean Nyquist plot of PC and IrOx sites ($n = 8$ for each material type) in PBS. (e) Voltage excursions of a representative IrOx site (left) and a PC site (right) in response to current pulses from 10 to 60 μA in PBS (colored legends). V_a represents access voltage and E_{mc} represents the electrode polarization voltage used for the calculation of charge injection limits. (f, g) Impedance modulus and phase *in vivo*. (h) *In vivo* voltage transient as a result of a 30 μA stimulus. All black traces represent PC and all blue traces represent IrOx except for panel (e). (i) Current excursion as a result of a 3V biphasic pulse measured at a representative PC and IrOx site.

Table 5. *In vitro* Electrochemical Properties. Asterisks denote values normalized to the enlarged PC surfaces.

	Charge Storage Capacity (mC/cm ²)	Impedance at 1kHz (kOhm)	Charge Injection Limit (mC/cm ²)
IrOx	25.1±1.9	136±9.3	1±0.12
PC	26.4 ± 0.4; 21.12±0.3*	45±0.13	5.68±0.13; 4.54±0.1*

2.4.2 Meso-scale imaging of GCaMP response to electrical stimulation

We coated the conducting sites of NeuroNexus multielectrode arrays with IrOx and PC and implanted them into the somatosensory cortex of GCaMP6s mice. The arrays were interfaced with the stimulation hardware via a 16- channel Omnetics connection. We stimulated each electrode site with biphasic, charge-balanced, cathodic leading pulses ranging from 0.5 nC/ph to 6 nC/ph. Stimulations were administered at random for *low* (0.5 – 4nC/ph) and *high* (4.5nC/ph – 6nC/ph) charge densities for 1 second on and 3 seconds off while the animal is awake and head-fixed on a treadmill (Figure 10). Evoked neuronal activity for both probe styles was measured via GCaMP fluorescence changes through the cranial window (Figure 10 b,c).

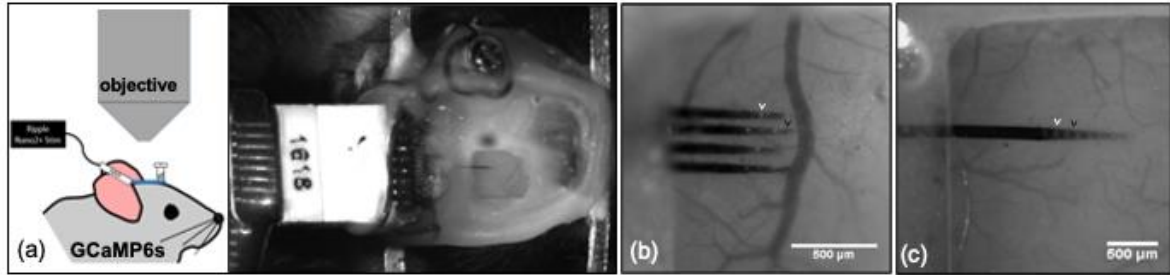


Figure 10. *In vivo* experimental setup. (a, left) Cartoon of a GCaMP 6s mouse implanted with a multielectrode array at a 30°angle, the cranial window is sealed with a cover glass allowing for imaging of cortical responses. (a, right) Optical micrograph of the cranial window. The electrode is affixed to a rectangular metal bar which was cemented with a contralaterally implanted stainless-steel reference screw. (b,c) Zoomed-in view of the cranial window showing a four-shank and a one-shank electrode array respectively. White arrows point to IrOx sites and black arrows point to PC sites. Scale bars represent 500 μm .

The GCaMP fluorescence increased with increasing electrical stimulation intensity (Figure 11a). Additionally, stimulating via sites of different coating materials within the same electrode array resulted in heterogeneous GCaMP responses (Figure 11b,c). We quantified the intensity and radius of GCaMP responses using 2D exponential curve (Figure 11c inset). The height and width of the exponential curve represents the intensity and radius of the GCaMP response.

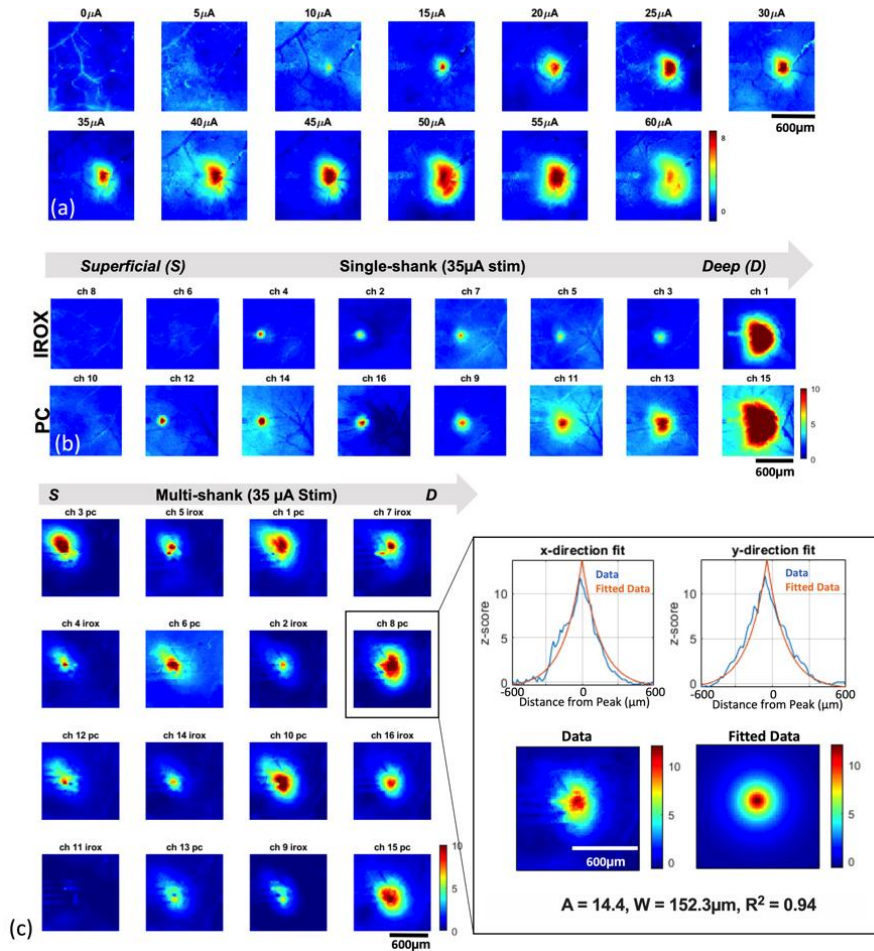


Figure 11. Mesoscale imaging of GCaMP response to electrical stimulation. (a) Snapshots of maximum GCaMP response to increasing electrical stimulation from a representative PC coated electrode site. The stimulation waveform was a biphasic, charge-balanced, cathodic leading pulse (cathodic pulse width: 100µs, interphase interval:100µs, anodic phase: 200 µs, applied at 50 Hz (b) Snapshots of maximum GCaMP responses to a 35µA stimulation on electrode sites from a single-shank array. The top row shows responses from IrOx sites. The bottom row shows responses from their following (distal from the connector) PC sites, 50µm away. (c) Snapshots of the maximum GCaMP responses to a 35 µA stimulation on electrode sites from a four-shank array whose alternating sites are coated with PC or IROX. Inset shows a representative 2-D exponential fitting from an individual trial from Ch8. The fit was performed on the image data, profiles of the fit are shown on the top row shows along the x and y-direction (blue is the experimental data and orange is the model fit). The bottom row shows the 2D experimental image data (left) and model fit in 2D image (right). The result of the fitting is represented in the exponential decay equation with the peak GCaMP response of 14.4 (z-score) and radius of activation of 152.3µm. Gray arrows denote electrode positions from superficial to deep. Scale bars represent 600 µm.

Quantification of the mesoscale imaging confirms the observation that increases in stimulation intensity resulted in increasing neuronal activation as represented by the GCaMP response intensity and radius (Figure 12a,e). The increase in GCaMP responses amplitude suggests an increase in the density of neurons in the vicinity of the electrode, meanwhile the increase in GCaMP radius suggests an increase in activation volume. We then examined the potential differences in material. Due to the heterogeneous expression of GCaMP and neuronal distribution across the cortical depth, we normalized GCaMP intensity and radius elicited by PC sites to their IrOx counterpart. PC sites stimulated significantly more intense GCaMP activity across the amplitudes that were applied ($p < 0.005$). Additionally, this observation was consistent across the two electrode geometries (Figure 12c,d). Furthermore, PC sites elicited a significantly higher GCaMP radius, regardless of probe geometry (Figure 12f-h).

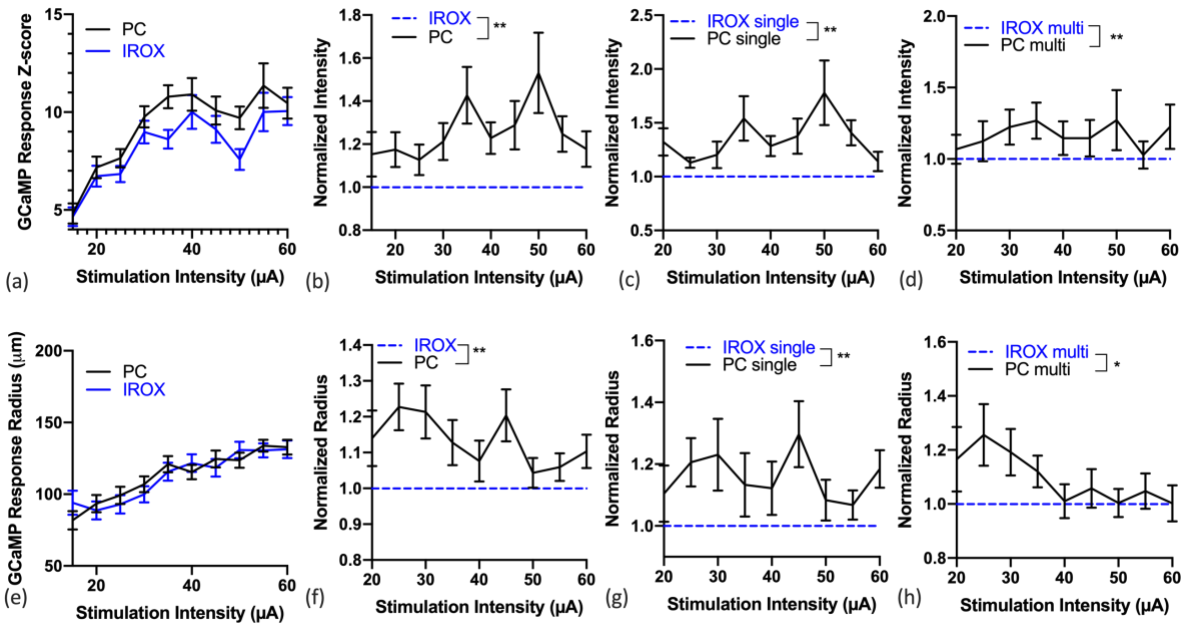


Figure 12. Quantification of GCaMP response to electrical stimulation. (a) Mean GCaMP intensity as a function of stimulation amplitude (pooling data from single and multi-shank arrays). GCaMP intensity increases with increasing stimulation current. PC sites elicit significantly higher GCaMP response than IrOx sites. **** $p < 0.005$, two-way ANOVA. $n = 44-60$ electrode sites that elicited threshold crossing GCaMP intensity at different stimulation amplitudes. $N = 10$ mice. Error bars represent the standard error of the mean. (b)** Mean normalized GCaMP intensity as a function of stimulation amplitude regardless of electrode geometry. **** $p < 0.005$, Wilcoxon signed-rank test. (c)** Mean normalized GCaMP intensity as a function of stimulation amplitude for both materials for single-shank electrode arrays. $n = 20 - 30$ electrode sites that elicited threshold crossing GCaMP intensity at different stimulation amplitudes. $N = 5$ mice. **** $p < 0.005$, Wilcoxon signed-rank test. (d)** Mean normalized GCaMP intensity as a function of stimulation amplitude for both materials for multi-shank electrode arrays. $n = 14 - 26$ electrode sites that elicited threshold crossing GCaMP intensities at different stimulation amplitudes. $N = 5$ mice. **** $p < 0.005$, Wilcoxon signed-rank test. (e)** The mean GCaMP radius increases as a function of stimulation amplitude for both material types. $n = 44-60$ electrode sites that elicited threshold crossing GCaMP response at different stimulation amplitude. $N = 10$ mice. (f). Normalized radius from (e). PC sites elicited significantly broader GCaMP responses compared to IrOx sites. (g). The normalized radius for single and (h) multi-shank electrode arrays. *** $p < 0.05$, Wilcoxon signed-rank test.**

2.4.3 Effect of the number of electrode shanks on GCaMP intensity and radius

The number of probe shanks did not significantly alter GCaMP intensity with increasing stimulation amplitude (Figure 13a). This observation is consistent across material types (Figure 13b,c). In contrast, stimulating from multi-shank arrays resulted in significantly broader GCaMP activity than stimulating from single-shank arrays(Figure 13d). This observation is consistent across both material types (Figure 13e,f).

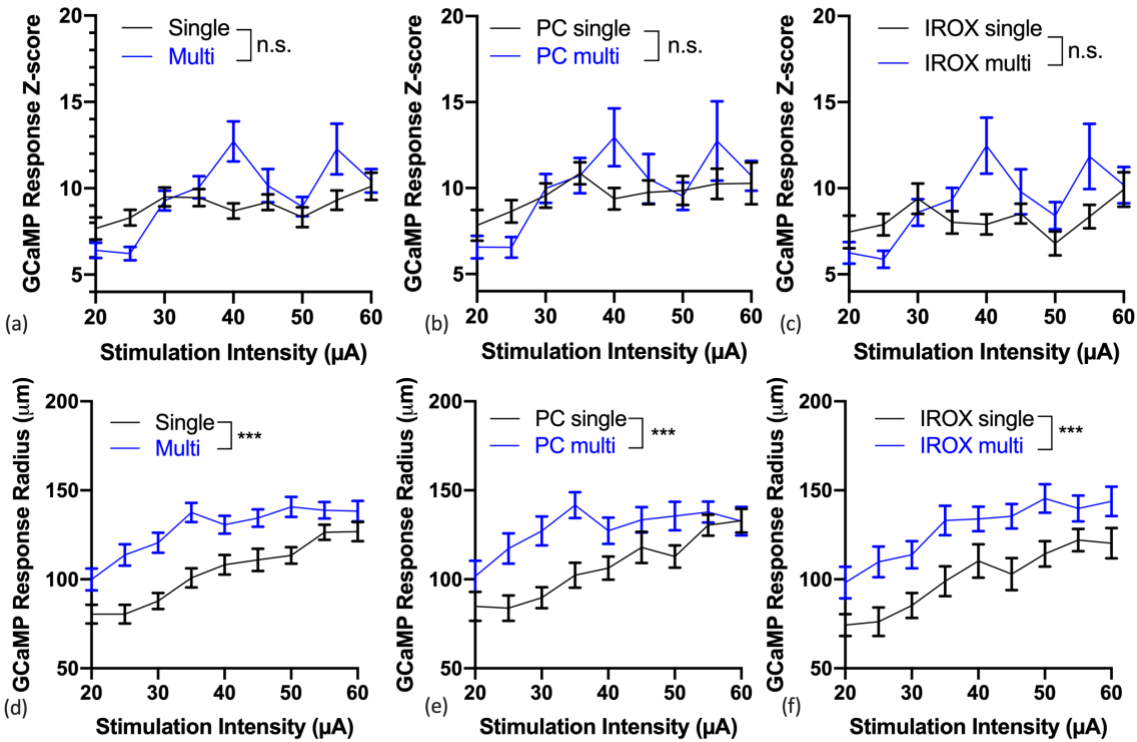


Figure 13. Effect of electrode shank number on GCaMP intensity and radius. (a) Mean GCaMP intensity as a function of stimulation amplitude for single and multi-shank electrode arrays. Pooling data from both materials. $n = 40-60$ electrode sites that elicited threshold-crossing GCaMP events in 5 mice, for each geometry type. (b) Mean GCaMP intensity as a function of stimulation amplitude from PC sites in single vs. multi-shank arrays. $n = 19-30$ electrode sites that elicited threshold crossing GCaMP events in 5 mice, for each geometry type. (c) Mean GCaMP intensity as a function of stimulation amplitude from IrOx sites in single vs. multi-shank arrays. $n = 21-30$ electrode sites that elicited threshold crossing GCaMP events in 5 mice, for each geometry type. (d) Mean GCaMP radius as a function of stimulation amplitude, pooling data from both materials. Multi-shank arrays stimulate a higher radius of activation compared to single-shank arrays. $*** p = 0.0005$, two-way ANOVA, $n = 40-60$ electrode sites that elicited threshold crossing GCaMP events in 5 mice, for each geometry type. (e) Mean radius of activation as a function of stimulation intensity for single vs. multi-shank arrays elicited by PC sites. $*** p = 0.0001$, two-way ANOVA. $n = 19-29$ electrode sites that elicited threshold-crossing GCaMP events in 5 mice, for each geometry type. (f) Mean radius of activation as a function of stimulation intensity for single vs. multi-shank arrays elicited by IrOx sites. $*** p = 0.0005$, 20–30 electrode sites that elicited threshold crossing GCaMP events in 5 mice, for each geometry type.

2.4.4 Material differences in constant voltage versus constant current stimulation

We then examined whether electrode material plays a role in neuronal activation using either constant-voltage or constant-current stimulations. First, we delivered charge-balanced bi-phasic voltage-controlled stimulation at 3V in the cathodic phase, which generated a maximum cathodic current of approximately 28 μA and 43 μA for IrOx and PC electrodes, respectively (Figure 9i). The elicited calcium response was measured by TPM (Figure 14a and b). Electrical stimulation via PC sites with peak voltage of 3V activated a significantly larger number of neuronal soma ($p < 0.01$) as well as a significantly higher intensity of neuropil ($p < 0.01$) compared to IrOx (Figure 14c and Figure 14d). Next, we examined the delivered charge-balanced bi-phasic current-controlled stimulation at 30 μA in the cathodic phase and imaged the GCaMP response (Figure 14e and f). Stimulation via PC sites activated a significantly higher number of somas ($p < 0.05$) compared to IrOx, while no significant difference in neuropil recruitment was observed (Figure 14g, Figure 14h)

To compare the efficiency of electrical stimulation for IrOx and PC, we calculated the electrical energy for current-controlled stimulation. PC electrode sites delivered significantly less energy compared to IrOx sites, (15 ± 0.4 nJ, $n = 41$ PC sites. 17.5 ± 0.5 nJ, $n = 38$ IrOx sites, $p = 0.0005$, unpaired two-tailed *t-test*). If we define stimulation efficiency as the number of neurons activated per Joule, the stimulation efficiency of PC is 80 ± 47 cells/nJ, which is significantly higher than IrOx 60 ± 31 cells/nJ ($p < 0.05$).

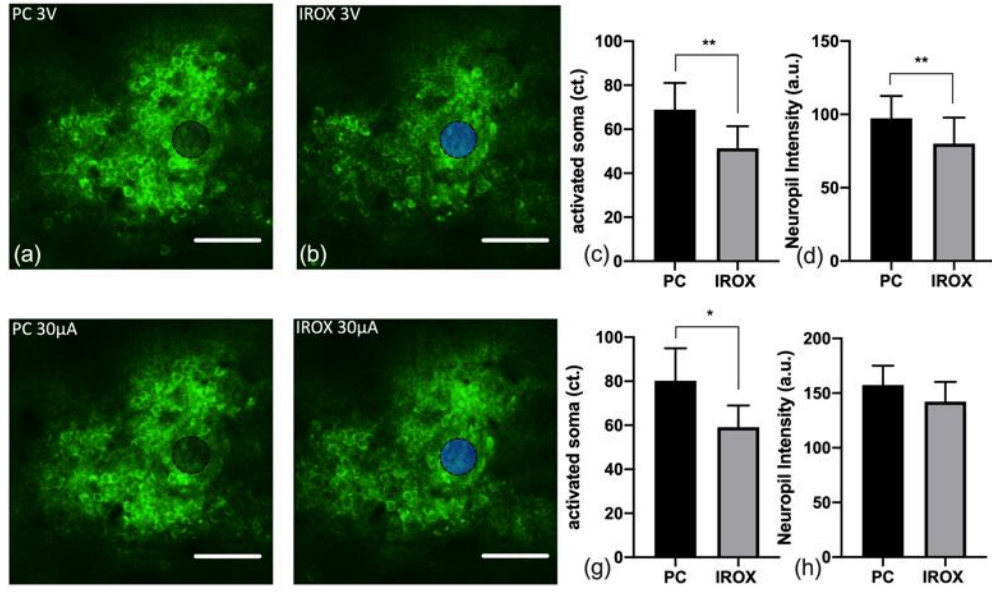


Figure 14. Two-photon microscopy investigation of voltage and current controlled electrical stimulation. (a,b) Neural elements evoked by 3V biphasic voltage-controlled stimuli from a PC and an IrOx, respectively. Electrode locations are denoted by black and blue disks, respectively. Scale bars represent 50µm. (c) Quantification of electrically activated neuronal soma as a result of a 3V stimulus. $p < 0.01$. (d) Quantification of neuropil intensity within the image after subtracting somas. $**p < 0.01$. (e,f) Neural elements activated by 30µA biphasic current-controlled stimuli from a PC and an IrOx. Electrode locations are denoted by black and blue disks, respectively. (g) Quantification of electrically activated somas from PC and IrOx sites. $*p < 0.05$. (h) Quantification of neuropil intensity after subtracting somas. $n = 10$ sites for each material tested in $N = 3$ mice.**

2.4.5 Pulse width modulation for microstimulation selectivity

Using two-photon microscopy, we examined the effect of modulating pulse width and current amplitude while maintaining a constant charge between 1nC/ph—4 nC/ph, on neuronal recruitment. Figure 15a shows representative TPM images of neural elements stimulated by 66 μ s – 500 μ s long cathodic pulses at 4nC/ph using electrodes coated with PC and IrOx. PC coated electrodes activated a significantly higher number of neuronal soma than IrOx coated electrodes across all pulse widths. Additionally, there were no significant differences in the number of activated neuron soma among pulse widths for either material (Figure 15b). Figure 15c shows the quantification of electrically activated neuropil as a function of pulse widths for PC and IrOx coatings. There were no significant differences in neuropil activation between material types and among pulse widths. Figure 16 a - f are threshold maps of the same brain region stimulated by the same electrode (white asterisk) for different pulse widths. The color for each pixel represents the lowest current for it to be significantly activated by the electrical stimulation. We observed that stimulating with shorter pulses results in more spatially distinct neuronal recruitment. As the pulse width increases, the recruited neuronal elements become less distinguishable. We quantified this trend by binning each image from the center of the electrode to the edges of the ROI and calculating the average threshold current for each bin(g). To compare the differences in selectivity among these pulse widths, we performed linear regression for all recruitment curves within 100 μ m from the electrode center where the relationship between threshold current and distance was the most linear, and all regressions exhibited significant non-zero slopes (data not shown). Moreover, by performing linear regression between selectivity and pulse width we observed that the increase in pulse width resulted in significantly decreased spatial selectivity (Figure 16h). The material type did not have an effect on pulse width modulated neuronal selectivity.

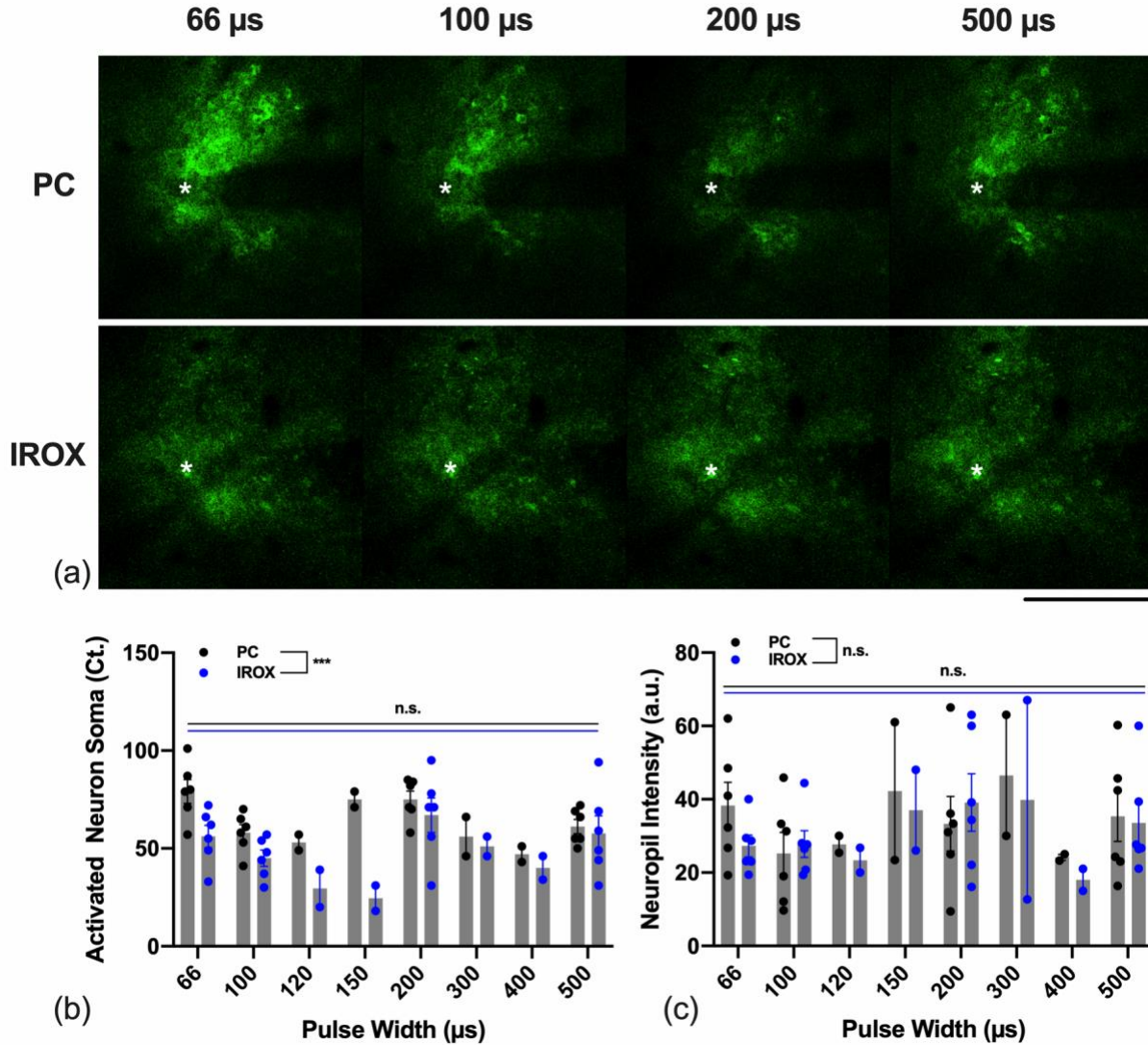


Figure 15. Effect of pulse width modulation on neural activation. (a) Representative TPM images showing electrically stimulation GCaMP expressed neural elements for 66 μs – 500 μs pulse widths at 4nC/ph for PC and IrOx coatings. (b) Quantification of electrically activated neuron soma for pulse widths between 66 μs to 500 μs for PC and IrOx coatings. PC activates significantly higher neuronal soma than IrOx across all pulse widths. There is no significant difference among the activated neuron soma among pulse widths for either material. Black and blue dots represent $n = 2 - 6$ biological replicates for each material for each pulse width pooled from $N = 3$ mice. Two-way ANOVA. *** $p = 0.0002$. (c) Quantification of electrically activated neuropil as a function of pulse widths for PC and IrOx coatings. There are no significant differences in

neuropil activation between material types and pulse widths. Two-way ANOVA.

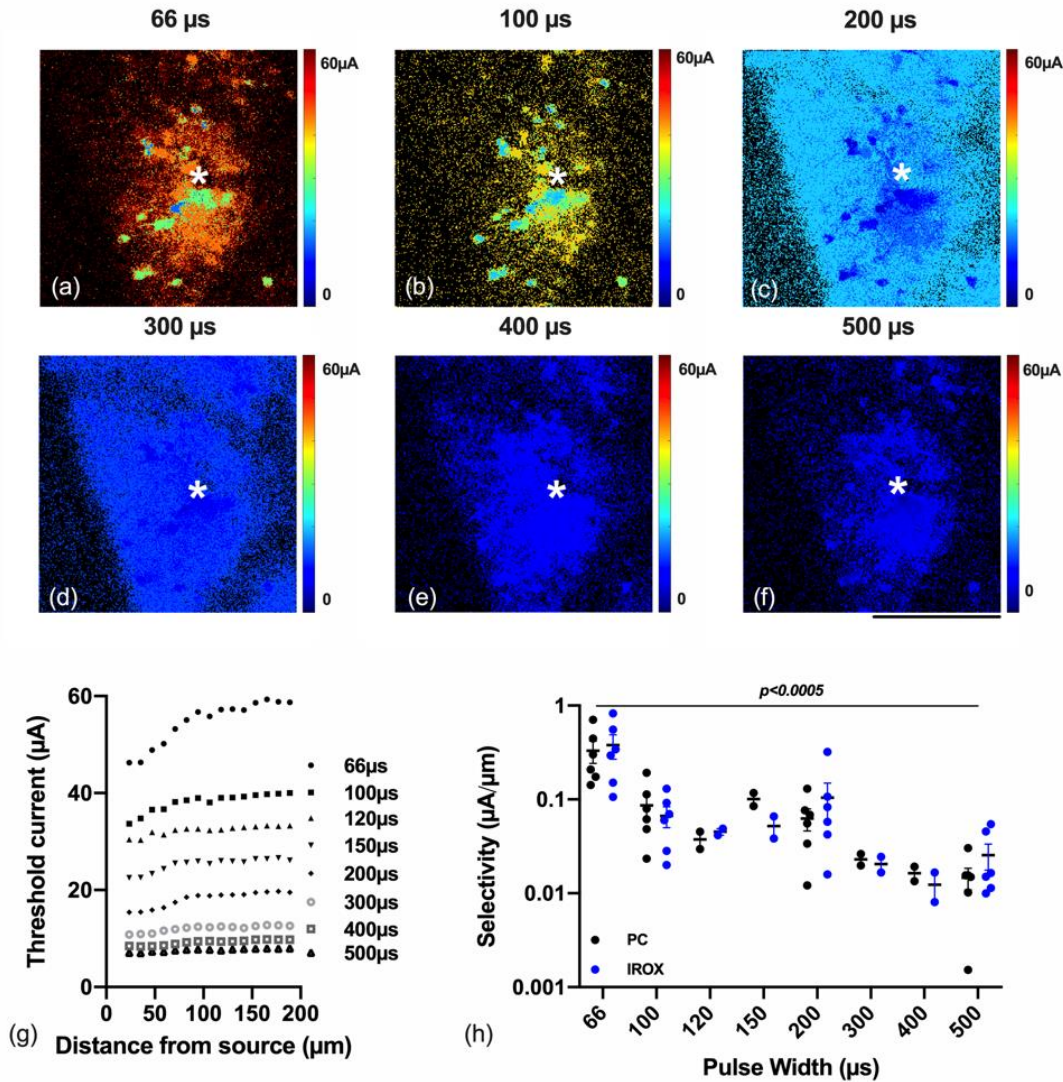


Figure 16. Effect of pulse width modulation on neuronal selectivity. (a-f) Representative threshold maps for charge injections between 1nC/ph to 4nC/ph by varying pulse width and current amplitude. Electrode positions are denoted with asterisks. Color bars represent threshold currents for each pixel. (g)

Representative plot of threshold current as a function of distance away from the center of the electrode.

Different marker styles represent different pulse widths. (h) Selectivity significantly decreases with increasing pulse widths. Black dots represent selectivity values for each pulse width from $n = 4-12$ electrode sites $N = 3$ mice. P-value represents the significance of the slope of the linear regression for selectivity versus pulse width. Scale bars represent 100 μm .

2.4.6 Explanted arrays

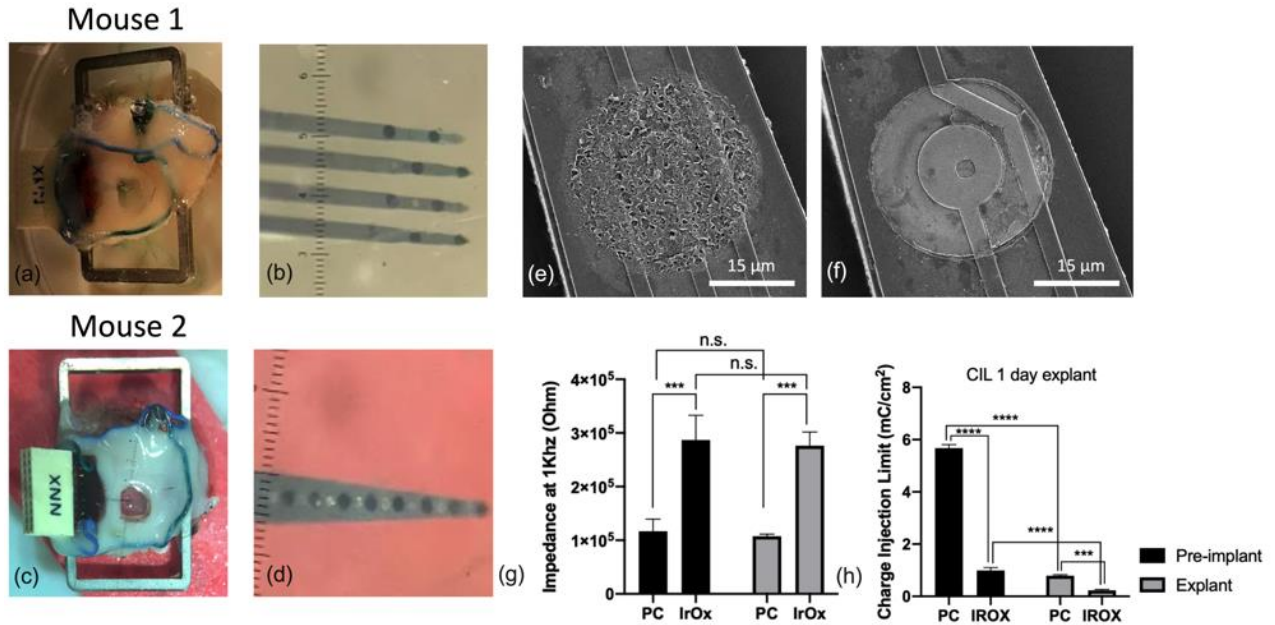


Figure 17. Explant examination. (a) Explanted skull showing headframe, cranial window, a 4x4 electrode array and reference screw. (b) Zoomed in view of the 4x4 electrode array. (c) Explanted skull from a different mouse showing the same components of mouse 1 but a linear array. (e) SEM of a representative array showing an electrode site coated with PEDOT/CNT. (f) SEM of a representative array showing an electrode site with IrOx thinfilm. (g) Impedance at 1kHz of explanted arrays coated with PC and IrOX pre-implant and explanted. There was no significant difference in impedance between pre and post stimulation measurements. (h). Charge injection limit for PC and IrOx pre and post implantation. Measurements were performed in PBS with a three electrode setup against Ag/AgCl reference electrode. N = 16 electrode sites for IrOx and PC, respectively. Two-way ANOVA, Tukey's post hoc correction. *** $p < 0.001$, **** $p < 0.0001$.

2.5 Discussion

Recent advances in the use of microstimulation for restoring movement, sensation, vision, and hearing motivate the need for a deeper understanding of how electrode materials, stimulation modality, and stimulation parameters affect the efficiency, selectivity, safety, and stability of stimulation. *In vivo* imaging in awake GCaMP6s mice affords us the opportunity for direct visualization of the stimulated outcome in real-time. Particularly, this study examined the efficiency and selectivity of PC coated electrodes for electrical microstimulation using *in vivo* imaging in comparison to the commonly used microstimulation material IrOx. We modified the individual microelectrode sites of NeuroNexus probes with IrOx and PC coatings in an alternating pattern to directly compare the two electrode materials. First, we delivered electrical stimuli ranging from 0.5nC/ph to 6nC/ph and used a model to obtain a measure of the GCaMP response amplitude and radius from meso scale fluorescence microscopy data. PC coated electrodes evoked significantly stronger GCaMP response amplitudes and larger radii compared to IrOx. Next, using two-photon microscopy, we examined whether electrode material plays a role in the magnitude of neuronal activation and energy delivery in constant-voltage and constant-current stimulations. PC coated electrodes exhibited superior energy efficiency for neural stimulation in terms of activating more intense and broader GCaMP for the same delivered charge compared to IrOx coated electrodes. Meanwhile, also using TPM, we explored the effect of pulse width modulation on cortical stimulation selectivity using IrOx and PC. Stimulation with shorter cathodic leading pulse widths resulted in more selective neural activation compared to longer pulses for both materials.

2.5.1 Electrochemical features of PC and IrOx

Characterization of the modified electrodes reveals unique electrochemical signatures of the two electrode materials. PC coated electrodes had significantly lower impedance, higher charge injection limit and similar cathodic charge storage capacity compared to IrOx coated electrodes. Consistent with observations in the literature, the unique electrochemical properties of PC are attributed to the nanofibrous structure of the coating, dramatically increasing the electrochemical surface area for charge transfer, [23, 86] compared to the IrOx surfaces, which are relatively smoother. Other methods for forming IrOx such as sputtered IrOx films can result in a nano-surface topography which increases electrochemical surface areas and improves the electrochemical behavior.[15, 73] In addition, to be consistent with most of the stimulation paradigms used in animal and human studies, we did not perform a bias voltage on IrOx coated electrodes during stimulation, which has been shown to further reduce impedance and improve the charge injection limit.[16] *In vivo*, both electrode materials retained their electrochemical features as seen *in vitro* (Figure 9f,g). The overall elevated impedance is due to the higher impedance of tissue compared to PBS. *In vivo* current pulsing at 30 μ A to both materials resulted in a voltage transient with lower overall amplitude for PC electrodes (Figure 9h). Lower *in vivo* voltage transient and lower E_{mc} suggest a higher charge injection capacity before safety limit is reached for the PC electrode. Furthermore, less energy is consumed from the PC electrode than IrOx at the same current injection, which is desired for extending battery life in chronic constant-current stimulators with implanted batteries. Similarly, due to the lower electrical impedance offered by PC surfaces,

pulsing both materials with a 3V biphasic stimulus results in a higher injected current, offering potential higher power efficiency compared to IrOx surfaces .

2.5.2 Effect of electrode material on the intensity and the spread of the GCaMP response

Fluorescence microscopy in awake head-fixed mice provides direct visualization of cortical responses to electrical stimulation. Lower stimulation amplitudes (0.5- 1.5 nC/ph) showed non-statistically significant GCaMP responses that were indistinguishable from ongoing GCaMP fluorescence fluctuations in awake mice. Increasing charge density between 2 nC/ph to 4 nC/ph resulted in increasing GCaMP responses (Figure 12a). This is expected because increasing charge injection increases the extracellular voltage which increases the likelihood of initiation of the action potential of nearby neural elements [225]. Additionally, the rate of increase of GCaMP intensity stimulated by the PC electrode is higher than that stimulated by the IrOx electrode. However, GCaMP responses did not continue to increase for charge densities between 4.5nC/ph to 6 nC/ph (Figure 12a), for both electrode materials. Since there was no significant increase in electrical impedance for both materials before and after stimulation, we exclude the unlikely contribution of changes in electrode property during stimulation (Figure 17). This phenomenon may be attributed to acute neuronal injury due to electrode implantation. The insertion of the electrode into the cortex triggers acute inflammation which deprives the extracellular environments of nutrients such as oxygen and glucose, which are essential for action potential initiation[226], as such the neuronal elements are not able to meet the high metabolic demand of high-intensity stimulation. In addition, the severed axonal connections and membranes of somas likely contributing to the plateau in recruiting neural elements.

Due to the heterogeneity of GCaMP6s expression and neuronal density relative to cortical depth (Figure 11b,c), the comparison of electrode efficiency was made by normalizing the PC site data to their neighboring IrOx counterparts, resulting in up to 8 pairs of comparisons per mouse. Statistical analyses revealed that PC sites elicited significantly higher and broader GCaMP responses than IrOx sites for both electrode shank densities(Figure 12). Due to the nanofibrous nature of the PC coating, micro-scale surface topography creates a significantly rougher surface compared to IrOx coatings. The increase in surface roughness results in (1) increased non-uniform voltage distribution thereby increasing the activating function of nearby neural elements[227], and (2) the three-dimensional morphology of the PC coating reducing the distance between the current source and neural elements. The estimation of extracellular voltage field distribution based on PC and IrOx coatings is described in detail in Chapter 3.

2.5.3 Effect of electrode shank number on GCAMP response

We examined the effect of probe shank number on cortical responses to electrical stimulation. There were no significant differences between the electrode shank number on GCaMP responses (Figure 13a) for either electrode materials (Figure 13b,c). While the radius of activation increased with increasing stimulation intensity (Figure 13d), the overall radius of activation elicited by multi-shank arrays was higher than that elicited by single-shank arrays. (Figure 13e,f). This could be explained by the larger insertion footprint from multi-shank arrays relative to single-shank arrays, resulting in larger areas of the brain with damaged neural elements. Our group has previously investigated calcium activity and morphology of neurons before, during, and one month after the insertion of an electrode array, and found that the implantation leads to sustained, abnormal high calcium levels in neurons within 150 μm of the implant. These neurons were

morphologically distorted, and some cellular membranes were mechanoporated which could increase the likelihood of calcium influx. Neurites exhibited signs of axonal injury in response to the device implantation, forming swollen, hypertrophic spherical bodies, or “blebs”.[118] In addition, axotomy as a result of mild traumatic brain injury has been reported to increase neuronal network excitability within 48 hours after damage,[228] which could explain the more excitable brain environment around multi-shank probes compared to single-shank probes acutely. While the healthy calcium activity recovers over the first month in this study, how the initial damage, especially by electrodes with larger footprints such as the Utah 10x10 multi-electrode arrays, affects the long-term neuronal function for electrical stimulation, remains to be investigated.

2.5.4 Higher stimulation efficiency from PC than IrOx in both voltage and current controlled stimulation modalities

There are two types of stimulation modalities for cortical microstimulation: constant-voltage stimulations and constant-current stimulations. In constant voltage stimulations, voltage is applied between the microelectrode and the ground resulting in an injected charge into the tissue. However, due to foreign body response, the conductivity of the local environment of the electrode can vary throughout the implant period. This will result in unpredictable charge injection, making it difficult to maintain stimulation consistency. On the other hand, constant-current stimulations allow us to control the total injected charge, making chronic microstimulation more reliable with an increased risk of voltage transient exceeding the water window. For TPM studies, the GCaMP response within the field of view consists of excitatory neuron somas at the imaging plane, and neuropil, which consists of axons, dendrites, and out-of-plane somas. We observed significant advantage in both neuronal soma and neuropil recruitment for PC coated electrodes compared to

IrOx electrodes for constant voltage stimulation. This observation agrees with our understanding that a lower impedance electrode results in higher injected current amplitude (Figure 9i)[213]. On the other hand, we have observed a significant difference in neuron soma recruitment but no significant difference in neuropil activation in the constant current mode from the two materials. The difference in soma activation likely stems from the increased activating function of neurons as a result of an increased and non-uniform voltage distribution nearby PC sites[227, 229]. In addition, the three-dimensional nano-fibrous network of the PC coating enables a more intimate connection with the neural tissue compared to the relatively smoother IrOx surface. Closer contact between the electrode and the excitable neural tissue, reduces the likelihood of current shunting by the extracellular fluid, resulting in more efficacious neural stimulation. The lack of statistical significance in the neuropil activation could be explained by the small difference in extracellular voltage elicited by both materials at 30 μ A(Figure 21). In addition, with our two-photon imaging set up, we can only observe neural elements within one plane for each stimulation session, where the majority of fluorescence are contributed by the highly GCaMP expressing neuronal soma, which could influence the detection of statistical differences in neuropil intensity upon stimulation from both electrode materials. Regardless, for current-controlled stimulation, PC electrodes delivered significantly less energy compared to IrOx, making them a more energy-efficient material for battery life preservation in chronically implanted stimulators.

2.5.5 Pulse width modulation on stimulation selectivity in the cortex

In the realm of therapeutic and functional stimulations of the CNS, pulse width modulation has been associated with various functional outcomes in therapeutic efforts. In auditory

prostheses, modulating pulse widths affected auditory percepts other than loudness, particularly, a longer pulse duration (266 μ s) resulted in a different perceived pitch than a short pulse duration (50 to 100 μ s). [230] In retinal prostheses, focal cellular responses could be achieved with relative short pulse durations ($\leq 120\mu$ s), which improves the spatial resolution and more ideal shape perception.[113] In studies in non-human primates for sensory prostheses, the detection threshold was lower for shorter pulse widths compared to longer pulse widths, however, this difference disappears at higher stimulation frequencies.[231] In human cortical microstimulation, pulse widths between 50 – 400 μ s have been surveyed in the motor and the sensory cortices. For somatosensory restoration studies in humans, 200 μ s and 400 μ s pulse widths elicited two different types of sensations, electrical buzz, and tingling, respectively. [232] We investigated the effect of pulse width modulation on neuronal activation selectivity using two-photon microscopy. We maintained a constant charge between 1nC/ph to 4nC/ph and varied the pulse width and current amplitude. We quantified the activation profile of layer II/III neurons. The threshold current maps of neuronal responses at different pulse widths reveal more spatially distinct activations with shorter pulse widths compared to longer pulse widths (Figure 15). A potential explanation for this observation is that (1) for the same charge density (nC/ph) there is a higher temporal current density (μ A/ μ s) delivered with shorter pulses compared to longer pulses, and (2) with increasing charge densities, there was a higher increase in current amplitude with shorter pulses compared to longer pulses. Both factors can increase the likelihood of activating fibers with varying diameters and fibers that are farther away from the current source, resulting in a more spatially distinct activation with shorter pulses. Our observations are consistent with reports made in the *ex-vivo* calcium imaging study investigating stimulation strategies for selective activation of retinal ganglion cells.[113] In their study, using charge-balanced cathodic leading pulses, stimulating with

pulse widths beyond 500 μs yields spatially indistinguishable activation of neural elements at increasing current amplitudes.

2.6 Limitations

While our study has the advantage of stimulating and imaging the cortex of awake mice which mimics the conditions of human studies, the awake brain had large ongoing fluctuations. These large fluctuations made it difficult to capture significant mesoscale GCaMP responses at low stimulation amplitudes (5-15 μA). However, we were able to accurately depict GCaMP activation patterns at amplitudes higher than 15 μA and drew comparisons between materials. In addition, simulating human studies, our stimulation paradigms did not involve the use of bias voltages which has been demonstrated beneficial for increasing the conductivity and charge injection limit of IrOx electrodes[16]. Moreover, while implantation at a 30-degree- angle allows imaging of electrically stimulated neural response, this set-up is still limited to superficial regions of the cortex. The depth of imaging is further obstructed by the radio-opaque Michigan arrays. The use of three-photon microscopy [233] and the use of transparent arrays [234] can increase image depth and image quality.

2.7 Conclusion

With the increasing development in efficient materials for electrical stimulation, it is crucial to understand their *in vivo* performance. We investigated the *in vivo* stimulation efficiency of two high charge injection materials. Using advanced imaging techniques, we observed distinct differences in neuronal responses stimulated by PC and IrOx coatings. Specifically, we observed significantly higher and broader neural activation by PC coated electrodes compared to IrOx coated electrodes. This observation was highly likely due to (1) the nano-fibrous surface topography of PC electrodes, creating a more non-uniform electric field compared to IrOx electrodes thereby increasing the activating function of nearby neural elements (described in Chapter 3), and (2) the fractal nature of the PC coating creates a better integration of neural tissue than the smoother IrOx coating. The improved electrode-tissue integration may reduce additional extracellular fluid buildup, which could shunt the injected current, requiring higher charge injection. In addition, we observed that microelectrode arrays with multiple shanks recruit a wider region of the cortex compared to single shank arrays. This may be associated with the larger implant footprint which severs additional axon, increasing network excitability evident in mild traumatic brain injury literatures. Moreover, *in vivo* imaging of GCaMP response upon electrical stimulation were performed 24h post electrode implantation, allowing us to study the *in vivo* electrode performance without the interference of glial scarring. Furthermore, we investigated the effect of stimulation modality on neural activation. With voltage-controlled stimulation, PC coated electrodes activate significantly more neural tissue than IrOx due to the lower impedance and the consequent higher injected current. With current-controlled stimulation, we observed higher soma recruitment from PC sites than IrOx sites. Lastly, for both materials, we observed more spatially distinct neuronal activation with shorter pulse widths. The findings of this work contribute to our

understanding of cortical microstimulation using novel materials; by using *in vivo* imaging in awake mice, we mimic conditions in human studies while directly visualized the region of activated neural tissue. Our results show that PC coated electrodes provide essential improvements in electrical stimulation applications in terms of increased energy efficiency compared to IrOx coated electrodes. Further work to assess the chronic *in vivo* stimulation performance of the PC electrode and other novel stimulation materials using this imaging setup is warranted.

3.0 Finite Element Analysis of Electric Fields of PEDOT/CNT and Iridium Oxide

Electrodes

3.1 Chapter Overview

Computational modeling is an effective tool for engineers in designing, evaluating and understanding complex systems. Simulation techniques such as finite element modeling enable the exploration of large parameter spaces especially when resources are limited. In this chapter, we explore a potential mechanism behind the observation made in chapter 2 regarding the increased stimulation efficiency provided by the PC coating. We hypothesize that one of the mechanisms for the broader and more intense GCaMP response is due to the nano-fibrous surface topography of the PC coating, which increases the non-uniformity in electric field, increasing the likelihood of neuronal activation. We explanted and cleaned electrodes coated with PC and IrOx from acute stimulation experiments. We simulated the electric field from stimulating these electrodes using COMSOL Multiphysics based on the surface features derived from SEM. Our results show that PC has average change of field strength $1.14e4V/m$ per microamp compared to $0.97e4V/m$ per microamp imparted by IrOx, suggesting that the PC material results in a larger change in electric field strength per incremental change in applied current, leading to more power efficient electrical stimulation.

3.2 Introduction

Computational modeling is an efficient tool for neural engineers for the design, evaluation, understanding of electrodes for neural interfaces. Simulation techniques such as finite element modeling (FEM) enable the exploration of large parameter spaces, particularly when experimental resources are limited. In neural engineering, FEM have been used to model the thermal [235], mechanical[236, 237], and electrical[238, 239] [240, 241] properties of electrodes in biological tissues.

The electrical field distributions for macroelectrodes with various shapes have been explored by several groups. To improve the efficiency of deep brain stimulation electrodes, Wei and Grill proposed to increase the electrode perimeter without changing the electrode area. They rationalize this design by the fact that increasing the perimeter without changing the area increases the non-uniformity of current density on the electrode surface, generating larger activation functions for surrounding neurons, thereby increasing stimulation efficiency. Model results demonstrated that serpentine perimeter resulted in lower threshold currents for axons that were farther away from the electrode surface than circular electrodes[227, 229]. Similarly, Park et al used FEM to optimize the electrode design for maximum energy efficiency [241]. Specifically, they compared the current density distribution of circular, fractal, serpentine, and serpentine with higher perimeter electrodes. As a result, fractal electrode designs produced the highest current density around the microelectrode, followed by the serpentine style electrodes with higher perimeters, followed by circular electrodes. Additionally, all high perimeter to area ratio electrodes showed broader average current density distribution as a function of distance away from the surface of the electrode.

In Chapter 2, we observed that PEDOT/CNT coated microelectrodes elicit broader and more intense neural activity in the form of GCaMP responses than IrOx microelectrodes. We attribute this observation to the nano-fibrous structures that make up the PEDOT/CNT surfaces, compared to IrOx surfaces, which are smoother. Based on prior literature, we hypothesize that a rougher surface will generate a denser and broader voltage field thereby increasing the likelihood of neuronal activation. In this chapter, we created a finite element model in COMSOL to mimic the surface topography of PEDOT/CNT and IrOx. We apply current controlled electrical stimulation through either electrode surface with reference to a skull screw in simulated brain tissue and quantified the resulting electric field.

3.2.1 Materials and Methods

3.2.1.1 Finite Element Model in COMSOL

To study impact of potential differences in the electric field imparted by current delivery through IrOx and PC sites, a finite element model was established in the *AC/DC module* in COMSOL v5.5. The 2D model consists of a working electrode (WE) and a reference electrode (RE) suspended in brain tissue. The conductivity and relative permittivity of IrOx, PC and the brain tissue are reported in Table 1. IrOx sites were represented with a circular disk of $703 \mu\text{m}^2$. To model the roughness imparted by the nano-fibrous topography of PC, these sites were represented with a randomly generated polar curve with random roughness following a Gaussian distribution. This distribution was chosen to mimic the smooth but random variations observed in SEM images from these sites. The roughness of the electrode model was controlled by changing the spatial frequency and spectral exponent. We estimated the spatial frequency and spectral exponent of PC by deriving values obtained from SEM in ImageJ. Specifically, the spatial

resolution was obtained by dividing the number of peaks in the 1D profile by the total distance (μm^{-1}). The spectral exponent was estimated by plotting the power spectrum density of the 1D profile and finding the slope of the linear region that is within the relevant wavenumber range for the smallest feature of the PC composite, i.e. carbon nanotubes[242].

Table 5. material properties used for finite element modeling

	Reference Screw (SS)	PC	Iridium Oxide	Brain
Electrical Conductivity(S/m)	4.032e6	0.026[243]	2.9e6[244]	1.5e-1[245]
Relative Permittivity	1	3.05[246]	3.5e5[244]	2.5e3[245]

3.2.1.2 Electrode Preparation

Electrode modification procedures were described in detail in 2.3.1. After acute electrical stimulation, electrode arrays were carefully explanted. Explanted arrays were first soaked in an enzymatic detergent (Enzol, Advanced Sterilization Products, CA, USA) at room temperature for 1 hour, rinsed with DI water, then soaked in 0.05% trypsin EDTA (Sigma-Aldrich) overnight at 37 °C. Electrode arrays were rinsed with DI water and isoprophol alcohol prior to SEM imaging.

3.2.1.3 Scanning Electron Microscopy

Imaging samples were prepared by carefully breaking off electrode shanks from the omnetics connectors and mounting onto SEM sample nub using copper tapes. The samples were

sputter coated with Au at a thickness of 3.5 nm and imaged using field emission scanning electron microscopy (JOEL JSM 6335F).

3.2.1.4 Quantification of Voltage Field Decay

The voltage profile as a function of distance from the edge of the electrode was fitted to an exponential two-phase decay (equations 3-1 – 3-3) in GraphPad PRISM, using least squares regression, where V_{peak} represents the amplitude of the voltage field when the distance is 0 μm ($X=0$). V_0 represents the amplitude of the voltage field when distance approaches 100 μm ($X = 100$). K_{fast} and K_{slow} represent the two rate constants for the slow and the fast decay phases. f_{fast} is the fraction of the amplitude (from V_{peak} to V_0) accounted for by the faster of the two components.

$$V_{\text{slow}} = (V_{\text{peak}} - V_0) * (1 - f_{\text{fast}}) \quad (3-1)$$

$$V_{\text{fast}} = (V_{\text{peak}} - V_0) * f_{\text{fast}} \quad (3-2)$$

$$Y(X) = V_{\text{slow}} \exp(-K_{\text{slow}}X) + V_{\text{fast}} \exp(-K_{\text{fast}}X) + V_0 \quad (3-3)$$

3.3 Results

3.3.1 Electrode Surface Topography

PEDOT/CNT and IrOx surfaces exhibit distinct topographical features (Figure 18a,b). PEDOT/CNT coating has nano-porous structures which are constituted by PEDOT and carbon nanotubes. Carbon nanotubes can be clearly observed in Figure 18c as bright lines blended within

the PEDOT network (Figure 18c). Contrastingly, the IrOx thin film exhibits a much smoother topography(Figure 18d).

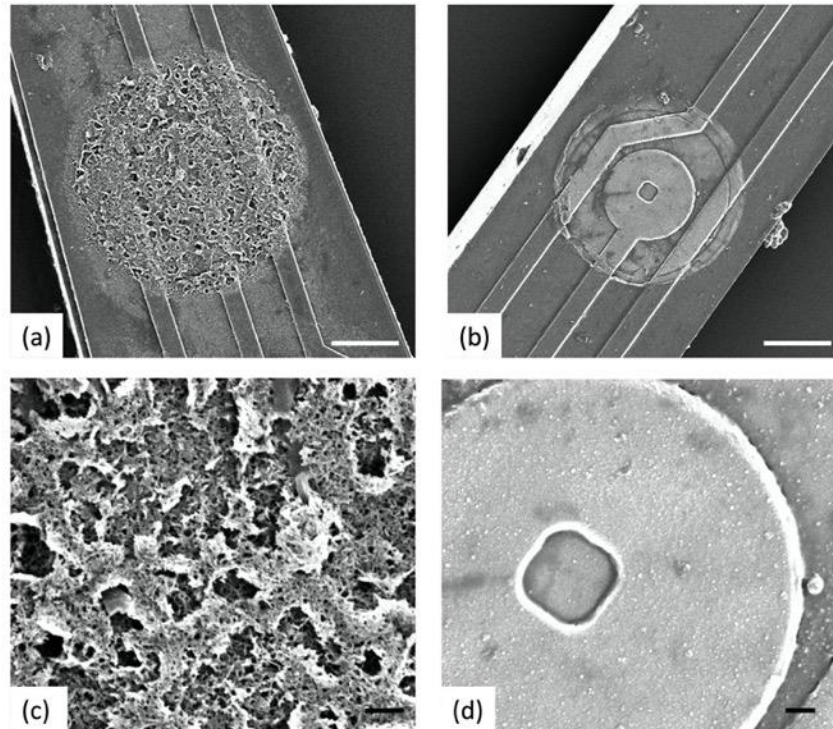


Figure 18. Scanning electron microscopy of acutely explanted Michigan arrays with PEDOT/CNT and IrOx sites. Sites were modified with (a) PEDOT/CNT and (b) IrOx thinfilm. Scale bars represent 10 μm . (c) Magnified view of a PEDOT/CNT coated surface. Scale bar represent 1 μm . (d) Magnified view of a IrOx thinfilm surface. Scale bar represent 1 μm .

We estimated the spatial resolution and spectral exponent of PEDOT/CNT by deriving values obtained from SEM in ImageJ (Figure 19a,b). Specifically, the spatial resolution was obtained by

dividing number of peaks in the 1D profile by the total distance, resulting in spatial resolution (μm^{-1}). The spectral exponent was estimated by plotting the power spectrum density of the 1D profile and finding the slope of the linear region that are within the relevant wavenumber range for the smallest feature of the PEDOT/CNT composite, i.e., carbon nanotubes. From the PEDOT/CNT coating in Figure 19a, we estimated a spectral resolution of $76 \mu\text{m}^{-1}$, and a spectral exponent of 1.5.

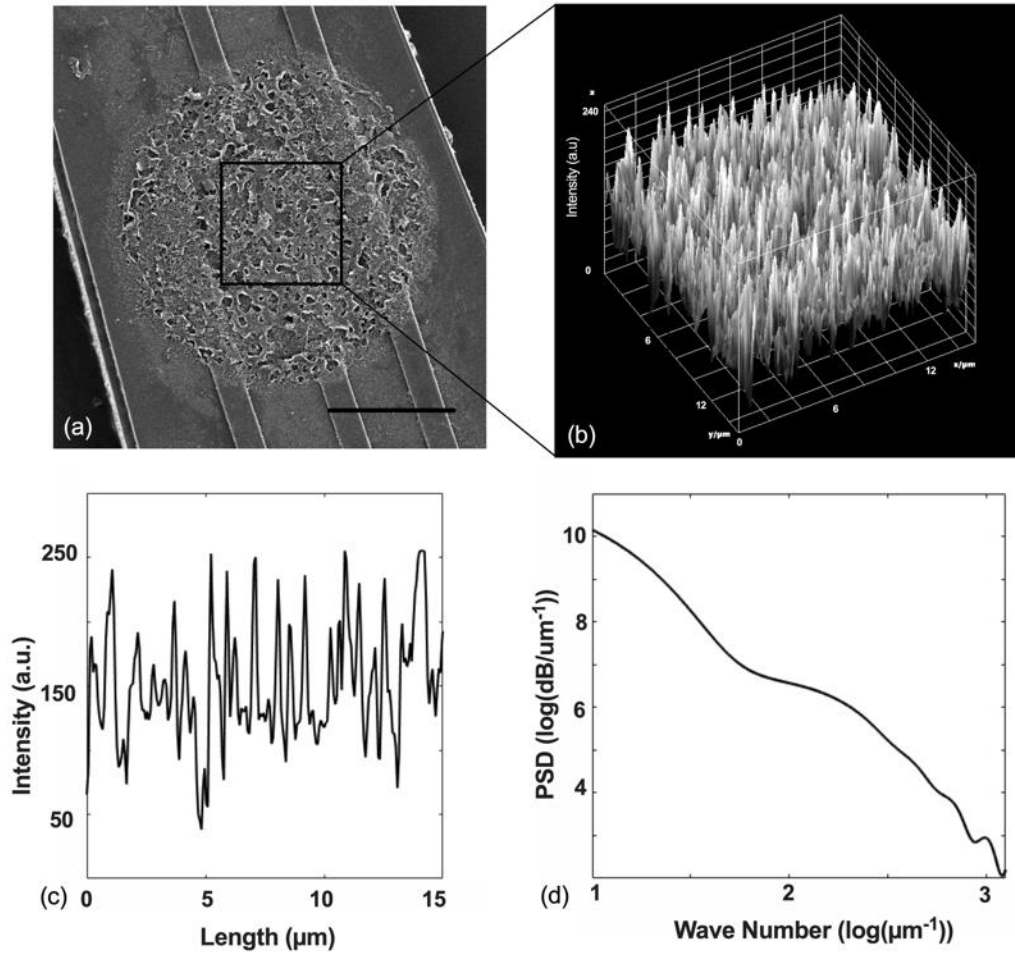


Figure 19. Estimation of fractal features of the PEDOT/CNT surface. (a) SEM of a PEDOT/CNT coating on an iridium substrate. Black box encompass a 3D visualization of surface topography in (b). (b) 3D representation of surface topography based on SEM intensity. (c) 1D profile of the PEDOT/CNT surface topography. (d) 1D profile of the PEDOT/CNT surface topography in the Fourier domain.

3.3.2 2D Finite Element Analysis Using Surface Features Derived from SEM

Using COMSOL Multiphysics, we created a 2D model for PEDOT/CNT and IrOx (Figure 20). Representative images of the electrical field strength for PC and IrOx at 40 μA current amplitude show that the roughened edge of the PC has a more concentrated electric field immediately adjacent to the electrode (Figure 21a) compared to the electric field immediately next to the edge of an IrOx electrode (Figure 21b). Examination of the voltage field profile from the edge of the electrode reveals that there are two phases to the change to voltage field next to the edge of the electrode, a slow and a fast-exponential decay. We created a two-phase exponential decay model and fitted the model with the simulation data. Table 6 displays fitting parameters from the two-phase exponential decay function. PC has a 11.4% larger absolute maximum voltage field than IrOx.

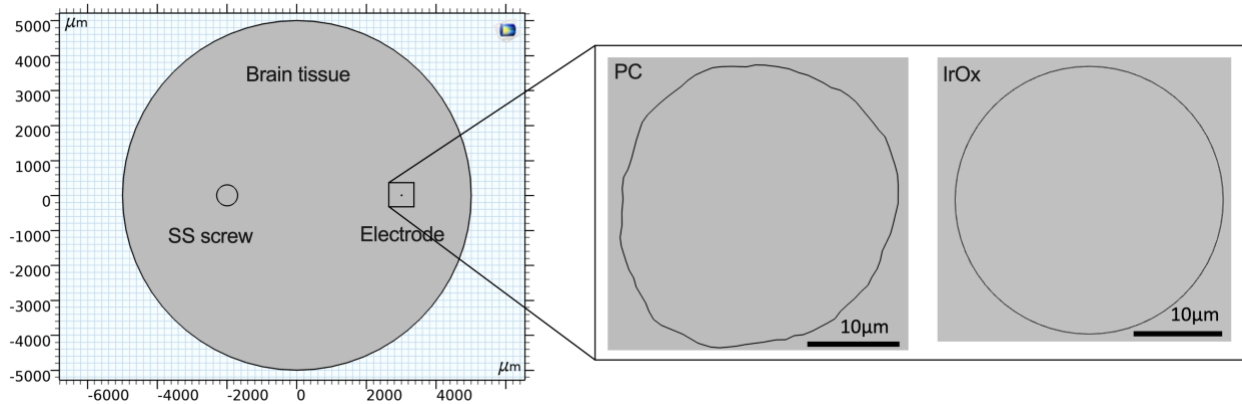


Figure 20. COMSOL simulation environment and electrode geometry. The simulated environment consists of the brain tissue, a stainless steel (SS) reference screw, and the microelectrode. Inset shows the electrode geometry for PC and IrOx respectively.

Furthermore, we applied increasing currents from 5 μ A to 60 μ A at both electrode sites and observed increasing maximum normal electric field for both materials, with PC having a higher slope than IrOx electrodes, i.e., 1.14e4 and 0.97e4, respectively. This means that the incremental increase in max voltage field nearby PC sites with incremental increase in current is larger than that nearby IrOx sites.

Table 6. Parameters describing the two-phase exponential decay function representing voltage field distribution nearby PC and IrOx electrodes.

	V _{peak}	V ₀ (V/m)	K _{fast}	K _{slow}	V _{slow} (V/m)	V _{fast} (V/m)	r (μ m)	R-squared
PC	3.9e5	4.7e4	0.19	0.036	2.4e5	1.08e5	32.5	0.99
IrOx	3.5e5	3.9e4	0.14	0.030	1.9e5	1.1e5	39.9	0.99
% difference	11.4	21	35.7	20	26	2.6	18.5	-

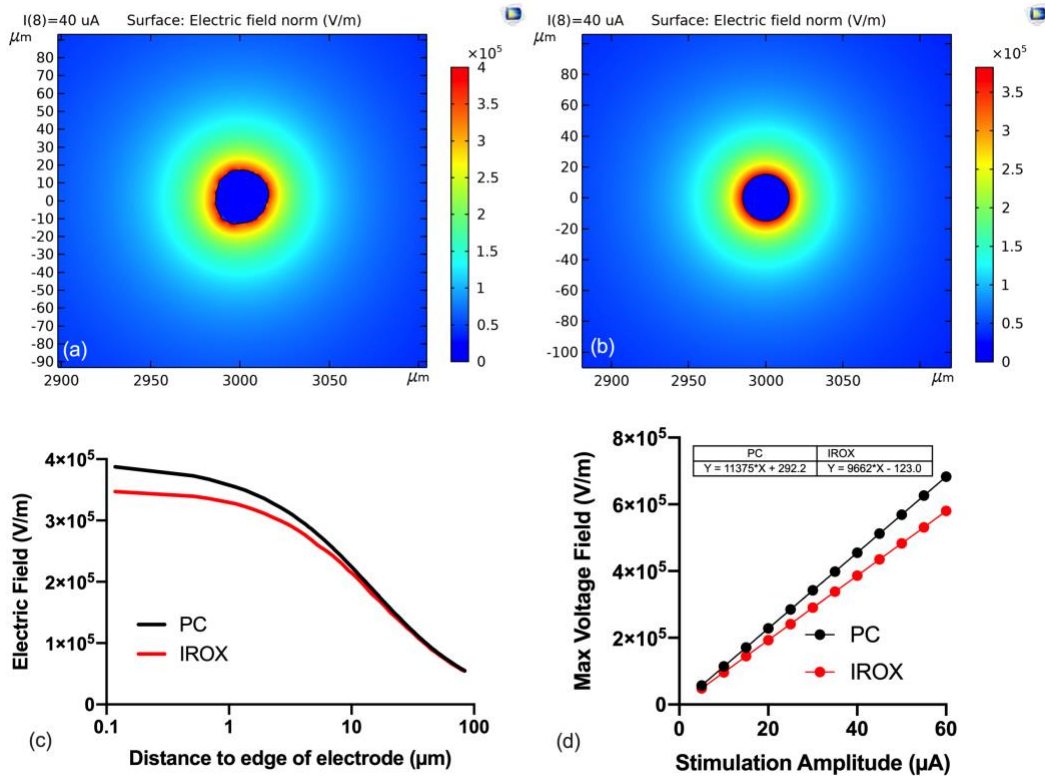


Figure 21. Finite element analysis of PC and IrOx electrode surfaces. (a) 2D Visualization of electric field distribution of a PEDOT/CNT surface with a spatial resolution of $76 \mu\text{m}^{-1}$ and spectral exponent of 1.5, as a result of a $40 \mu\text{A}$ stimulus with respect to a far-away stainless steel screw (b) 2D Visualization of electric field distribution of an IrOx surface simulated from a perfect disk, as a result of a $40 \mu\text{A}$ stimulus with respect to a far-away stainless steel screw. Both images are zoomed in near the electrode site. Colorbars represent electric field for (a,b). (c) Electric field gradient as a function of distance away from the edge of the electrode. (d) Maximum voltage field measured along the surface of the electrode as a function of virtual stimuli applied between $5 \mu\text{A}$ to $60 \mu\text{A}$.

To compare the parameter relevant for axonal activation, we calculated the activating function from the 1D extracellular voltage in response to a 40 μA stimulation across the center of both electrode materials (Figure 22a). We observed higher extracellular voltage generated by PC coated electrodes compared to IrOx coated electrodes. We calculated the activating function (second spatial difference) of the 1D extracellular voltage and saw 163% higher maximum activating function generated by PC coated electrodes compared to IrOx coated electrodes (Figure 22b,c). This suggests that for the same stimulating current amplitude, PC's higher activating function will generate higher internal currents in nearby axons which increases their probability of activation[229].

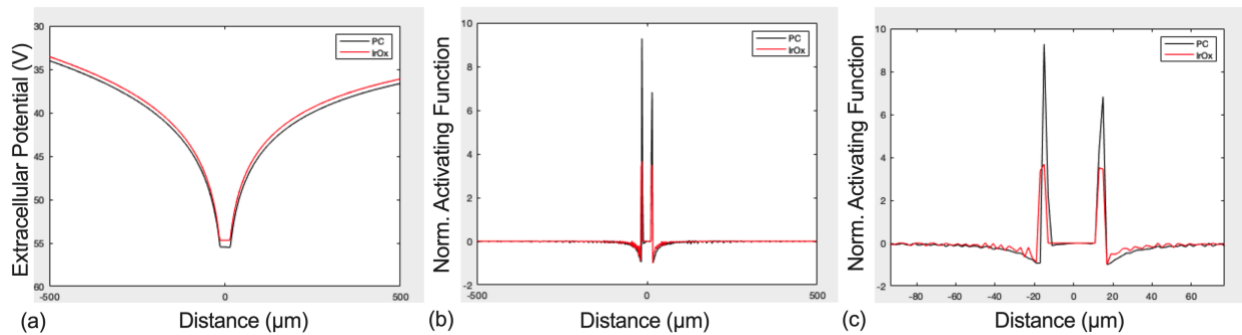


Figure 22. Activating function of the 1D extracellular voltage. (a) Profile of the extracellular field parallel to the electrodes. (b) Normalized activating function for both materials calculated as the second spatial difference from (a). (c) Zoomed in view of (b).

3.3.3 Geometric Considerations for Microelectrode Design

Based on the 2D FEM, we varied the radius and the spectral exponent of the randomly generated polar curve to gain understanding about the respective roles that radius and spectral exponent play in the electric field strength of a micro electrode. For a perfectly smooth disk electrode, we observed a more concentrated and stronger electric field with smaller diameter electrodes compared to larger diameter electrodes (Figure 23a-c). While holding radius constant, we varied the spectral exponent and observed a smaller spectral exponent result in a rough edge with higher amplitude of convolution, this resulted in more concentrated and larger electric field gradient compared to electrodes with higher spectral exponents(Figure 23d-f, Figure 24a). By taking the ratio between the perimeter and the area of the simulated electrodes, we saw increasing normalized maximum electric field strength with increasing perimeter to area ratio (Figure 24b).

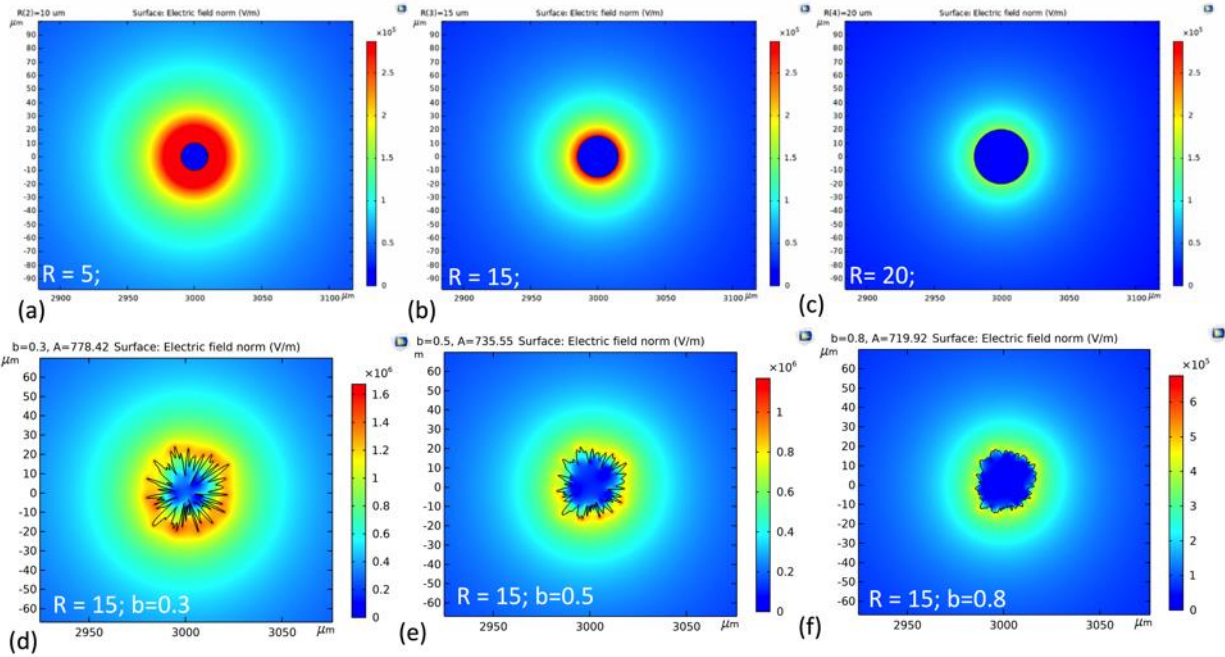


Figure 23. Geometric factors affecting electrical field distribution of microelectrodes. (a-c) 2D Visualization of electric field of IrOx with radii (a) 5 μm , (b) 15 μm , and (c) 20 μm . (d-f) 2D visualization of electric field of PC with fixed radius but varying spectral exponent, b , of 0.3, 0.5 and 0.8 respectively. 30 μA was applied to all geometry types, with respect to a far-away stainless steel screw.

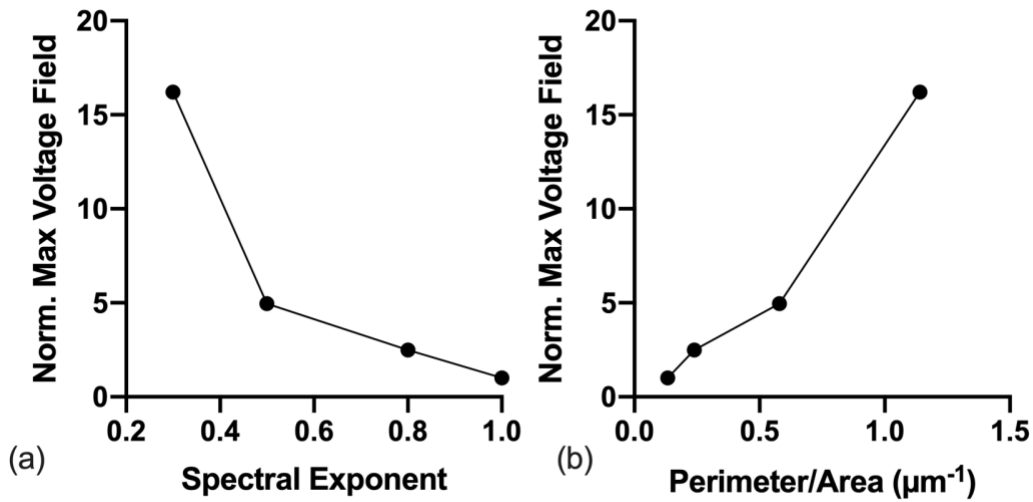


Figure 24. Quantification of geometric factors affecting electrical field distribution. (a). Normalized voltage field declines as spectral exponent increases. (b) Normalized maximum voltage field increases with increasing perimeter to area ratio. Normalization was applied to the maximum voltage field of IrOx disk electrode with a radius of 15 μm .

3.4 Discussion and Conclusion

In this chapter, we used numerical methods to explore the electrical field strength imparted by PC and IROX, each material possessing a different surface topography. We explanted electrodes from acute stimulation experiments and obtained SEM images, from which we estimated parameters for the generation of polar curve to represent the 2D surface topography of the PC electrode material. In COMSOL, we applied increasing currents from 5 μA to 60 μA at both electrode material sites and observed increasing maximum electric field strength for both materials, with PC having a higher slope than IrOx electrodes, i.e., 1.14e4 and 0.97e4, respectively, this means that the PC material can result in a larger change in electric field strength per

incremental change in applied current, leading to more power efficient electrical stimulation. Additionally, we calculated the activating function of the 1D extracellular voltage field across the center of both electrode materials and saw 163% higher activating function generated by PC coated electrodes compared to IrOx coated electrodes. Our simulation results partially support our conclusions regarding PC stimulation efficiency in Chapter 2. The nano-fibrous PC coating results higher electric field strength immediately next to electrode, thereby increasing the activating function of nearby axons.

Furthermore, there are several limitations to the modeling study. The self-affinity features of PC will depend highly on the scale they are investigated in. The derivation of topographical features in our study was from SEM images at the micro-scale whose spectral exponent resulted in a visually apparent rough topography in the COMSOL model. Additionally, the 2D simulation of electric field strength may be a modest estimation of the true electric field strength of the 3D nano-fibrous topography of PC, closer approximations of the 3D electrode topography may be achieved by performing AFM and nano-CT^[77]. In addition, our simulation assumes a perfect brain environment with homogenous conductivity, which does not describe the true *in vivo* environment with different zones of tissue compositions with varying conductance values surrounding the electrodes. Future work should incorporate these considerations along with modeling the probability of neural activation using NEURON for a more complete picture. Nevertheless, the simulation study described in this chapter supports one of our proposed mechanisms for increased stimulation efficiency of PC coated electrodes compared to IrOx, and supporting the claim that PC is a viable candidate for high efficiency electrical stimulation.

4.0 Imaging the Stability of Chronic Electrical Microstimulation Using Electrodes Coated with PEDOT/CNT and Iridium Oxide

4.1 Chapter Overview

Electrical microstimulation has partially restored vision, somatosensation, hearing and has become a potential alternative or complement to conventional pharmaceuticals for the treatment of asthma, diabetes, and gastrointestinal disorders. However, successful chronic microstimulation is faced with several challenges that require additional understanding of the stability and safety of chronic stimulation. In this chapter, we chronically stimulated the cortex of GCaMP6s mice using two high-charge-injection materials, PC and IrOx, up to 12 weeks. We observed an initial decline in stimulation efficiency in terms of integrated GCaMP intensity and radius per unit stimulation amplitude. This was followed by a trend of recovery in GCaMP intensity at week 4. Additionally, PC coated electrodes showed significantly higher efficiency in activating GCaMP compared to IrOx coated electrodes overall but not during the initial ~ 2 weeks after implantation. Using TPM, we evaluated the excitability of neural elements within 50 μm of the electrode and observed a qualitative increase in the rheobase over 7 weeks, indicating decreased excitability within the first 50 μm of the electrode center. Spontaneous electrophysiology showed a significant decline in neural spike unit count and amplitude over time for both materials. Meanwhile, *in vivo* electrochemical data showed fluctuations within the twelve-week period with moderate increases in impedance up to week 8, significant decreases in CSCc, and moderate increases in energy consumption for stimulating electrodes of both materials over time. PC coated electrodes had significantly lower impedance and delivered energy compared to IrOx coated electrodes. We

performed equivalent circuit modeling to further understand the stimulating interface and concluded that the larger pores from the nano-fibrous topography of the PC coating made it more susceptible to dramatic changes in electrolyte resistance within the coating to electrical stimulation compared to IrOx coated electrodes. Furthermore, we observed abnormal cortical responses to stimulations within the charge injection limit of both electrode materials in a subset of chronically surviving mice, providing new evidence for the potential adverse effects of widely used intracortical stimulation paradigms. Results from this study not only revealed the dynamic changes to stimulation efficiency after implantation, but also reiterates the tremendous potential for PC to be used for high efficiency chronic stimulations in neuromodulation.

4.2 Introduction

Electrical microstimulation is a technique in which electrical currents are sent through microelectrodes to excite the neuronal tissue. It only serves as a valuable tool for researchers in the neuroscience community for dissecting neural circuits, relating brain regions, studying behaviors[1-3], but also an essential method for neuromodulation. Neuromodulation via electrical stimulation has helped partially restore vision[4], somatosensation[7], hearing[5], and has become a potential alternative or complement to conventional pharmaceuticals for the treatment of asthma[202], diabetes[247], and gastrointestinal disorders[9]. The global market size for neural modulation is estimated to be USD 8.1 billion in 2019 and is estimated to grow 13.1% by 2027[10].

Safe and efficacious chronic electrical stimulation is faced with several challenges. First, to effectively stimulate a functional output, the delivered charge needs to be above the threshold charge density of the excitable tissue, yet below the charge injection limit to avoid irreversible

redox reactions. In human neural prostheses applications, the threshold charge density ranges between 5- 306 $\mu\text{C}/\text{cm}^2$ (1000-2000 μs pulse width) for epi-retinal stimulation [42, 43], and 190-2300 $\mu\text{C}/\text{cm}^2$ (200 μs pulse width) for intracortical visual stimulation [44]. Traditional stimulating electrode materials like platinum with a charge injection limit of 50-150 $\mu\text{C}/\text{cm}^2$ [41] cannot meet the full range of charge injection requirement for these applications, which drives the need for the development of high charge injection electrode materials. Second, the integrity of the implanted electrode face unique challenges *in vivo* that often lead to material degradation [30, 64-66]. Material related failure modes include fracture, dissolution and delamination of the electrode insulation and electrode metallization over the implantation duration. For stimulation applications, the failures in insulation will invite additional interstitial fluid under the existing insulation which can shunt the stimulating current, which will distribute the current by effectively a larger surface, reducing the efficiency for precise neural activation. While inert metals like platinum is considered resistant to corrosion, and iridium oxide has demonstrated much higher charge injection limit[72, 73], both can degrade or detach from the substrate upon high charge injection or prolonged stimulation load[22, 66]. Third, the implantation of the electrode devices inevitably triggers a foreign body response within the host tissue marked by the activation of microglia, breaching of the blood brain barrier, and axonal degeneration. The existing host tissue inflammation due to electrode insertion can be exacerbated by electrical stimulation. There have been reports of electrical stimulation induced vasoconstriction, thrombosis in venules and arterioles and blood brain barrier break down within 30s of stimulation at a charge density threshold necessary for a sensorimotor response or for monophasic pulses at power densities greater than 0.5mW/cm² [45-47]. Moreover, electrochemical products as a result of faradaic charge injection have been reported to increase the presence of reactive oxygen species which severely damages myelin, severely

impacting signal transduction in the neural network.[48] [49-53]. Furthermore, depending on the stimulation frequency, there may be persistent depression of neuronal excitability following stimulation of the cortex that last for several days following the cessation of the stimulation[54].

The demand for stable and efficient neural interfaces drives the development of novel materials such as the conducting polymer coating PEDOT/CNT. Its nano-fibrous surface topography drastically increases the electrochemical surface area of its underlying substrate which results in much more efficient charge transfer compared to traditional metals. Our laboratory has previously demonstrated that PEDOT/CNTs electrochemically polymerized on platinum substrates resulted in high charge injection limit of ($2.5\text{mC}/\text{cm}^2$ using -0.6V as cathodic water window), high charge storage capacity ($\sim 61.4\text{ mC}/\text{cm}^2$), and low impedances at 1kHz ($3\text{-}7\text{ k}\Omega$). The PEDOT/CNT coating remained stable after three months of soaking in PBS with continuous electrical stimulation using biphasic pulses between weeks 5-7 at $0.35\text{ mC}/\text{cm}^2$ at 50 Hz [23]. *In vivo*, PEDOT/CNT coated electrodes showed significantly lower impedances while induced significantly less neuronal death and inflammation compared to non-coated electrodes[24].

Traditionally, the characterization of efficacious electrical stimulation has been based on *in vitro* testing[96, 97], histology[24, 101], electrophysiology[106-108], and behavior[7, 110]. While these methods respectively provide unique information about the electrical stimulation, they do not allow for direct visualizations of the electrode-tissue interface. Modern imaging techniques and the rapidly developing genetic tools enable real time observations of the electrode-tissue interface. Two photon imaging and meso scale fluorescent microscopy afford us with single cell and meso scale interrogations of the brain, respectively. The ability to observe the interaction of the brain with the implanted devices has shed new light into understanding how different cellular

players and anatomical features respond to the trauma induced with an implanted electrode device[116-118, 248-251]. [34, 162, 252]

The goal of this work is to investigate the longitudinal stimulation stability and efficiency of PEDOT/CNT compared to IrOx using multiple modalities of characterization including *in vivo* imaging, electrophysiology and electrochemistry. We modified NeuroNexus planar arrays with PEDOT/CNT and IrOx, implanted them into the somatosensory cortex of GCaMP6s mice, and imaged cortical responses to electrical stimulation up to 12 weeks. To assess the health of the neurons, we measured spontaneous electrophysiology before each stimulation session. To assess stability of the implanted electrodes collected electrochemistry data. Results from this work will provide additional insight into the time course of the stability and efficiency of electrical stimulation using high performing electrode materials.

4.3 Materials and Methods

4.3.1 Animal Surgery

Aseptic surgical techniques were used throughout. Surgical details closely follow the description in section 2.3.3.

4.3.2 *In vivo* Imaging and Electrical Stimulation

The methodology of *in vivo* wide field imaging and electrical stimulation has been described in detail in section 2.3.4. Unique for this chapter, the imaging and electrical stimulation

was performed within 24 hours of the surgery (ascribed to the time point, day 1 or week 0) and weekly for 12 weeks (except for week 11). Stimulation yield is defined as the percentage of electrode sites that elicited a GCaMP response that meet the inclusion criteria (described in detail in chapter 2) for at least three amplitudes between 20 μA to 60 μA .

Neuronal excitability was defined as using the rheobase and chronaxie of neural elements. Strength-duration curves were generated by stimulating the brain from 1nC/ph—4nC/ph with varying pulse widths and amplitudes. Rheobase and chronaxie was quantified by fitting the strength-duration curve of neural elements within 50 μm of the electrode center. Where rheobase represents the current at infinite pulse width and chronaxie presents the pulse width at twice the rheobase current.

4.3.3 Image Analysis

Meso scale imaging analysis and two photon maps of threshold currents for neural element activation follows closely to methodologies described in section 2.3.5. Current amplitude for the onset of ictal phenomenon and cortical spreading depressions were identified visually by reviewing the meso scale time-series images. GCaMP responses accompanying ictal phenomenon are abnormally large in amplitude and faster in pace compared to a electrically activated GCaMP response during non-ictal state. GCaMP responses of CSDs are marked by a wave of calcium signal sweeping the cortex followed by a minute of suppressed cortical calcium activity. Abnormal GCaMP responses to stimulations were removed from analyses for the longitudinal comparison between electrode materials. This was done by removing stimulated trials that evoked GCaMP responses more than ± 3 median absolute deviations away from the mean of the GCaMP responses for each stimulation amplitude.

4.3.4 Electrophysiology

Neural spiking activities were acquired at using Ripple Grapevine via the Nano2+Stim front end and using the Trellis software. Specifically, signal streams that contain neural events that cross the threshold for a channel. The threshold is defined as 2.5 standard deviations of the spike-band-width signal. Each spike data packet consists of 52 samples captured at 30Ks/s (1.7 ms snippet) and are digitally filtered with a high pass filter of 250 Hz. Sorting of spike data was performed in Plexon offline sorter (version 3). The spike data was first sorted using the K-means automated sorting algorithm with three to five predefined clusters. The sorting results were then visually verified and incorrectly sorted units and units that consistently appeared on multiple channels (likely due to motion artifact) were discarded.

4.3.5 Electrochemistry and Equivalent Circuit Modeling

The electrode modification and characterization methods in this chapter closely follows sections 2.3.1 and 2.3.2. Equivalent circuit modeling was performed in MATLAB using a custom optimization algorithm. To reduce the low frequency noise from *in vivo* impedance measurement, the fitting was performed in between 100 Hz – 40kHz of the impedance spectrum. We chose the equivalent circuit model developed by Bisquert et al [253] which models the electrical characteristics of both *in vivo* inflammatory tissue encapsulation [254]. The goodness of fit was determined by visually inspecting the experimental data and the model data while ensuring less than 15% of absolute error between the experimental data and model fitting.

4.3.6 Explant Analysis

At the 12-week end point. We explanted the functional electrode arrays of two mice. Each array was first rinsed with an enzymatic cleaner (ENZOL) and DI water followed by an overnight soaking in trypsin at 37C. Electrochemical measurements after electrode cleaning were made using the same method described in section 2.3.2. Scanning electron microscopy (JOEL JSM 6335F) was performed at the Center for Biological Imaging (University of Pittsburgh). The samples were cleaned with isopropyl alcohol and dried before sputter coating. To enable electrical connectivity, the samples were coated with a thin layer (3.5 nm) of gold.

4.3.7 Statistics

All statistical analyses were performed in Graphpad PRISM 8.0. Two-way ANOVA mixed effects with Sidak's post-hoc were used for the following comparisons: The effect of time on neuronal activation intensity efficiency PC and IrOx coated electrodes; The effect of time on the radius efficiency between PC and IrOx coated electrodes; The effect of time on the ratio of integrated GCAMP intensity and radius compared to 1; The effect of time on single unit count and amplitude between PC and IrOx coated electrodes; The effect of time on the impedance, charge storage capacity, and energy between PC and IrOx coated electrodes.

4.4 Results

4.4.1 Longitudinal *In Vivo* Imaging of GCaMP Response to Electrical Stimulation

The cranial windows of longitudinal imaging were prepared in the same manner as described in Chapter 2 (Figure 10, Figure 25 a—c) . Neuronexus arrays were implanted at a 30-degree-angle into the somatosensory cortex of GCaMP6 mice.

4.4.1.1 Stability of Stimulation Efficiency and GCaMP Response

Electrically evoked neuronal activity from the implanted electrodes was measured via GCaMP fluorescence changes through the cranial window over twelve weeks (Figure 26) . To quantify the distance effect from the electrical stimulation GCaMP responses of neural elements within 100 μm were divided into 0-50 μm and 50-100 μm bins (Figure 27.).

The meso scale GCaMP responses in terms of maximum GCaMP intensity (Figure 28a) and integrated GCaMP intensities at distance bins 0-50 μm and 50-100 μm (Figure 28b,c) showed overall corresponding increase to increasing stimulation amplitudes over time. The overall GCaMP response intensity (Figure 28a—c) was higher at early implantation periods (weeks 0, 1) relative to the sub-chronic implantation period (weeks 4, 5), and then recovered by week 12. Likewise, the meso scale GCaMP response radius also increased with increasing stimulation amplitude. Different from trends observed with GCaMP response intensity, there was an overall lower GCaMP response radius at early implantation periods (weeks 0,1) but recovers by the sub-chronic implantation period (weeks 4,5) and remain stable until week 12.

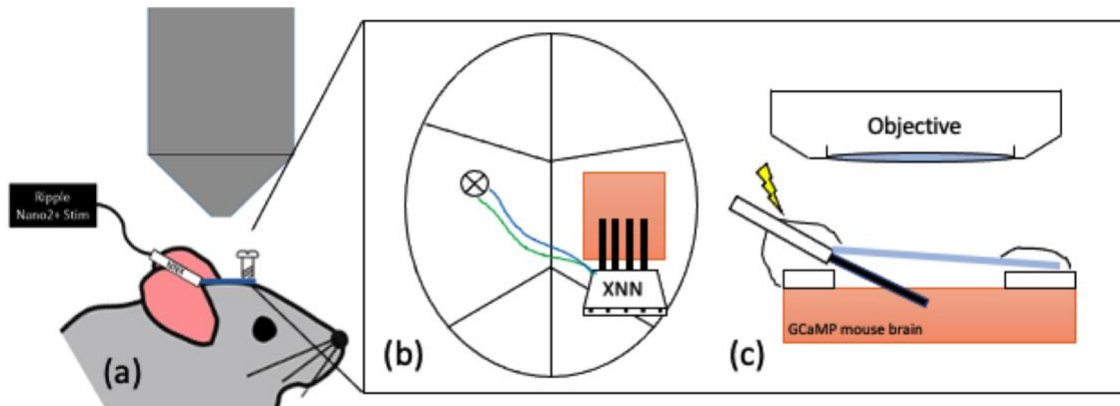


Figure 25. Experimental set up.(a) Illustration of a GCaMP6 mouse implanted with a neuronexus (NNX) electrode, connected to a stimulator with a microscope objective above the head. (b) Illustrated bird's eye view and (c) side view of the craniotomy. The electrode is implanted at a 30-degree- angle into the cortex, and the cranial window is sealed with a medical grade elastomer with a clear cover glass. The electrode is cemented in place using dental acrylic. The reference and ground wires are shorted to a stainless steel screw implanted in the contralateral hemisphere.

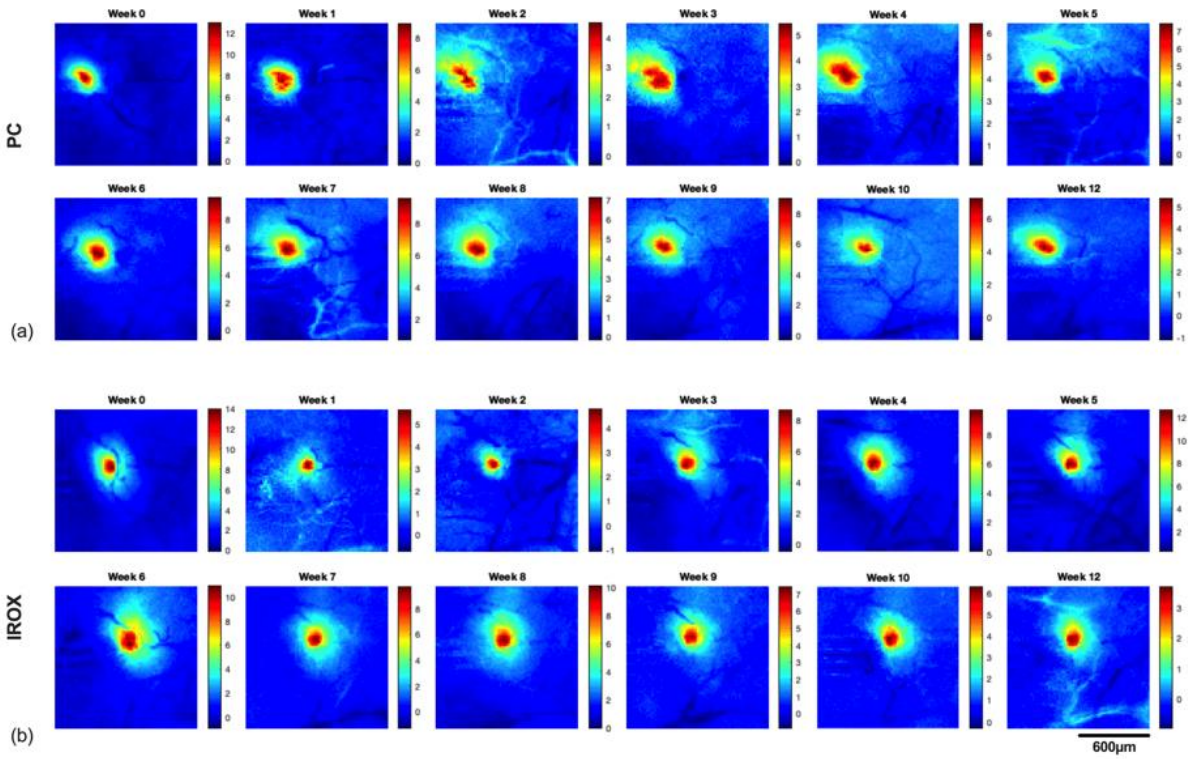


Figure 26. GCaMP responses over time. (a) Representative GCaMP responses to 30 μ A stimulations from the same PC coated electrode site over 12 weeks. (b) representative GCaMP responses to 30 μ A stimulations from the same IROX coated electrode site over 12 weeks. Color bars represent the z-score for each pixel.

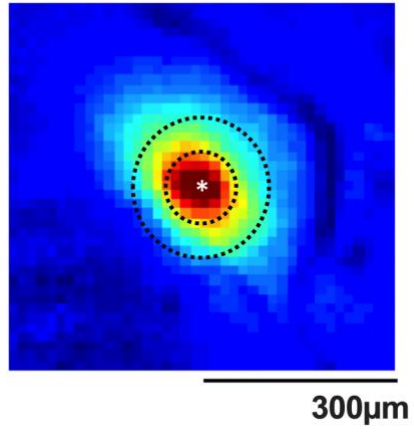


Figure 27. Example of integrated GCaMP response and binning method. Dashed concentric circles represent the 0-50 µm and 50 – 100 µm bins away from the center of the GCaMP response (denoted with an asterik).

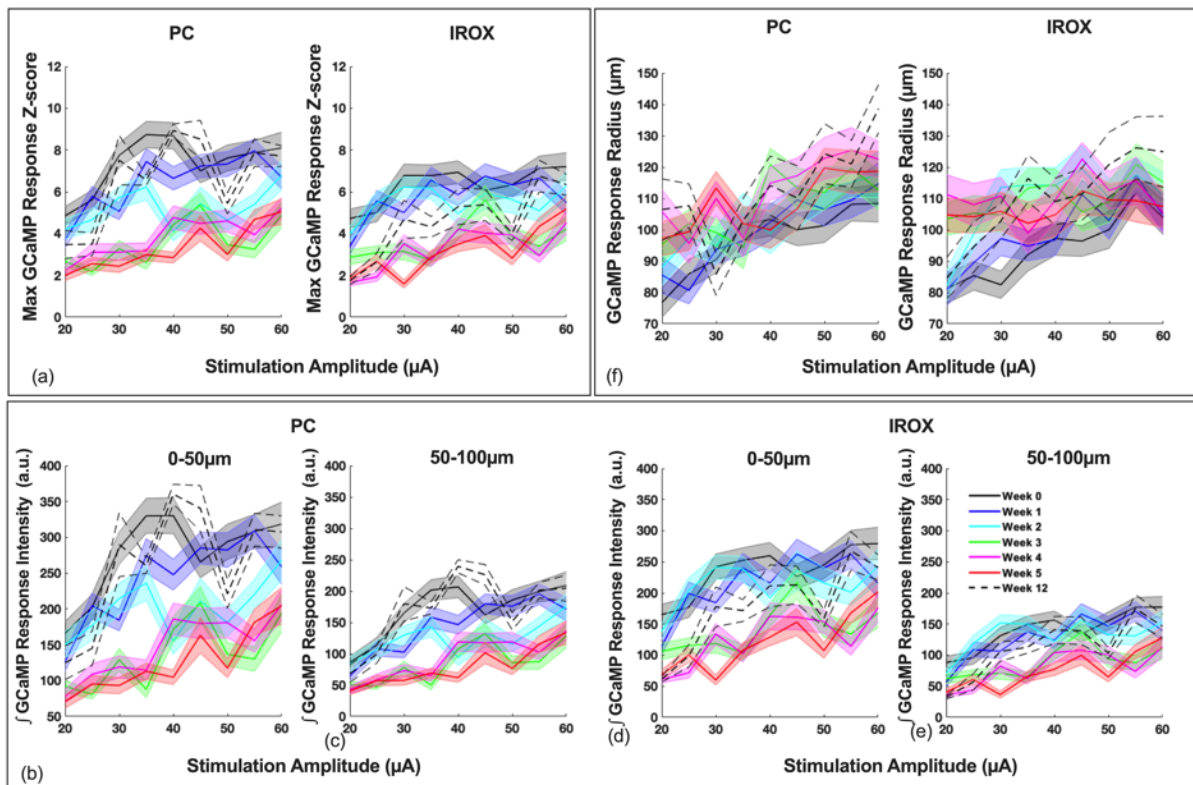


Figure 28. Quantification of GCaMP response over time. (a) Maximum GCaMP response Z-score as a function of stimulation amplitude for PC and IrOx coated electrodes. (b,c) Integrated GCaMP response as a function of stimulation amplitude activated by PC coated electrodes for bins 0-50 μm and 50-100 μm respectively. (d,e) Integrated GCaMP response as a function of stimulation amplitude by IrOx coated electrodes for bins 0-50 μm and 50-100 μm , respectively. (f) GCaMP response radius as a function of stimulation amplitude for PC and IrOx coated electrodes. For all images, shaded regions represent standard error of the mean. $n = 61-14$ electrode sites across 10-2 mice over twelve weeks, for each electrode material. Different colors represent different weeks after implantation and denoted in (e).

The longitudinal GCaMP responses were further analyzed to identify potential changes to the stability of the stimulation. GCaMP responses as a function of stimulation amplitude for each time point were fitted with linear regressions and we defined the stimulation efficiency to be the slopes of the fitting that showed p values less than 0.05. Neural activation efficiency represents the discrete recruitment of neural population for incremental changes in stimulation amplitude. PC coated electrodes exhibited significantly higher neuronal activation efficiency over the duration of the implant period at 0-50 μm ($p < 0.05$) (Figure 29**Error! Reference source not found.**a) compared to IrOx coated electrodes. Additionally, both electrode materials exhibited a significant decline in neuronal activation intensity efficiency on week 2 through week 8 compared to week 0. Neural elements within 50-100 μm of the center of the electrode exhibited overall lower neural activation efficiency compared to neural elements within 0-50 μm of the electrode. Additionally, there were significant declines in neuronal activation efficiency for both materials, beginning at week 2 for PC and week 5 for IrOx, respectively. Moreover, PC coated electrodes exhibited significantly higher neuronal activation efficiency compared to IrOx coated electrodes within 50-100 μm of the electrode center (Figure 29b). Radius efficiency represents the discrete change in the volume of activation caused by incremental changes in stimulation amplitude (Figure 29c). There was an overall significant decline in radius efficiency for both materials beginning at week 2 compared to week 0. We observed a gradual recovery in radius efficiency after week 2 that remained stable from week 6 to week 8.

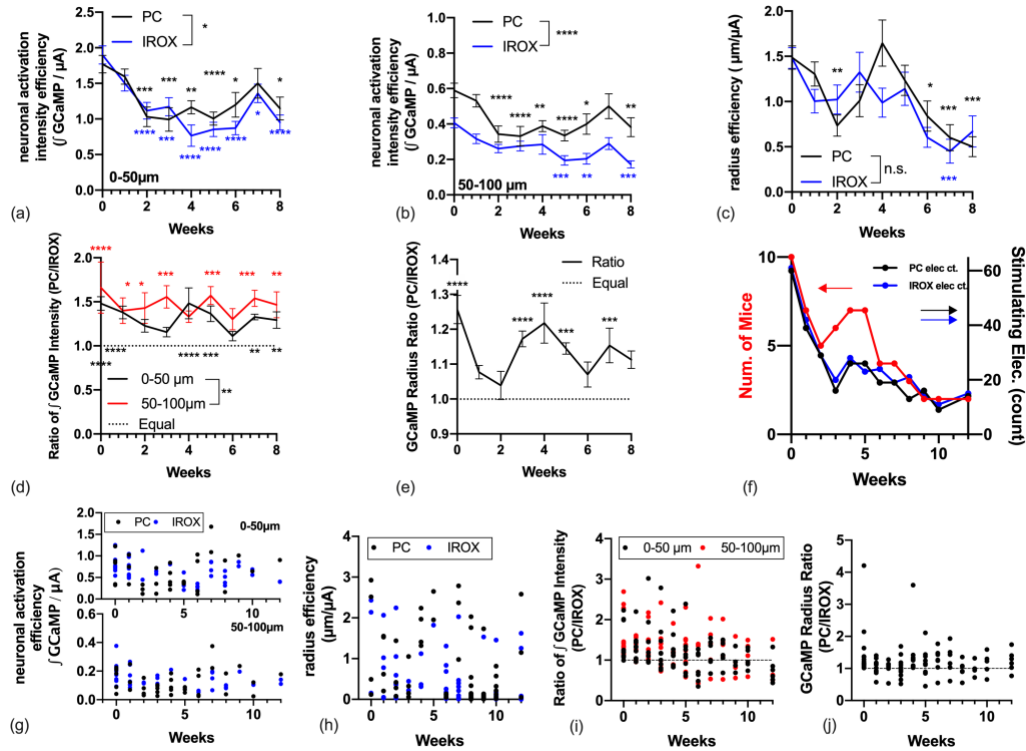


Figure 29. Quantification of stimulation stability. (a) Neuronal activation efficiency determined by the integrated GCaMP response per μA for PC and IrOx coated electrodes over time for neuronal elements within 0-50 μm and (b) 50- 100 μm away from the center of the electrode. $n = 46-14$ electrode sites.(c) Efficiency for radius of activation determined by $\mu\text{m}/\mu\text{A}$ for PC and IrOx coated electrodes. $n = 40-19$ electrode sites. For (a-c) Errorbars represent standard error of the mean. Two way ANOVA with Sidak's post-hoc. (d) Ratio of integrated GCaMP intensity (PC sites / IrOx sites) over time for neural elements between 0-50 μm and 50-100 μm . Dashed line represent a reference of equality between the two materials. Error bars represent standard error of the mean of the ratios between stimulating PC and IrOx for nine stimulation amplitudes (20- 60 μA) (e) Ratio of GCaMP radius (PC sites / IrOx sites) over time. Dashed line represents a reference of equality between the two materials. Error bars represent standard error of the mean.For all of above statistical comparisons * $p < 0.05$, ** $p < 0.01$, *** $p < 0.001$, **** $p < 0.0001$. (f) Number of mice and the total number of electrode sites analyzed for figures (a—e). (g) neuronal activation efficiency, (h)radius efficiency , (i)ratios of integrated GCaMP and (j) radius between the two materials for two mice that survived passed 8 weeks. Dots represent electrode sites from two mice.

To compare the absolute GCaMP responses activated by both materials *in vivo* we obtained the ratio of GCaMP responses activated by PC and IrOx coated electrodes. Ratios that are significantly higher than 1 indicates significant advantage of PC coated electrodes over IrOx electrodes in activating GCaMP responses. PC coated electrodes activated significantly higher GCaMP intensity within 0-50 μm of the center of the electrode at weeks 0, 1, 4, 5, 7, and 8 compared to IrOx coated electrodes. Meanwhile, PC coated electrodes activated significantly higher GCaMP intensity within 50-100 μm of the center of the electrode for weeks 0 – 3 and weeks 5, 7, and 8. Additionally, the ratio of PC to IrOx activated GCaMP intensity is significantly higher in the 50-100 μm bin compared to the 0-50 μm bin ($p < 0.01$, Figure 29d). Furthermore, PC coated electrodes stimulated larger radius of GCaMP responses compared to IrOx coated electrodes for weeks 1, 3, 4, 5, 7, and 8 (Figure 29e). Due to the invasiveness of the experimental preparation, there was a sharp decline in the number of participating mice within the first two weeks of stimulation. Mice that showed poor recovery were euthanized or allowed additional recovery before stimulation (Figure 29f). However, there were two mice that survived passed 8 weeks, and whose respective stimulation efficiency data are displayed individually in (Figure 29g-j). Data from these two mice follow trends described in Figure 29a-e for the first 8 weeks. After which both of these mice showed relatively stable stimulation efficiency.

4.4.1.2 Decrease in Neuronal Excitability Over Time

We performed electrical stimulations and imaged using TPM on a separate group of mice to gauge potential changes in neuronal excitability. Threshold maps of GCaMP responses showed a trend of increase over 7 weeks (Figure 30a-f). We fitted the strength-duration curves of electrode sites that were observable with TPM for three mice and observed a qualitative increase in rheobase (Figure 30g) and a decrease in chronaxie (Figure 30h) from week 5 to week 7.

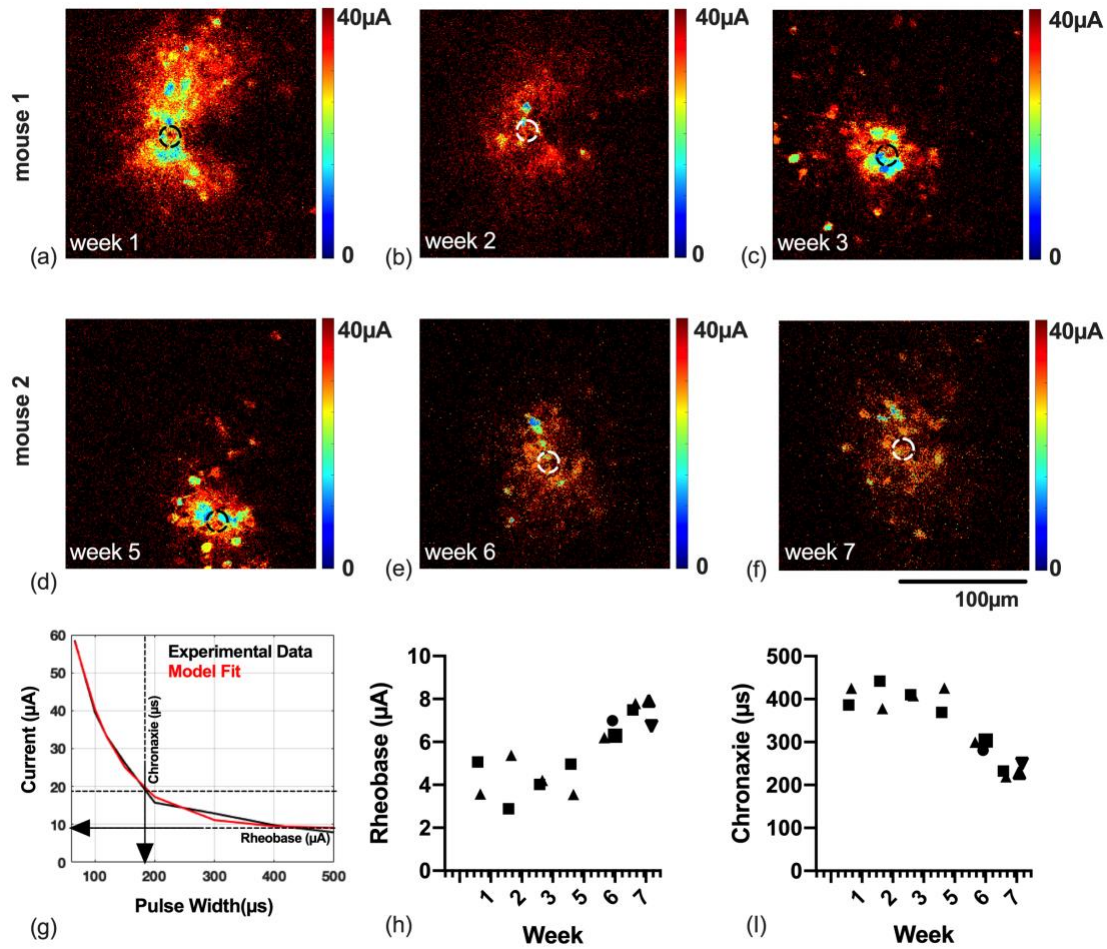


Figure 30. Two photon microscopy of neuronal excitability over time. (a-c) Representative maps of threshold current ($100\mu\text{s}$ pulse width) for neural activation from weeks 1-3 for mouse 1. Black and white dashed circles represent electrode positions. (d-f) Maps of threshold current for neural activation from weeks 5-7 for mouse 2, from the same electrode position as mouse 1. Black and white dashed circles indicate electrode positions. Scale bar represents $100\mu\text{m}$. (g) Example strength-duration curve from mouse 1. Black trace represent experimental data and red trace represent model fit. Arrows point to rheobase and chronaxie, respectively. (h) Trends of rheobase and (i) chronaxie of neural elements within $50\mu\text{m}$ of the center of the electrodes over time. Symbols represents electrode sites from 3 mice.

4.4.2 Longitudinal Electrophysiology and Changes to Electrode Functions

We measured spontaneous spike signals before electrical stimulation to gauge the activity of the neurons nearby the electrode sites (Figure 31a,b). There was an overall significant change in single unit count per electrode for both materials. Additionally, there was a trend of decreasing single unit count from weeks 0 to week 5 followed by a trend of recovery (Figure 31c). Furthermore, there was an overall significant change in the amplitude of the largest unit recorded per array over the implant duration for both materials. Similar to trends observed in Figure 31c, there is a decrease in the amplitude for the largest unit until week 5 followed by a trend of recovery but large variability in amplitudes (Figure 31). There were no significant differences between materials types in the recording of spike signals. The number of single units from mice that survived for 12 weeks showed continued stability in single unit count until week 12 where there was a slight increase in single unit count(Figure 31e). Similar trends were observed for these mice for the amplitude of maximum unit (Figure 31f).

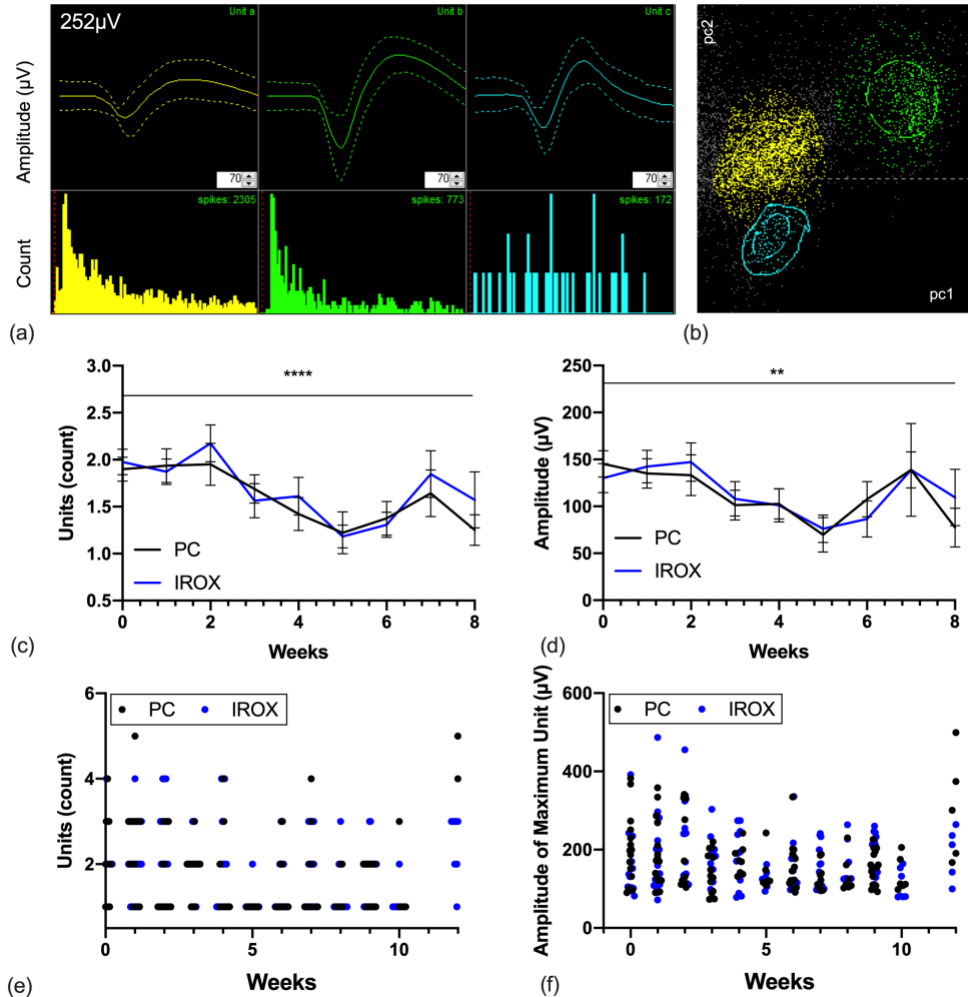


Figure 31. Electrophysiology over time.(a) Representative traces of isolated single units from an electrode site with corresponding histograms of interspike intervals and (b) first two principal components for each unit in the PCA space (screen captures from Offline Sorter). $252\ \mu\text{V}$ indicates the amplitude range for the waveform view. (c) Quantification of the number of single units on electrode sites that activated GCaMP responses over time. (d) Amplitude of the largest unit for all recording electrode sites. Errorbars represent standard error of the mean of $n = 61-14$ electrode sites that measured single units also evoked GCaMP response from $N = 10-3$ mice over time for each electrode material. ** $p < 0.01$, **** $p < 0.0001$. (e) Number of units and (f) amplitude of the largest unit for the two mice that survived passed 8 weeks. Dots represent data from each recording electrode site.

We observed dynamic changes to electrode functions over time. These functions ramify their ability to stimulate GCaMP and / or record neural signals (Figure 32). Specifically, on day 1 of stimulation, most implanted electrode sites were functional in either stimulation or recording, with the largest percentage of electrodes able to stimulate and record. A smaller fraction of electrode sites was only able to stimulate while an even smaller fraction of electrodes was able to record spike signals. However, the overall percentage of functional sites (sites that stimulate and or record) fluctuate over the implant duration with the largest fraction of non-functional (sites that did not stimulate or record) electrodes at week 3. The fraction of non-functional sites gradually decreases and stabilizes around week 6.

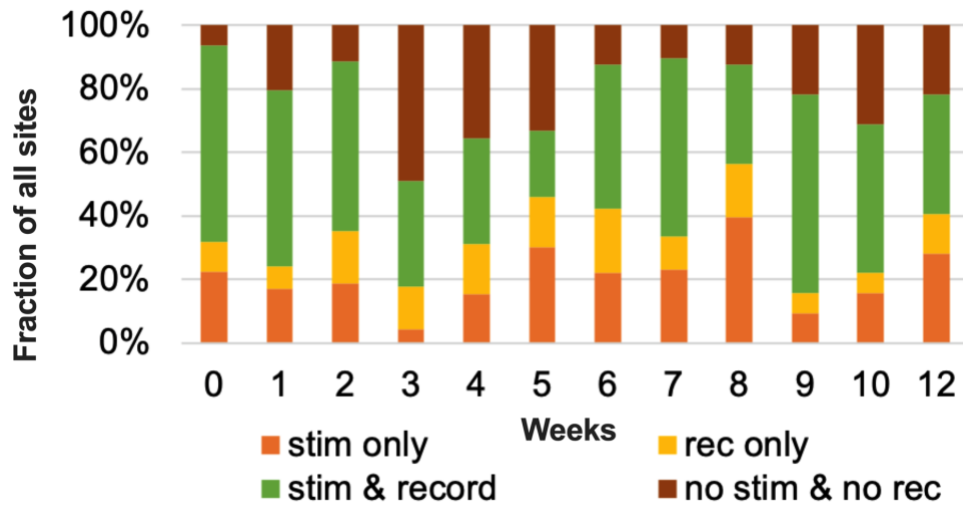


Figure 32. Functions of electrode sites over time. Colors represent electrode functions separated by their ability to stimulate GCaMP responses and / or record neural signals. Data combines both electrode materials.

4.4.3 Longitudinal Electrochemical Measurements and Equivalent Circuit Modeling

We used electrochemical methods to assess the *in vivo* stability of the electrode materials. Specifically, we measured the electrical impedances of PC and IrOx coated electrodes (Figure 33a) and quantified the 1kHz impedance over time. Stimulating PC coated electrodes had significantly lower impedance at 1kHz compared to stimulating IrOx coated electrodes over the implantation period (Figure 33b). However, non-stimulating PC coated electrodes had significantly higher impedance at 1kHz compared to non-stimulating IrOx coated sites (Figure 33c). Two mice that survived passed 8 weeks showed relatively consistent impedances in both stimulating and non-stimulating electrode sites over time (Figure 33d). We measured the charge storage capacity as a method of gauging potential changes to the electrode surface (Figure 33e). There were significant changes in the cathodic charge storage capacity (CSCc) for both materials over time. Specifically, for non-stimulating electrodes, there was a gradual reduction in CSCc through week 8. (Figure 33f). The CSCc for the two mice that survived passed 8 weeks had continuing low CSCc beyond week 8 (Figure 33h). Furthermore, we measured the voltage excursions of PC and IrOx coated electrodes (Figure 33i) and calculated the energy delivered by the system for the two materials over time. Stimulating PC coated electrodes delivered significantly less energy compared to stimulating IrOx coated electrodes (Figure 33j). However, non-stimulating PC coated electrodes deliver significantly higher energy compared to non-stimulating IrOx coated electrodes (Figure 33k). The energy consumed by both electrode materials for the two mice that survived passed 8 weeks showed stability for both stimulating and non-stimulating electrode sites after 8 weeks.

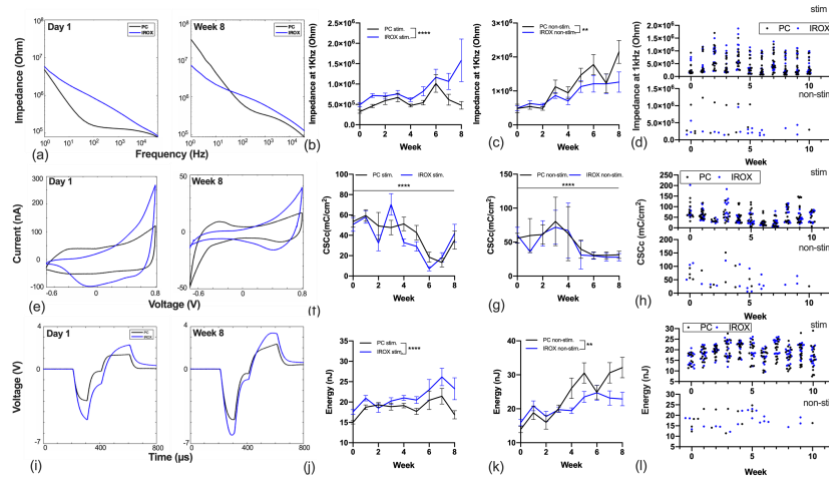


Figure 33. Electrochemistry measurements over time.(a) Full spectrum impedance modulus for electrode sites coated with PC and IrOx for (left) day 1 (right) week 8. (b) Impedance modulus at 1kHz for PC and IrOx coated electrodes that elicited GCaMP responses (fxn). Error bars represent standard error of the mean of $n = 60-17$ stimulating electrode sites $N = 10-3$ mice. (c) Impedance modulus at 1kHz for PC and IrOx coated electrodes that did not elicit GCaMP responses (non-stim). Error bars represent standard error of the mean of $n = 19-3$ non-stimulating electrode sites for each material. (d) Impedance at 1kHz for stimulating sites (top) and un-stimulating sites (bottom) for two mice that survived through week 12. (e) Representative traces of *in vivo* cyclic voltammetry for electrode sites coated with PC and IrOx for day 1(left) and week 8 (right) . (f) Cathodic charge storage capacity for PC and IrOx coated electrodes that elicited GCaMP responses (stim.). Error bars represent standard error of the mean of $n = 38-8$ stimulating electrode $N = 6-3$ mice. (g) Cathodic charge storage capacity for PC and IrOx coated electrodes that did not elicit GCaMP responses(non-stim.). Errorbars represent standard error of the mean. $n = 11-9$ electrode sites for each material of $N = 6-3$ mice. (h) CSCc for stimulating sites (top) and non-stimulating sites (bottom) of the two mice that survived through week 12. (i) Representative traces of voltage excursion from electrodes coated with PC and IrOx on (left) day 1 and (right) week 8. (j) Energy delivered from electrodes coated with PC and IrOx over time. Error bars represent standard error of the mean of $n = 41-10$ stimulating electrode sites and (i) $n = 24-12$ non-stimulating electrode sites for each material of $N = 9-3$ mice. * $p < 0.05$, ** $p < 0.01$, *** $p < 0.0001$, **** $p < 0.00001$. (j) Energy delivered from electrodes coated with PC and IrOx for two mice that survived through week 12. Dots represent data from each electrode site.

To understand the dynamic changes to the electrode tissue interface over time, we performed curve fitting of the full spectrum electrochemical impedance spectroscopy to an equivalent circuit model developed by Bisquert et al[253] (Figure 34a,b), and used by Alba et al to model electrodes coated with PEDOT/CNT/Dex[164]. The model consists of a resistive bulk tissue component (R_{ser}), a encapsulation and electrode coating component (Z_d), and the solid portion of the electrode (parallel circuit made of R_{ct} and CPE). Specifically, the Z_d circuit consists of double-channel transmission line distributed element which represents a superposition between a solid and a liquid continuum, or in other words, the tissue encapsulation and the porous region of the electrode coating, extending from the electrode surface with thickness L . The equation representing Z_d is expressed as follows:

$$Z_d = \left\{ \frac{R_0 R_1}{1 + \left(\frac{i\omega}{w_1}\right)^\alpha} \right\}^{\frac{1}{2}} \times \coth \left\{ \left(\frac{w_1}{w_L}\right)^{\frac{\alpha}{2}} \left[1 + \left(\frac{i\omega}{w_1}\right)^\alpha \right]^{\frac{1}{2}} \right\} \quad (4-1)$$

$$w_L = (r_0 q_1 L^2)^{-\frac{1}{\alpha}} = (R_0 Q_1)^{-\frac{1}{\alpha}} \quad (4-2)$$

$$w_1 = (r_1 q_1)^{-\frac{1}{\alpha}} = (R_1 Q_1)^{-\frac{1}{\alpha}} \quad (4-3)$$

Where r_0 is the resistance per unit length (ohm cm^{-1}) of the electrolyte fluid, r_1 is the charge transfer resistance length (ohm cm) of the electrolyte/solid interface, and q_1 is the coefficient of the interface CPE per unit length ($\text{F s}^{\alpha-1} \text{cm}^{-1}$). ω is the angular frequency (rad s^{-1}) and $i = \sqrt{-1}$. For fitting purposes, L is equated to 1, which results in R_0 being the total resistance of the electrolyte phase and represents the restriction to ionic motion within the pores of the coating and R_1 and Q_1 represents the total charge transfer resistance and CPE capacitance of the

electrolyte/conducting polymer boundary with α representing the CPE exponential parameter. This equivalent model is a good representation of the electrode tissue interface for both PC and IrOx as indicated in the representative fitting for day 1 and week 8 after electrode implantation(Figure 34c-f). This model can accurately depict the resistive behavior at high frequencies of the PC coating and the influence double layer capacitance for both materials at lower frequencies over time. Electrolyte resistance (r_0) for PC exhibited dynamic changes from week to week with statistical significantly higher electrolyte resistance at weeks 2 and 6 compared to week 0. The increasing in electrolyte resistance at week 2 are likely contributed by the accumulation of cells and proteins that could fill the pores of the PC coating. After week 2, electrical stimulation from week to week may result in variable amount of tissue within the PC film, resulting in variable electrolyte resistance. Meanwhile, the electrolyte resistance for IrOx exhibited no statistically significant change over time. This can be largely attributed to the dramatically smoother surface topography and smaller pore size within the IrOx film compared to the PC coating such that the majority of the electrolyte resistance are influenced by the tissues encapsulating the electrodes. However, there was an overall significantly lower electrolyte resistance within the PC Zd component compared to IrOx (Figure 34g) due to the higher electrochemical surface area from the nano-fibrous surface topography of PC compared to IrOx sites. This provided ions ample room to diffuse across. Moreover, the capacity coefficient (Q_1) of the Zd component for PC coated electrodes showed dynamic significant changes throughout the implantation period with significantly higher capacitance compared to IrOx coated electrodes on day 1 (week 0) after implantation (Figure 34h). The CPE coefficient remained stable with no significant changes over time and between electrode materials(Figure 34j). Likely contributed by

the infiltration of astrocytes which could block the pores of the coating and increasing resistance for ionic diffusion.

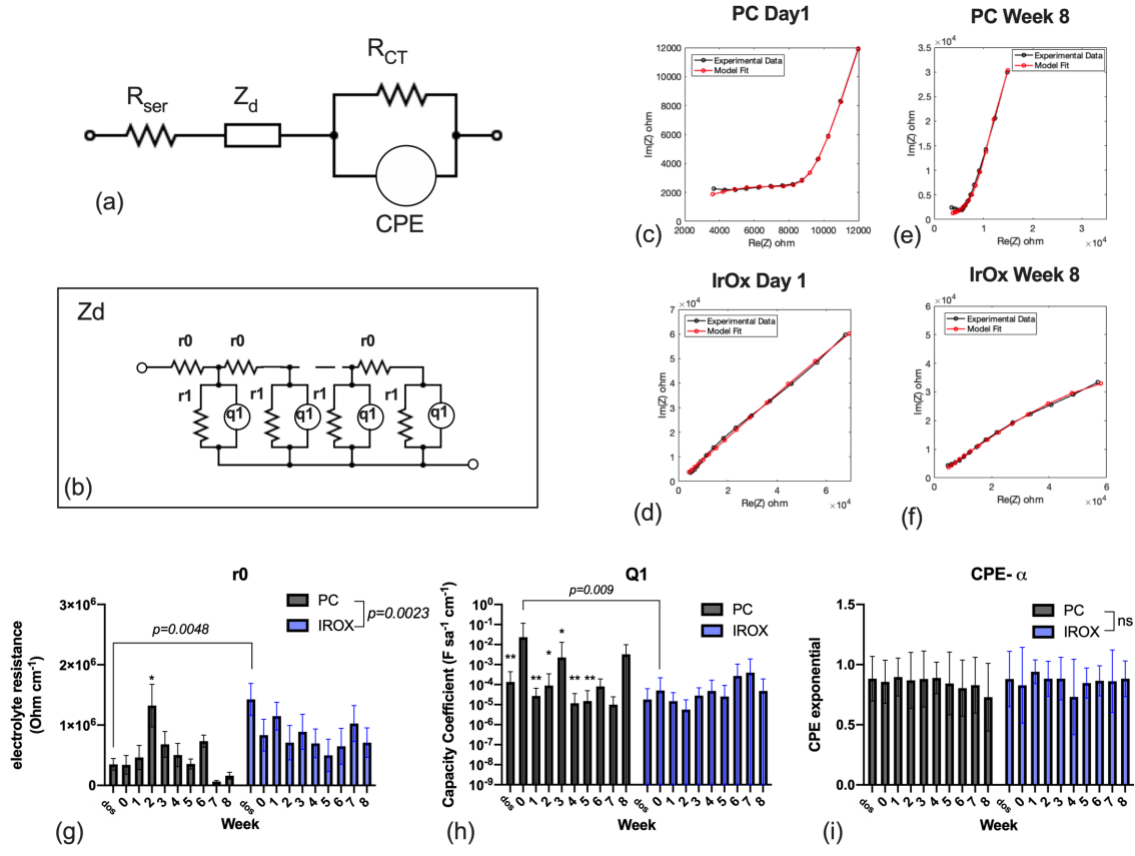


Figure 34. Equivalent circuit modeling. (a) Diagram of an equivalent circuit model representing the electrode tissue interface. R_{ser} represents the resistivity of the bulk tissue. Z_d is a diffusion impedance element representing the porous continuum between the tissue encapsulation through the electrode coating. R_{ct} represents the faradaic charge transfer resistance of the solid portion of the electrode, and CPE represents the double layer capacitance of the solid portion of the electrode. (b) Details of the Z_d circuit, where r_0 is the electrolyte resistance (ohm cm^{-1}) through the pores of the electrode coating and the encapsulation, and r_1 is the charge transfer resistance length (ohm cm). q_1 is a CPE representing the electrolyte/ conducting polymer boundary. (c,d) Representative fitting for a PC and a IrOx electrode on day 1. (e,f) Representative fitting for a PC and a IrOx electrode at week 8. (g) Electrolyte resistance (r_0) over time. PC coated electrodes had overall significantly lower electrolyte resistance compared to IrOx coated electrodes. $*p < 0.05$. (h) Capacity coefficient Q_1 for the q_1 CPE element in (b). There was a significant reduction in the capacity coefficient for PC coated electrodes in weeks 1- 5 compared to week 0. (i) CPE exponential, α , of the Z_d circuit. ($n = 26 - 5$ electrode sites from 7 –3 mice chronically surviving mice).

4.4.4 Stimulation Induced Changes to Electrophysiology

In this study, we observed incidences of ictal phenomenon, many of which were followed by cortical spreading depression (CSD) during microstimulation. These events were manifested in the abnormally high GCaMP response magnitude and response rate to stimulation compared to a normal GCaMP response. The current amplitude for the occurrences of ictal phenomena ranged between 40 μA and 60 μA while the current for the occurrences of CSDs ranged between 45 μA and 60 μA . (Figure 35a,b). Of these mice that exhibited abnormal neurological events during microstimulation, there was a significant decline in neural recording performances in terms of the number of units per channel (Figure 35c) and amplitude of the largest unit per channel (Figure 35d) for both materials in the two minutes immediately following a stimulation session. Accompanying this was a drastic reduction of the number of electrode sites that were recording neural signals (Figure 35e). Contrastingly, where no abnormal neurological events occurred during microstimulation, the significant differences in the number of units recorded were observed weeks 0 and 1. And significant decline in the largest amplitude recorded on the array at week 1 (Figure 35f,g), with occasional increase in the number of recording electrodes over time (Figure 35h). The significant reduction in recording performance post stimulation were likely due to the increased the overall metabolic demand from the acute injury in the environment resulting in reduced neuronal activity after electrical stimulation. For both electrode materials, there were significant decreases post stimulation in the 1kHz impedance (Figure 35i,j). Particularly for PC coated electrodes, there was a significant decrease in the electrolyte resistance across the Zd component after electrical stimulation, but no significant change was detected for IrOx coated electrodes (Figure 35k,i).

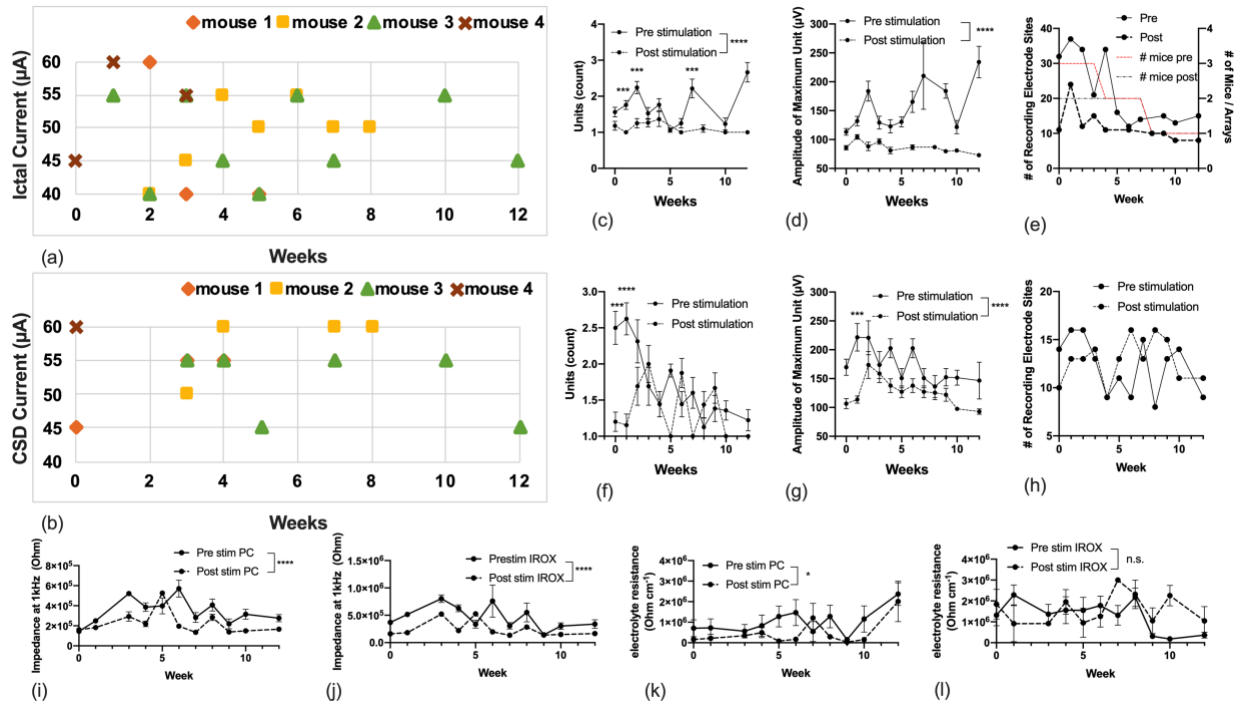


Figure 35. Observation of abnormal cortical events during microstimulation.(a) Current for the onset of ictal phenomenon for four mice over 12 weeks. (b) Current for the onset of cortical spreading depression for four mice over 12 weeks. (c) Number of single units before and after electrical stimulation for PC and IrOx coated arrays for mice that showed cortical spreading depression (d) Amplitude of largest unit on array before and after stimulation for mice that showed cortical spreading depression. (e) Number of electrode sites that were recording neural spikes before and after stimulation. Dashed red and black lines represent the number of mice for each time point with electrophysiology data. (f) Number of single units before and after stimulation for one mouse that did not show cortical spreading depression. (g) Amplitude of largest unit on array before and after stimulation for one mouse that did not show cortical spreading depression. (h) Number of recording electrode sites for the mouse in (g,h) over time before and after electrical stimulation. (i,j) Impedance at 1kHz for the mouse in (e,f) before and after electrical stimulation. $n = 8$ sites for each electrode material. **** $p < 0.0001$. (k,l) electrolyte resistance across the Zd diffusion layer (r_0) for PC and IrOx coated electrodes, respectively. $n = 3-7$ electrodes that showed adequate model fit over time for PC and $n = 4-8$ for IrOx. Error bars represent standard error of the mean. * $p < 0.05$.

4.4.5 Explant Investigation

To examine the effects of chronic implantation and electrical stimulation on the electrode arrays. We explanted functional arrays of two mice after 12 weeks of implantation. Both the 4x4 type and the linear type array exhibited various levels of material degradation. Using bright field microscopy, we could observe the black appearance characteristic of the PC coatings. However, for the linear array, the black appearance of PC coatings was not apparent for superficial electrode sites (Figure 36a,b). The 12-week implantation and stimulation *in vivo* resulted in a trend of increased electrical impedance for both materials, due to the variability between electrode sites for each material in the explanted scenario, the increase in impedance was not statistically significant. Additionally, the impedances of PC coated electrodes were significantly lower than IrOx coatings in both the pre-implant and explanted measurements (Figure 36c). Furthermore, the CSCc for both materials showed a significant decrease explant compared to pre-implant (Figure 36d). Moreover, there was a significant reduction in charge injection limit for PC coated electrode sites explant compared to pre-implant (Figure 36e). We examined the surface features of the explanted arrays using SEM and observed varying levels of material degradation and tissue adherence for both materials. While some PC sites remained intact over the implant duration, others exhibited features of partial or complete delamination accompanied by tissue encapsulation on the coating material (Figure 36f). Similarly, IrOx sites have exhibited complete or partial delamination or cracking while other remained intact. IrOx degradations were also accompanied by encapsulation that were resistant to our enzymatic treatment (Figure 36g).

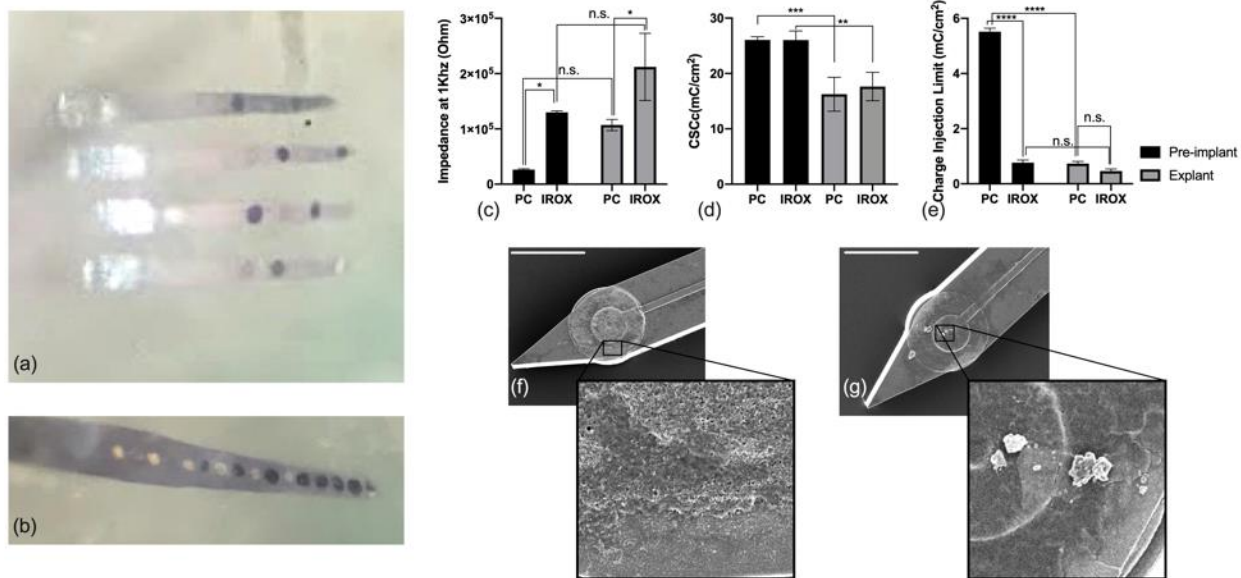


Figure 36. Explant analysis.(a,b) optical micrographs of four-shank and single shank arrays coated with PC and IrOx. (c) Impedance at 1kHz of electrodes coated with PC and IrOx as pre implants and explants. * $p < 0.05$. (d) Cathodic charge storage capacity of electrodes coated with PC and IrOx as pre-implants and explants. ** $p < 0.01$, *** $p < 0.001$. (e) Charge injection limit of electrodes coated with PC and IrOx as pre-implants and explants. **** $p < 0.00001$. (f) SEM of an explanted PC electrode. Inset shows magnified view of the explanted surface. Note evidences of coating delamination and tissue adherence on the surface of the electrode site. (g) SEM of an explanted IrOx electrode. Inset shows a magnified view of the explanted surface. Note evidences of cracking in the IrOx thinfilm and tissue coverage on the surface of the electrode.

4.5 Discussion

The development of modern imaging techniques and transgenic tools enable observations of neural dynamics to electrical stimulations in real time. In this work, we conducted a longitudinal study on the stability of electrical stimulation performance of two high-charge-injection materials, PC and IrOx. Using NeuroNexus arrays modified with PC and IrOx on alternating sites, we stimulated the somatosensory cortex of GCaMP6s mice for up to twelve weeks using both meso scale fluorescence imaging and up to seven weeks using two photon imaging. We observed an initial decline in stimulation efficiency in terms of integrated GCaMP intensity and radius per unit stimulation amplitude. This was followed by a trend of recovery in GCaMP intensity at week 4. Additionally, PC coated electrode showed significantly higher efficiency in activating GCaMP compared to IrOx coated electrodes. Using TPM, we evaluated the excitability of neural elements within 50 μm of the electrode and observed a qualitative increase in the rheobase over 7 weeks, indicating decreased excitability. We acquired spontaneous electrophysiology data before stimulation each week. There was a significant decline in neural spike unit count and amplitude over time for both materials. Meanwhile, *in vivo* electrochemical data showed fluctuations within the twelve-week period with moderate increases in impedance up to week 8, significant decrease in CSCc, and moderate increase in energy consumption for stimulating electrodes of both materials. We performed equivalent circuit analysis on the impedance data and saw significantly lower electrolyte resistance within the electrode coating and encapsulation for PC coated electrodes compared to IrOx coated electrodes. Furthermore, at the twelve-week end point we explanted the functional arrays of the two surviving mice and observed various changes to electrode coating for both materials.

4.5.1 Fluctuations in Stimulation Efficiency Revealed through *In Vivo* Imaging

We quantified the stability of electrical stimulation using activated GCaMP responses in terms of (1) stimulation efficiencies for each electrode material, i.e., the neuronal activation efficiency and the radius efficiency (Figure 29 a-c), and (2) the ratio of the GCaMP activation magnitude between the two materials (Figure 29d,e). We defined two zones for the quantification of neuronal activation efficiency, 0-50 μm and 50-100 μm . In the acute injury phase (weeks 0 –2) we observed a significant decline in neuronal activation efficiency in 0-50 μm for both materials and a significant reduction in neuronal activation efficiency for PC in 50 -100 μm . The transient decrease in stimulation efficiency after day one may stem from changes to the neuronal network excitability immediately after the implantation of an electrode which heightened the neuronal response to electrical stimulation on day 1. Here, the GCaMP fluorescent signal is an ultrasensitive indicator of action potential events[255]. Borrowing evidences from mild traumatic brain injury brain slice patch-clamp studies, in acutely injured tissue, both the intact and axotomized neurons exhibited significantly higher action potentials (AP) compared to neurons in the un-injured tissues. By 48 hours post injury, axotomized neurons continued to have high action potential amplitude whereas the APs in intact neurons recovered compared to neurons in the uninjured tissue. The changes in AP amplitude have been thought to be attributed to various factors such as possible changes to the densities of Na⁺ channels or the K⁺ ATPase pumps after injury, however, a consensus has not yet been reached regarding the specific mechanism [256] [257]. Meanwhile, the radius efficiency also saw a significant reduction within the first 2 weeks. The severing of network connections due to the acute electrode implantation likely caused axonal injury near the electrode, preventing the recruitment of distant neural elements.

We saw significantly lower neuronal activation efficiency for both materials from week 2 to week 8 for both electrode materials compared to week 0. However, we observed a recovery in radius efficiency after week 2, and this remained relatively stable until week 5. The recovery in radius efficiency could be facilitated by the regenerating and re-establishing axonal connections after the initial electrode insertion trauma, allowing for recruitment of neural elements farther away. The significant decline in radius efficiency after week 5 could be explained by the maturation of the astrocytic scar around the electrode site, increasing the electrode-tissue interface impedance [93], while increasing the distance between the electrode and excitable tissue. Additionally, from the equivalent circuit modeling result, we saw a qualitative increase in the electrolyte resistance from weeks 5-8 for IrOx coated electrodes (Figure 34g), which could suggest that the buildup of encapsulation impeded ionic diffusion across the interface, preventing the activation of neural elements farther away. Nevertheless, PC coated electrodes had significantly higher average stimulation efficiency compared to IrOx coated electrode sites in terms of neuronal activation efficiency. In Chapter 2, we concluded that PC coated electrodes activate significantly more intense and broader GCaMP responses compared to IrOx coated electrodes in the acute setting. Herein we conducted a longitudinal experiment to investigate if the advantage of the PC coated electrodes in efficient neural stimulation sustains chronically. Same as comparisons made in Chapter 2, to account for the heterogenous GCaMP expression and neuronal densities across the cortical depth, we obtained the ratio of the GCaMP response between PC and their IrOx counterparts. We observed significantly higher integrated GCaMP intensity activated by PC coated electrodes compared to IrOx coated electrodes in within 50 μm of the electrode over the implantation period (Figure 29d). However, at weeks 2 - 3, there were no significant difference between electrode materials in the magnitude of the integrated GCaMP responses. This is likely

due to (1) the significantly reduced neural elements within 50 μm coupled and (2) the infiltrating inflammatory macrophages and initiation of astrocyte activity in weeks 2 and 3 potentially filling in the pores of the PC coating, which increased the electrolyte resistance of the PC coated electrodes (Figure 34g), overriding the benefit the PC coating provides. As the interface recovers with re-established axonal connections along with refreshed PC coating pores after electrical stimulation, the benefit of the PC coating re-emerged. Another potential explanation of PC coatings regaining its higher stimulation efficiency may be supported by evidences in the literature, wherein carbon nanotubes have been demonstrated to support neurite outgrowth[158], neuronal health, and reducing inflammation[24]. We observed continuously higher integrated GCaMP intensity stimulated by PC coated electrodes in 50-100 μm throughout the implantation period (Figure 29d) compared to the 0-50 μm bin, likely due to (1) higher neural element survival farther away from the implant location[258, 259], and (2) PC coated electrodes stimulating larger activation radius compared to IrOx coated electrodes. Meanwhile, PC coated electrodes activated significantly larger radius of neural element compared to IrOx over the implantation period except for weeks 1 and 2 where there were degenerating axons from the insertion of the electrode. As new connections form, additional neurons were recruited, and the benefit of the PC coating re-emerged (Figure 29e). Using TPM, we examined the excitability of a separate cohort of three mice with the same preparation. We quantified excitability in terms of the rheobase of neural elements within 50 μm of the electrode. There was a qualitative increase in rheobase and decrease in chronaxie from week 5 to week 7, suggesting a decrease in excitability for neural elements in this region. Supporting this observation, the Purcell group has performed *ex vivo* studies on quantifying the expressions of ion channels involved in neuronal signal transduction, they have found a progressive increase in potassium channel expression and a reduction in sodium channel

expression that accompanied a 6-week signal loss in terms of local field potentials and the number of single units, changes to these ion channel expressions have been shown to reduce excitability of neurons[260]. Accordingly, we have also observed a decline in neuronal signal within this period (Figure 31).

4.5.2 Longitudinal Changes in Electrophysiological Measurements

Recordings of spontaneous spike activity showed an overall significant decline in single unit counts and the amplitude of the largest unit for both materials. However, there was no significant decline in neural recording performance for either materials within 2 weeks after implantation as observed in the stimulation efficiency investigation. This observation may be explained by the differing mechanisms in neural recording and stimulation. In neural recording, the signals were more likely to be coming from the cell soma whereas stimulation is initiated at the axons. As previously characterized in our laboratory, the implantation of an electrode into the neural tissue assert mechanical strains on the neuronal somas, which increases the intracellular calcium levels, but more aggressively sever the axons and neurites perpendicular to the path of the electrode insertion. This results in acute neurite “blebbing”, which are swollen, hypertrophic spherical bodies that develop along neurites following trauma[118]. Sustained high levels of intracellular calcium and axonal blebbing have been reported to promote neural degeneration and the loss of synaptic connectivity. The loss of synaptic connectivity prevents the additional recruitment of distant neurons with electrical stimulation but may not change the spontaneous activity of intact neurons nearby the electrode. We observed a more gradual decline in neural recording performance in both electrode materials, and we attribute this observation to (1) the gradual buildup of the glial scar around the electrode sites, and (2) the continuous neural

degeneration in the immediate vicinity of the electrode due to persistent blood barrier disruption triggering additional inflammations that lead to neuronal death as a result of micro-motion, respiration, and animal movements. We surveyed electrode functions in their abilities to stimulate and record neural activity and found fluctuations in electrode functions over time. While a large fraction of electrode sites was capable of both stimulation and recording, a small fraction of electrodes could only stimulate or record neural activity. Electrodes that only stimulated may be distant from a neuronal soma but close enough to an axon hillock for initiation of action potential. Electrodes that only recorded may have undergone material degradation that prohibits the inject sufficient charge to reach threshold of neural activation. Electrode sites that neither stimulated nor recorded likely sites that were superficial and sites whose traces may have corroded as a result of a chronic material degradation mechanism.

4.5.3 PC is a more Energy Efficient Material for Chronic Stimulation

We performed comprehensive *in vivo* electrochemical measurements of both electrode materials chronically and observed distinct differences in the electrochemical features of electrodes that activated GCaMP responses versus electrodes that did not in terms of impedance at 1kHz and energy consumption (calculated by integrating the absolute value of the product of current and voltage over time). Specifically, electrodes that activated GCaMP responses showed relatively stable impedance fluctuations not exceeding an average of 1.5 M Ω over time while electrodes that failed to activate GCaMP responses showed continuous increases in electrical impedance up to an average of 2M Ω over time. In addition, non-stimulating PC coated electrodes showed significantly higher electrical impedance and delivered higher energy compared to IrOx coated electrodes. Many of these electrode sites were in the superficial regions of the cortex. The

superficial electrode sites not only need to endure the mechanical stress imposed by brain micromotion and drastic animal movements, there is additional shear forces on the electrode material as electrode fluctuates in and out of the brain parenchyma, likely overcoming the primarily Van der Waals bonding force of the PC coating with the iridium substrate, resulting in accelerated electrode material degradation. Explant investigations showed that many PC coating delamination indeed occurred in superficial sites in the linear array with no location specific material degradation in multi-shank arrays. The degree of material degradation is less in IrOx coated superficial sites possibility due to its smoother surface topography which reduces its friction with the brain tissue, preventing catastrophic delamination. The sudden drop in electrode impedance and energy at week 7 end point may be attributed to the dynamic changes to the stimulating interface from week to week, along with the possibility of stimulating induced opening of the pores within the PC coating and within the encapsulation of the IrOx coated electrodes. Investigation of the Z_d parameter of the equivalent circuit, we observed a significant drop in electrolyte resistance within the PC coating at week 7 compared to week 6 (Figure 34g). This change also corresponds to the increased stimulation efficiency and increased single unit amplitudes at week 7. Furthermore, both materials exhibited significant decline in CSCc over time with no significant differences between material types. Both electrode materials are porous with high electrochemical surface areas after modification. *In vivo*, electrode surfaces undergo biofouling, in which various proteins and cells adhere to the electrode surface as a result of the foreign body response, this will reduce the electrochemical surface area thereby decreasing the charge storage capacity. Nevertheless, comprehensive electrochemical measurements of both electrode materials suggest that PC is a better candidate for higher energy efficient stimulation compared to IrOx. This is supported by (1) the significantly lower electrical impedances at 1kHz

for functional electrodes over the duration of the implant compared to IrOx (Figure 33b) and (2) significantly lower electrode potential from PC coated functional electrodes (Figure 33j). These features will increase the safety of stimulation and reduce the power consumption in chronically implanted pattern generators, reducing the frequency of battery replacement surgeries.

4.5.4 Abnormal Cortical Events to Electrical Microstimulation

In this study, we observed numerous ictal phenomena during microstimulation. These events manifested in the abnormally high GCaMP response magnitude and response rate to stimulation compared to normal GCaMP responses. Some cases of the ictal phenomenon were followed by cortical spreading depressions marked by sweeping calcium events across the cortical surface and silencing of the cortex, lasting up to a minute, with gradual but eventual recovery of spontaneous calcium activity. While we have no definitive answer to the exact mechanism for which these incidences occurred, there are several potential explanations. In seizure research, electrical kindling is used as a tool to reliably initiate seizure activity in animal models which was first proposed by Goddard et al[261]. The kindling is induced by repeated stimulation that evokes afterdischarges (AD), which are high amplitude, rhythmic activities observed in the electrocorticogram (EEG), outlasting the stimulus train[262], these EEG activities can be inferred with GCaMP signals in our study. The parameters for electric kindling typically consists of trains of pulses 1-2 s in duration, 1 ms in pulse width, and 25—150 Hz in frequency [263]. Current threshold for kindling are determined by increasing stimulation amplitude at small increments until AD occurs, which can vary between animals and animal models[264]. While the mechanical trauma introduced by the insertion of an electrode could contribute the onset of CSDs, as revealed in our previous investigation[118]. It is unlikely that the chronic presence of the electrode

promoted the occurrence of CSDs in our study because they were only linked to electrical stimulations above $40 \mu\text{A}$ (or 4nC/ph Figure 35a,b). Also supporting this claim, Cela et al reliably triggered epilepsy in layers II/III using optogenetics[265]. The occurrence of CSDs could be due to repeated neuronal depolarizations which could increase the extracellular glutamate and potassium concentrations to cytotoxic levels, increasing the likelihood of epilepsy[266]. In our study, the neuronal suppression after CSDs were reversible; while the number of units and the amplitude of the units significantly declined after electrical stimulation, these metrics showed improvement prior to electrical stimulation the following week (Figure 35c,d). Mice that did not experience CSDs showed less changes in overall recording performances before and after stimulation except for the first week, a period in which the overall health of the interface was poor due to the electrode implantation and acute inflammation (Figure 35e,f). There was an overall significant reduction in signal amplitude over time. This is likely because electrical stimulation potentially opened additional pores in the encapsulation, which reduced electrical impedance for both materials (Figure 35i,j) and reduced the electrolyte resistance for PC coated electrodes (Figure 35k) . While these kindling events only occurred in a subset of our subjects, the delivered charge per phase, duty cycle and stimulation frequency are in the range of values used in other animal models and human studies, calling for further studies to investigate if they cause any permanent neural damage and how to avoid them [7, 267-270].

4.5.5 Limitations and Future Research

In addition to the same limitations mentioned in Chapter 2. The chronic study has their own limitations. Prior to implantation, *in vitro* characterizations of the charge injection limit of both electrode materials indicated that our maximum current amplitude 6nC/ph was below the -

0.6V hydrolysis window for both electrode materials. However, as revealed by explant analyses, there were cases of electrode material failure such as cracking and delamination. These material failures will inherently reduce the effective surface area for stimulation and reducing the charge injection limit. However, using our stimulation paradigm, we did not observe overt signs of gas evolution as observed in using electrode rejuvenation protocols (monopolar 4s +1.5V [118]). Furthermore, due to complications that often arise with chronic cranial windows, the number of mice used in the study decreased rapidly after implantation with only two mice with clear cranial window and functional electrodes beyond week 8. The drastic decline in animal number (correspondingly, the number of electrode sites) could reduce the statistical power beyond week 8. Therefore, data beyond week 8 were presented as individual data points. Future investigations should consider alternative cranial sealing methods [120] and using arrays that reduces the mechanical mismatch of the interface could prolong survival of the experimental preparation [271]. Moreover, the stimulation intensity, frequency, and duty cycle in this study was applied weekly, which is mild compared to the ideal application condition where electrical stimulations may be required 24 hours a day. To determine if PC shows continuous stimulation benefit compared to IrOx coated electrodes, more aggressive *in vivo* experiments should be performed. Also, while we have demonstrated PC to be a more efficient stimulating materials, results of this study do not provide a clear answer for if and how the increased efficiency translate to changes in neural functions and rehabilitation. Additional investigations of electrical stimulation efficiency should pair *in vivo* imaging with behavior for a more comprehensive evaluation. Finally, our study was limited to observing the activities of neural elements only with no additional histological analysis (due to complications with extracting the probes). To further understand the stimulating

interface, additional labels should be used for the behavior for non-neuronal cells such as microglia, astrocytes, oligodendrocytes and pericytes, in conjunction with neural element labels.

4.6 Conclusion

Modern imaging techniques and transgenic tools enable observations of neural dynamics to electrical stimulations in real time. Herein, we chronically stimulated the cortex of GCaMP6s mice using two high-charge-injection materials, PC and IrOx, up to 12 weeks. We observed an initial decline in stimulation efficiency in terms of integrated GCaMP intensity and radius per unit stimulation amplitude. This was followed by a trend of recovery in GCaMP intensity at week 4. Additionally, PC coated electrodes showed significantly higher efficiency in activating GCaMP compared to IrOx coated electrodes overall but not during the initial ~ 2 weeks after implantation. This is likely due to the atrophying axons and neurites preventing the recruitment of distant neural elements during this time. Using TPM, we evaluated the excitability of neural elements within 50 μm of the electrode and observed a qualitative increase in the rheobase over 7 weeks, indicating decreased excitability within the first 50 μm of the electrode center. Spontaneous electrophysiology showed a significant decline in neural spike unit count and amplitude over time for both materials. Meanwhile, *in vivo* electrochemical data showed fluctuations within the twelve-week period with moderate increases in impedance up to week 8, significant decreases in CSCc, and moderate increases in energy consumption for stimulating electrodes of both materials over time. PC coated electrodes had significantly lower impedance and delivered energy compared to IrOx coated electrodes. We performed equivalent circuit modeling to further understand the stimulating interface and concluded that the larger pores from the nano-fibrous topography of the

PC coating made it more susceptible to dramatic changes in electrolyte resistance within the coating to electrical stimulation compared to IrOx coated electrodes. Furthermore, we observed abnormal cortical responses to stimulations within the charge injection limit of both electrode materials in a subset of chronically surviving mice, providing new evidence for the potential adverse effects of widely used intracortical stimulation paradigms. Results from this study not only revealed the dynamic changes to stimulation efficiency after implantation, but also reiterates the tremendous potential for PC to be used for high efficiency chronic stimulations in neuromodulation.

5.0 Conclusion

5.1 Summary of Research Findings

This dissertation investigates the stimulation efficiency of high-performing electrode materials, PEDOT/CNT (PC) and iridium oxide (IrOx). Using *in vivo* imaging and transgenic tools, we visualized neuronal responses to electrical stimulation in real time. Results from this work provided additional evidence in supporting the use of PC as an efficient and stable material for chronic electrical stimulation.

Chapters 2 and 3 of the dissertation focused on investigating the efficiency of the two stimulation materials. We observed significantly higher and broader neural activation by PC coated electrodes compared to IrOx coated electrodes. This observation was highly likely due to (1) the nano-fibrous surface topography of PC electrodes, creating a more non-uniform electric field compared to IrOx electrodes thereby increasing the activating function of nearby neural elements, and (2) the fractal nature of the PC coating creates a better integration of neural tissue than the smoother IrOx coating. The improved electrode-tissue integration may reduce additional extracellular fluid buildup, which could shunt the injected current, requiring higher charge injection. In addition, we observed that microelectrode arrays with multiple shanks recruit a wider region of the cortex compared to single shank arrays. This may be associated with the larger implant footprint which severs additional axon, increasing network excitability evident in mild traumatic brain injury literatures. Moreover, *in vivo* imaging of GCaMP response upon electrical stimulation were performed 24h post electrode implantation, allowing us to study the *in vivo* electrode performance without the interference of glial scarring. Furthermore, we investigated the

effect of stimulation modality on neural activation. With voltage-controlled stimulation, PC coated electrodes activate significantly more neural tissue than IrOx due to the lower impedance and the consequent higher injected current. With current-controlled stimulation, we observed higher soma recruitment from PC sites than IrOx sites, likely owing to its more intimate connection to neural tissue and increased non-uniform voltage field immediately nearby the electrode. Lastly, for both materials, we observed more spatially distinct neuronal activation with shorter pulse widths. The findings of this work contribute to our understanding of cortical microstimulation using novel materials; by using *in vivo* imaging in awake mice, we mimic conditions in human studies while directly visualized the region of activated neural tissue.

In Chapter 4, we described our results from longitudinal investigation of stimulation stability and safety. We chronically stimulated the cortex of GCaMP6s mice using electrodes coated with PC and IrOx, for up to 12 weeks. We observed an initial decline in stimulation efficiency in terms of integrated GCaMP intensity and radius per unit stimulation amplitude. This was followed by a trend of recovery in GCaMP intensity at week 4. Additionally, PC coated electrodes showed significantly higher efficiency in activating GCaMP compared to IrOx coated electrodes overall but not during the initial ~ 2 weeks after implantation. This is likely due to the atrophying axons and neurites preventing the recruitment of distant neural elements during this time. Using TPM, we evaluated the excitability of neural elements within 50 μm of the electrode and observed a qualitative increase in the rheobase over 7 weeks, indicating decreased excitability within the first 50 μm of the electrode center. Spontaneous electrophysiology showed a significant decline in neural spike unit count and amplitude over time for both materials. Meanwhile, *in vivo* electrochemical data showed fluctuations within the twelve-week period with moderate increases in impedance up to week 8, significant decreases in CSCc, and moderate increases in energy

consumption for stimulating electrodes of both materials over time. PC coated electrodes had significantly lower impedance and delivered energy compared to IrOx coated electrodes. We performed equivalent circuit modeling to further understand the stimulating interface and concluded that the larger pores from the nano-fibrous topography of the PC coating made it more susceptible to dramatic changes in electrolyte resistance within the coating to electrical stimulation compared to IrOx coated electrodes. Furthermore, we observed abnormal cortical responses to stimulations within the charge injection limit of both electrode materials in a subset of chronically surviving mice, providing new evidence for the potential adverse effects of widely used intracortical stimulation paradigms. Results from this study not only revealed the dynamic changes to stimulation efficiency after implantation, but also reiterates the tremendous potential for PC to be used for high efficiency chronic stimulations in neuromodulation.

5.2 Future Directions

Chronically stable stimulating neural interfaces require a coordinated effort from an interdisciplinary team of neuroscientists, material scientists and engineers. Despite improved charge injection limit in novel metal/metal oxides, conducting polymers, and carbon-based materials, devices made from these materials still face challenges similar to those encountered by recording electrodes. In stimulating devices, it is imperative to ensure insulation integrity, electrode coating adhesion, and mechanical stability of connectors to external data acquisition units. Numerous existing technologies could be combined to solve issues of foreign body responses and oxidative stress as a result of implantation. Surface modification with bioactive and biomimetic molecules such as neural adhesion molecules L1, anti-inflammatory peptides, super

hydrophilic coatings and superoxide dismutase or delivery of antioxidant and anti-inflammatory drugs have shown to reduce microglia activation,[250] neuronal death,[259] astrocytic scars,[259] improve axonal regrowth,[259] and reduce the generation of ROS at the vicinity of the implants.[105] While more neural electrodes are fabricated with subcellular dimensions and ultra-flexibility, investigations of microstimulation efficacy and stability on these devices need to be done.[271] Finally, we should use advanced genetic and imaging tools to understand the effects of electrical stimulation on both neuronal [117]and non-neuronal cells in order to understand the mechanism of electrical stimulation and optimize stimulation parameters for different applications. As with all newly developed medical devices, the road to clinical translation will be long. We must be aware of the regulatory process [272, 273] and be in compliance with the FDA guidelines to ensure ultimate safety from a material perspective and the design of safe stimulation paradigms.

5.2.1 Directions for the Use of Biomimetic Coatings for Improving Stimulation Stability

In chapter 4, we saw that the benefit of the PC coating diminished in the acute period of the implantation and this was likely caused by the acute injury as a result of the electrode implantation. During this period, axons that were mechanically severed undergo atrophy and degeneration. Meanwhile, immune cells secrete pro-inflammatory cytokines that can lead to additional neuronal death. These severe foreign body responses may be alleviated by the use of biological and chemical surface coatings.

5.2.1.1 Neural Adhesion Molecule L1

L1 is a neural-adhesion protein which is expressed in most neurons in the CNS and targeted on the surface of neurites and growth cones during development. It is known to mediate neurite outgrowth, adhesion, fasciculation, and neurite guidance and neuronal migration and survival even in the presence of astrocytes and fibroblasts[274-276]. Our laboratory has successfully immobilized the L1 protein on the surface of indwelling neural probes such as the Michigan silicon electrodes, and the Utah array[259, 276]. The immobilized L1 on the implanted probes has significantly improved device-tissue integration through the reduction of activated microglia and astrocyte attachment, and the increase in neurite outgrowth immediately adjacent to the device[277]. We hypothesize that L1 coated electrodes will reduce the threshold of activation of neural elements compared to uncoated electrodes by increasing neurite outgrowth and decreasing microglia attachment. The decrease in microglia attachment and increase the density in excitable neuronal elements shorten the distance between the current source and the excitable tissue, thereby reducing the amount of charge needed to activate the tissue. This hypothesis could be tested by implanting L1 coated and uncoated electrodes into the somatosensory cortex of thy1-GCaMP transgenic mice and applying clinically relevant stimulation parameters. The results from these experiments will allow us to observe in real time the effect of L1 coating on the neural adhesion and neurite regeneration around the implant and the excitability of the regenerated neural elements.

5.2.1.2 Superoxide Dismutase Mimic

The implantation of an electrode into the brain triggers an inflammatory response which initiates the activation of microglia/macrophage. Consequently, the activated microglia/macrophages secrete pro-inflammatory cytokines, initiate the recruitment of additional microglia/macrophages, and produce various cytotoxic factors like the reactive oxygen species

(ROS). The presence of ROS increases the likelihood of neurodegeneration, as in the cases of many neurological disorders [278, 279]. In addition, electrochemical products as a result of faradaic charge injection have been reported to increase ROS which can severely damage myelin, negatively affecting axonal signal transduction [48, 49] [50, 52]. The ROS generated as a result of electrode implantation or potentially unsafe electrical stimulation may be mediated by the use of a superoxide dismutase enzyme (SOD). In our previous reports, we have synthesized a SOD mimic (iSODm) to covalently attach to the neural probe surfaces. This coating showed a high catalytic superoxide scavenging activity. After 1 week of implantation *in vivo*, iSODm coated electrodes showed significantly lower expression of markers for oxidative stress immediately adjacent to the electrode surface and significantly less neurons undergoing apoptosis[280]. When immobilized on the surfaces of stimulating electrodes, the iSODm coating may improve the acute stimulation stability.

5.2.2 Directions for Further Understanding Stimulation Safety

This dissertation focused on investigating the efficiency and stability of microelectrodes coated with PC and IrOx. Another crucial aspect of stable electrical stimulation is deeper understanding on stimulation safety. Previously established safety limits do not take into account the differences in stimulation waveform, pulse width, frequency, and duty cycle, and they often do not apply to microstimulation. This motivates additional studies to expand on our understanding of microstimulation safety. As introduced in Chapter 1, biological damages as a result of electrical stimulation can manifest in electroporation, electrochemical reactions that lead to local pH changes[281], mechanical and chemical effects of gas evolution[118], toxicity of degraded electrode materials, and excitotoxicity as a result of high frequency stimulation. Using transgenic

mouse lines, we can characterize the functional and behavioral response of neurons and non-neuronal cells such as microglia in response to stimulation that exceeds the limit defined by traditional research. Neuronal cell membrane integrity can be assessed using propidium iodide (PI membrane permeability indicator) in conjunction with GCaMP which will give us information of neurons with damaged membranes. Similarly, PI can also be used to indicate membrane permeability for microglia cells, combined with our understanding of microglia behavior[162], we can gain additional understanding on unsafe electrical stimulation. Furthermore, previous research has shown BBB leakage with direct current electrical stimulation[282], we can also use imaging tools and vascular dyes to study BBB integrity associated with safe and unsafe electrical stimulation.

Appendix A Other Significant Contributions

Manuscripts

X.S.Zheng, Qianru Yang, Alberto Vasquez, Tracy Cui, Multimodal investigation of chronic microstimulation stability using PEDOT/CNT and Iridium oxide, 2021, in prep.

X.S Zheng, Chao Tan, Elisa Castgnola, Tracy Cui, Microelectrode materials for chronic electrical microstimulation, *Advanced Healthcare Materials*, 2021, submitted.

X.S.Zheng, Qianru Yang, Alberto Vasquez, Tracy Cui, Imaging the efficiency of PEDOT/CNT and iridium oxide electrode coatings for microstimulation, *Advances in Nano Biomed Research*, 2021, revised.

X.S. Zheng, A.Y. Griffith, E. Chang, M.J. Looker, L.E. Fisher, B. Clapsaddle, X.T. Cui, *Evaluation of a conducting elastomeric composite material for intramuscular electrode application, Acta Biomaterialia* 103 (2020) 81-91.

X.S. Zheng, A.Y. Griffith, E. Chang, M.J. Looker, L.E. Fisher, B. Clapsaddle, X.T. Cui, *Evaluation of a conducting elastomeric composite material for intramuscular electrode application, Acta Biomaterialia* 103 (2020) 81-91.

X.S. Zheng*, N.R. Snyder*, K. Woeppel*, J.H. Barengo, X. Li, J. Eles, C.L. Kolarcik, X.T. Cui, *A superoxide scavenging coating for improving tissue response to neural implants, Acta Biomaterialia* 99 (2019) 72-83.

X. Zheng, K.M. Woeppel, A.Y. Griffith, E. Chang, M.J. Looker, L.E. Fisher, B.J. Clapsaddle, X.T. Cui, *Soft Conducting Elastomer for Peripheral Nerve Interface, Advanced Healthcare Materials* 8(9) (2019) 1801311.

K.M. Woepfel, **X.S. Zheng**, Z.M. Schulte, N.L. Rosi, X.T. Cui, Nanoparticle Doped PEDOT for *Enhanced Electrode Coatings and Drug Delivery*, *Advanced Healthcare Materials* 8(21) (2019) 1900622.

K.M. Woepfel, **X.S. Zheng**, X.T. Cui. *Enhancing surface immobilization of bioactive molecules via a silica nanoparticle-based coating*, *J Mater Chem B* 6(19) (2018).

Z.J. Du, C.L. Kolarcik, T.D.Y. Kozai, S.D. Luebben, S.A. Sapp, **X.S. Zheng**, J.A. Nabity, X.T. Cui, *Ultrasoft microwire neural electrodes improve chronic tissue integration*, *Acta Biomaterialia* 53 (2017) 46-58.

Book Chapter

Elisa Castagnola, **X. Sally Zheng** and X. Tracy Cui. *Flexible and soft material and devices for neural interface*. Springer Handbook of Neuroengineering, Nithish Thankor, accepted

Presentations (national/international conferences)

X. Sally Zheng, Q. Yang, A. Vazquez, T. Cui. *Investigation of the efficiency, stability, and safety of intracortical microstimulation with AIROF and PEDOT/CNT microelectrodes using in vivo imaging*. Gordon Research Conference, Neuroelectronic Interfaces, March 2020, Ventura, CA (cancelled due to COVID-19).

X. Sally Zheng, Q. Yang, A. Vazquez, T. Cui. *In vivo characterization of the stability of cortical response to electrical microstimulation*. Program No. 314.16. 2019 Neuroscience Meeting Planner. Chicago, IL: Society for Neuroscience, 2019. Online.

X. Sally Zheng, Azante Griffith, Kevin Woepfel, Emily Chang, Michael Looker, Brady Clapsaddle, Lee Fisher, Tracy Cui, PhD *Improvement of chronic device-tissue integration with*

elastic PEDOT/CNT based intra-neural electrodes. Minneapolis, MN, Neural Interfaces Conference, 2018

X.S. Zheng, K. M. Woeppel, M. J. Looker, E. Chang, B. Clapsaddle, A. M. Aral, V. Gorantla, L. E. Fisher, X. T. Cui; *Soft and elastomeric electrodes for muscle and nerve interfaces*, 595.13/kk16. Neuroscience Meeting Planner. Washington, DC: Society for Neuroscience, 2017. Online.

X. S Zheng, X.T. Cui; *Functional evaluation of a superoxide dismutase mimic coating for chronically implanted neural electrodes* 438.05/WW3 Neuroscience Meeting Planner. San Diego, CA: Society for Neuroscience, 2016. Online.

K Woeppel, **S Zheng**, B Clapsaddle, M Looker, L Fisher, T Cui. (2017) “*Conductive Elastomeric Electrodes for Interfacing with Peripheral Nervous System*”, Materials Research Society Oral Presentation

K Woeppel, **S Zheng**, T Cui, (2019) “*Nanoparticle Dopants Enhance Electrically Controlled Drug Release from Conducting Polymer Coatings*”, Society for Biomaterials Oral Presentation

J Eles, **X Zheng**, P Prabhu, XT Cui *Carbon Nanotube/Conducting Polymer Coatings for Electrically Stimulated Drug Release from intramuscular electrodes* Biomedical Engineering Society Annual Meeting, FL, 2015

W McFadden, **X Zheng**, V Erbas, V Gorantla, X Cui, TDY Kozai, *Fabricating and Evaluation of Carbon Fiber Microelectrodes for Muscle Stimulation* Biomedical Engineering Society Annual Meeting, FL, 2015

Bibliography

- [1] J.S. Yeomans, P.W. Frankland, The acoustic startle reflex: neurons and connections, *Brain research reviews* 21(3) (1995) 301-314.
- [2] E.J. Tehovnik, W.M. Slocum, P.H. Schiller, Microstimulation of V1 delays the execution of visually guided saccades, *European Journal of Neuroscience* 20(1) (2004) 264-272.
- [3] P.L. Strick, J.B. Preston, Multiple representation in the primate motor cortex, *Brain research* 154(2) (1978) 366-370.
- [4] E. Schmidt, M. Bak, F. Hambrecht, C. Kufta, D. O'rourke, P. Vallabhanath, Feasibility of a visual prosthesis for the blind based on intracortical micro stimulation of the visual cortex, *Brain* 119(2) (1996) 507-522.
- [5] D. McCreery, T. Yuen, L. Bullara, Chronic microstimulation in the feline ventral cochlear nucleus: physiologic and histologic effects, *Hearing Research* 149(1-2) (2000) 223-238.
- [6] V.K. Mushahwar, D.M. Gillard, M.J. Gauthier, A. Prochazka, Intraspinal micro stimulation generates locomotor-like and feedback-controlled movements, *IEEE Transactions on Neural Systems and Rehabilitation Engineering* 10(1) (2002) 68-81.
- [7] S.N. Flesher, J.L. Collinger, S.T. Foldes, J.M. Weiss, J.E. Downey, E.C. Tyler-Kabara, S.J. Bensmaia, A.B. Schwartz, M.L. Boninger, R.A. Gaunt, Intracortical microstimulation of human somatosensory cortex, *Science translational medicine* 8(361) (2016) 361ra141-361ra141.
- [8] R. Rogers, G. Hermann, Gastric-vagal solitary neurons excited by paraventricular nucleus microstimulation, *Journal of the autonomic nervous system* 14(4) (1985) 351-362.
- [9] J. Guo, H. Jin, Z. Shi, J. Yin, T. Pasricha, J.D. Chen, Sacral nerve stimulation improves colonic inflammation mediated by autonomic-inflammatory cytokine mechanism in rats, *Neurogastroenterology & Motility* 31(10) (2019) e13676.
- [10] Global Neuromodulation Market Size study, by Technology (Internal Neuromodulation, External Neuromodulation), by Application (Parkinson's Disease, Epilepsy, Depression, Dystonia, Pain Management, Others) and Regional Forecasts 2020-2027, 2020, p. 200.

- [11] S.K. Kelly, D.B. Shire, J. Chen, P. Doyle, M.D. Gingerich, S.F. Cogan, W.A. Drohan, S. Behan, L. Theogarajan, J.L. Wyatt, J.F. Rizzo, 3rd, A hermetic wireless subretinal neurostimulator for vision prostheses, *IEEE transactions on bio-medical engineering* 58(11) (2011) 3197-3205.
- [12] S.F. Cogan, Neural Stimulation and Recording Electrodes, *Annual Review of Biomedical Engineering* 10(1) (2008) 275-309.
- [13] S. Arcot Desai, C.A. Gutekunst, S.M. Potter, R.E. Gross, Deep brain stimulation macroelectrodes compared to multiple microelectrodes in rat hippocampus, *Front Neuroeng* 7 (2014) 16.
- [14] J. Weiland, W. Fink, M. Humayun, W. Liu, D. Rodger, Y.C. Tai, M. Tarbell, Progress towards a high-resolution retinal prosthesis, *Conf Proc IEEE Eng Med Biol Soc 2005* (2005) 7373-5.
- [15] S.F. Cogan, J. Ehrlich, T.D. Plante, A. Smirnov, D.B. Shire, M. Gingerich, J.F. Rizzo, Sputtered iridium oxide films for neural stimulation electrodes, *Journal of Biomedical Materials Research Part B: Applied Biomaterials* 89B(2) (2009) 353-361.
- [16] S.F. Cogan, P.R. Troyk, J. Ehrlich, T.D. Plante, D.E. Detlefsen, Potential-biased, asymmetric waveforms for charge-injection with activated iridium oxide (AIROF) neural stimulation electrodes, *IEEE Transactions on Biomedical Engineering* 53(2) (2006) 327-332.
- [17] J.D. Weiland, D.J. Anderson, M.S. Humayun, In vitro electrical properties for iridium oxide versus titanium nitride stimulating electrodes, *IEEE transactions on biomedical engineering* 49(12) (2002) 1574-1579.
- [18] S. Nimbalkar, E. Castagnola, A. Balasubramani, A. Scarpellini, S. Samejima, A. Khorasani, A. Boissenin, S. Thongpang, C. Moritz, S. Kassegne, Ultra-capacitive carbon neural probe allows simultaneous long-term electrical stimulations and high-resolution neurotransmitter detection, *Scientific reports* 8(1) (2018) 1-14.
- [19] C. Boehler, D.M. Vieira, U. Egert, M. Asplund, NanoPt—A Nanostructured Electrode Coating for Neural Recording and Microstimulation, *ACS Applied Materials & Interfaces* 12(13) (2020) 14855-14865.
- [20] Z. Aqrawe, J. Montgomery, J. Travas-Sejdic, D. Svirskis, Conducting polymers for neuronal microelectrode array recording and stimulation, *Sensors and Actuators B: Chemical* 257 (2018) 753-765.

- [21] S.J. Wilks, S.M. Richardson-Burn, J.L. Hendricks, D. Martin, K.J. Otto, Poly (3, 4-ethylene dioxithiophene)(PEDOT) as a micro-neural interface material for electrostimulation, *Frontiers in neuroengineering* 2 (2009) 7.
- [22] X.T. Cui, D.D. Zhou, Poly (3,4-ethylenedioxythiophene) for chronic neural stimulation, *IEEE Trans Neural Syst Rehabil Eng* 15(4) (2007) 502-8.
- [23] X. Luo, C.L. Weaver, D.D. Zhou, R. Greenberg, X.T. Cui, Highly stable carbon nanotube doped poly (3, 4-ethylenedioxythiophene) for chronic neural stimulation, *Biomaterials* 32(24) (2011) 5551-5557.
- [24] C.L. Kolarcik, K. Catt, E. Rost, I.N. Albrecht, D. Bourbeau, Z. Du, T.D.Y. Kozai, X. Luo, D.J. Weber, X. Tracy Cui, Evaluation of poly(3,4-ethylenedioxythiophene)/carbon nanotube neural electrode coatings for stimulation in the dorsal root ganglion, *Journal of Neural Engineering* 12(1) (2014) 016008.
- [25] Q. Zeng, K. Xia, B. Sun, Y. Yin, T. Wu, M.S. Humayun, Electrodeposited iridium oxide on platinum nanocones for improving neural stimulation microelectrodes, *Electrochimica Acta* 237 (2017) 152-159.
- [26] S. Fierro, A. Kapalka, C. Comninellis, Electrochemical comparison between IrO₂ prepared by thermal treatment of iridium metal and IrO₂ prepared by thermal decomposition of H₂IrCl₆ solution, *Electrochemistry communications* 12(1) (2010) 172-174.
- [27] A. Ansaldo, E. Castagnola, E. Maggiolini, L. Fadiga, D. Ricci, Superior electrochemical performance of carbon nanotubes directly grown on sharp microelectrodes, *ACS nano* 5(3) (2011) 2206-2214.
- [28] Y. Lu, H. Lyu, A.G. Richardson, T.H. Lucas, D. Kuzum, Flexible neural electrode array based-on porous graphene for cortical microstimulation and sensing, *Scientific reports* 6 (2016) 33526.
- [29] S. Zhao, G. Li, C. Tong, W. Chen, P. Wang, J. Dai, X. Fu, Z. Xu, X. Liu, L. Lu, Full activation pattern mapping by simultaneous deep brain stimulation and fMRI with graphene fiber electrodes, *Nature communications* 11(1) (2020) 1-12.
- [30] A.J. Bullard, B.C. Hutchison, J. Lee, C.A. Chestek, P.G. Patil, Estimating risk for future intracranial, fully implanted, modular neuroprosthetic systems: a systematic review of hardware complications in clinical deep brain stimulation and experimental human intracortical arrays, *Neuromodulation: Technology at the Neural Interface* 23(4) (2020) 411-426.

- [31] J.W. Salatino, K.A. Ludwig, T.D.Y. Kozai, E.K. Purcell, Glial responses to implanted electrodes in the brain, *Nature Biomedical Engineering* 1(11) (2017) 862-877.
- [32] V.S. Polikov, P.A. Tresco, W.M. Reichert, Response of brain tissue to chronically implanted neural electrodes, *Journal of Neuroscience Methods* 148(1) (2005) 1-18.
- [33] T.D. Kozai, Z. Gugel, X. Li, P.J. Gilgunn, R. Khilwani, O.B. Ozdoganlar, G.K. Fedder, D.J. Weber, X.T. Cui, Chronic tissue response to carboxymethyl cellulose based dissolvable insertion needle for ultra-small neural probes, *Biomaterials* 35(34) (2014) 9255-9268.
- [34] T.D.Y. Kozai, A.L. Vazquez, C.L. Weaver, S.-G. Kim, X.T. Cui, In vivo two-photon microscopy reveals immediate microglial reaction to implantation of microelectrode through extension of processes, *Journal of neural engineering* 9(6) (2012) 066001.
- [35] D.R. Merrill, M. Bikson, J.G. Jefferys, Electrical stimulation of excitable tissue: design of efficacious and safe protocols, *Journal of neuroscience methods* 141(2) (2005) 171-198.
- [36] S.H. Wright, Generation of resting membrane potential, *Advances in physiology education* 28(4) (2004) 139-142.
- [37] M.H. Kole, G.J. Stuart, Is action potential threshold lowest in the axon?, *Nature neuroscience* 11(11) (2008) 1253-1255.
- [38] H. Yuk, B. Lu, X. Zhao, Hydrogel bioelectronics, *Chemical Society Reviews* 48(6) (2019) 1642-1667.
- [39] D.C. Martin, G.G. Malliaras, Interfacing electronic and ionic charge transport in bioelectronics, *ChemElectroChem* 3(5) (2016) 686-688.
- [40] S.F. Cogan, K.A. Ludwig, C.G. Welle, P. Takmakov, Tissue damage thresholds during therapeutic electrical stimulation, *J Neural Eng* 13(2) (2016) 021001.
- [41] T.L. Rose, L.S. Robblee, Electrical stimulation with Pt electrodes. VIII. Electrochemically safe charge injection limits with 0.2 ms pulses (neuronal application), *IEEE Transactions on Biomedical Engineering* 37(11) (1990) 1118-1120.

- [42] M. Mahadevappa, J.D. Weiland, D. Yanai, I. Fine, R.J. Greenberg, M.S. Humayun, Perceptual thresholds and electrode impedance in three retinal prosthesis subjects, *IEEE Transactions on Neural Systems and Rehabilitation Engineering* 13(2) (2005) 201-206.
- [43] J.F. Rizzo, J. Wyatt, J. Loewenstein, S. Kelly, D. Shire, Perceptual efficacy of electrical stimulation of human retina with a microelectrode array during short-term surgical trials, *Investigative ophthalmology & visual science* 44(12) (2003) 5362-5369.
- [44] F. Hambrecht, Visual prostheses based on direct interfaces with the visual system, *Bailliere's clinical neurology* 4(1) (1995) 147.
- [45] R.H. Pudenz, L. Bullara, D. Dru, A. Talalla, Electrical stimulation of the brain. II. Effects on the blood-brain barrier, *Surgical neurology* 4(2) (1975) 265-270.
- [46] R. Pudenz, L.A. Bullara, S. Jacques, F. Hambrecht, Electrical stimulation of the brain. III. The neural damage model, *Surgical Neurology* 4(4) (1975) 389-400.
- [47] J.T. Mortimer, C.N. Shealy, C. Wheeler, Experimental nondestructive electrical stimulation of the brain and spinal cord, *Journal of neurosurgery* 32(5) (1970) 553-559.
- [48] P.H. Chan, M. Yurko, R.A. Fishman, Phospholipid degradation and cellular edema induced by free radicals in brain cortical slices, *Journal of neurochemistry* 38(2) (1982) 525-531.
- [49] G.R. Buettner, The Pecking Order of Free Radicals and Antioxidants: Lipid Peroxidation, - Tocopherol, and Ascorbate, *Archives of biochemistry and biophysics* 300(2) (1993) 535-543.
- [50] L. Chia, J. Thompson, M. Moscarello, Disorder in human myelin induced by superoxide radical: an in vitro investigation, *Biochemical and biophysical research communications* 117(1) (1983) 141-146.
- [51] C. Griot, M. Vandeveld, A. Richard, E. Peterhans, Selective degeneration of oligodendrocytes mediated by reactive oxygen species, *Free radical research communications* 11(4-5) (1990) 181-193.
- [52] G.W. Konat, R.C. Wiggins, Effect of reactive oxygen species on myelin membrane proteins, *Journal of neurochemistry* 45(4) (1985) 1113-1118.

- [53] A. Sevanian, Lipid peroxidation, membrane damage, and phospholipase A2 action, Cellular antioxidant defense mechanisms, CRC Press Boca Raton, FL1988, pp. 78-95.
- [54] D.B. McCreery, T.G. Yuen, W.F. Agnew, L.A. Bullara, A characterization of the effects on neuronal excitability due to prolonged microstimulation with chronically implanted microelectrodes, *IEEE Trans Biomed Eng* 44(10) (1997) 931-9.
- [55] S. Ohayon, P. Grimaldi, N. Schweers, D.Y. Tsao, Saccade modulation by optical and electrical stimulation in the macaque frontal eye field, *J Neurosci* 33(42) (2013) 16684-16697.
- [56] A.M. Ni, J.H. Maunsell, Microstimulation reveals limits in detecting different signals from a local cortical region, *Current Biology* 20(9) (2010) 824-828.
- [57] R. Vallejo, A. Gupta, C.A. Kelley, A. Vallejo, J. Rink, J.M. Williams, C.L. Cass, W.J. Smith, R. Benyamin, D.L. Cedeño, Effects of Phase Polarity and Charge Balance Spinal Cord Stimulation on Behavior and Gene Expression in a Rat Model of Neuropathic Pain, *Neuromodulation* 23(1) (2020) 26-35.
- [58] P.J. Rousche, R.A. Normann, Chronic intracortical microstimulation (ICMS) of cat sensory cortex using the Utah Intracortical Electrode Array, *IEEE transactions on rehabilitation engineering* 7(1) (1999) 56-68.
- [59] J.R. Bartlett, R.W. Doty sr, B.B. Lee, N. Negrão, W.H. Overman jr, Deleterious effects of prolonged electrical excitation of striate cortex in macaques, *Brain, behavior and evolution* 14(1-2) (1977) 46-66.
- [60] S.A. Chowdhury, G.C. DeAngelis, Fine discrimination training alters the causal contribution of macaque area MT to depth perception, *Neuron* 60(2) (2008) 367-377.
- [61] C.-T. Law, J.I. Gold, Reinforcement learning can account for associative and perceptual learning on a visual-decision task, *Nature neuroscience* 12(5) (2009) 655.
- [62] D. McCreery, V. Píkov, P.R. Troyk, Neuronal loss due to prolonged controlled-current stimulation with chronically implanted microelectrodes in the cat cerebral cortex, *Journal of neural engineering* 7(3) (2010) 036005.
- [63] A.T. Rajan, J.L. Boback, J.F. Dammann, F.V. Tenore, B.A. Wester, K.J. Otto, R.A. Gaunt, S.J. Bensmaia, The effects of chronic intracortical microstimulation on neural tissue and fine motor behavior, *Journal of neural engineering* 12(6) (2015) 066018.

- [64] T.D. Kozai, K. Catt, X. Li, Z.V. Gugel, V.T. Olafsson, A.L. Vazquez, X.T. Cui, Mechanical failure modes of chronically implanted planar silicon-based neural probes for laminar recording, *Biomaterials* 37 (2015) 25-39.
- [65] A. Prasad, Q.-S. Xue, V. Sankar, T. Nishida, G. Shaw, W.J. Streit, J.C. Sanchez, Comprehensive characterization and failure modes of tungsten microwire arrays in chronic neural implants, *Journal of neural engineering* 9(5) (2012) 056015.
- [66] R. Caldwell, M.G. Street, R. Sharma, P. Takmakov, B. Baker, L. Rieth, Characterization of Parylene-C degradation mechanisms: In vitro reactive accelerated aging model compared to multiyear in vivo implantation, *Biomaterials* 232 (2020) 119731.
- [67] G. Schmitt, F. Faßbender, H. Lüth, M.J. Schöning, J.W. Schultze, G. Buß, Passivation and corrosion of microelectrode arrays, *Materials and Corrosion* 51(1) (2000) 20-25.
- [68] J. Aceros, M. Yin, D.A. Borton, W.R. Patterson, C. Bull, A.V. Nurmikko, Polymeric packaging for fully implantable wireless neural microsensors, 2012 Annual International Conference of the IEEE Engineering in Medicine and Biology Society, IEEE, 2012, pp. 743-746.
- [69] A. Vanhoestenbergh, N. Donaldson, Corrosion of silicon integrated circuits and lifetime predictions in implantable electronic devices, *Journal of neural engineering* 10(3) (2013) 031002.
- [70] A. Prasad, Q.-S. Xue, R. Dieme, V. Sankar, R. Mayrand, T. Nishida, W.J. Streit, J.C. Sanchez, Abiotic-biotic characterization of Pt/Ir microelectrode arrays in chronic implants, *Frontiers in neuroengineering* 7 (2014) 2.
- [71] L.A. Geddes, R. Roeder, Criteria for the selection of materials for implanted electrodes, *Annals of biomedical engineering* 31(7) (2003) 879-890.
- [72] R.L. White, T.J. Gross, An Evaluation of the Resistance to Electrolysis of Metals for Use in Biostimulation Microprobes, *IEEE Transactions on Biomedical Engineering* BME-21(6) (1974) 487-490.
- [73] S.F. Cogan, T. Plante, J. Ehrlich, Sputtered iridium oxide films (SIROFs) for low-impedance neural stimulation and recording electrodes, The 26th Annual International Conference of the IEEE Engineering in Medicine and Biology Society, IEEE, 2004, pp. 4153-4156.

[74] R. Green, P. Matteucci, R. Hassarati, B. Giraud, C. Dodds, S. Chen, P. Byrnes-Preston, G. Suaning, L. Poole-Warren, N. Lovell, Performance of conducting polymer electrodes for stimulating neuroprosthetics, *Journal of neural engineering* 10(1) (2013) 016009.

[75] Q. Huang, Q. Luo, Z. Chen, L. Yao, P. Fu, Z. Lin, The effect of electrolyte concentration on electrochemical impedance for evaluating polysulfone membranes, *Environmental Science: Water Research & Technology* 4(8) (2018) 1145-1151.

[76] C.J. Meunier, J.D. Denison, G.S. McCarty, L.A. Sombers, Interpreting Dynamic Interfacial Changes at Carbon Fiber Microelectrodes Using Electrochemical Impedance Spectroscopy, *Langmuir* (2020).

[77] Y. Lu, Z. Cai, Y. Cao, H. Yang, Y.Y. Duan, Activated iridium oxide films fabricated by asymmetric pulses for electrical neural microstimulation and recording, *Electrochemistry communications* 10(5) (2008) 778-782.

[78] H. Zhou, X. Cheng, L. Rao, T. Li, Y.Y. Duan, Poly (3, 4-ethylenedioxythiophene)/multiwall carbon nanotube composite coatings for improving the stability of microelectrodes in neural prostheses applications, *Acta biomaterialia* 9(5) (2013) 6439-6449.

[79] M. Vomero, A. Oliveira, D. Ashouri, M. Eickenscheidt, T. Stieglitz, Graphitic Carbon Electrodes on Flexible Substrate for Neural Applications Entirely Fabricated Using Infrared Nanosecond Laser Technology, *Scientific Reports* 8(1) (2018) 14749.

[80] S. Negi, R. Bhandari, L. Rieth, R. Van Wagenen, F. Solzbacher, Neural electrode degradation from continuous electrical stimulation: Comparison of sputtered and activated iridium oxide, *Journal of Neuroscience Methods* 186(1) (2010) 8-17.

[81] T. Geninatti, G. Bruno, B. Barile, R.L. Hood, M. Farina, J. Schmulen, G. Canavese, A. Grattoni, Impedance characterization, degradation, and in vitro biocompatibility for platinum electrodes on BioMEMS, *Biomedical microdevices* 17(1) (2015) 24.

[82] Standard Test Methods for Rating Adhesion by Tape Test.

[83] J.A. Goding, A.D. Gilmour, P.J. Martens, L.A. Poole-Warren, R.A. Green, Small bioactive molecules as dual functional co-dopants for conducting polymers, *Journal of Materials Chemistry B* 3(25) (2015) 5058-5069.

- [84] E. Castagnola, S. Carli, M. Vomero, A. Scarpellini, M. Prato, N. Goshi, L. Fadiga, S. Kassegne, D. Ricci, Multilayer poly(3,4-ethylenedioxythiophene)-dexamethasone and poly(3,4-ethylenedioxythiophene)-polystyrene sulfonate-carbon nanotubes coatings on glassy carbon microelectrode arrays for controlled drug release, *Biointerphases* 12(3) (2017) 031002.
- [85] S. Duan, L. Zhang, Z. Wang, C. Li, One-step rod coating of high-performance silver nanowire–PEDOT:PSS flexible electrodes with enhanced adhesion after sulfuric acid post-treatment, *RSC Advances* 5(115) (2015) 95280-95286.
- [86] E. Castagnola, L. Maiolo, E. Maggiolini, A. Minotti, M. Marrani, F. Maita, A. Pecora, G.N. Angotzi, A. Ansaldo, M. Boffini, L. Fadiga, G. Fortunato, D. Ricci, PEDOT-CNT-Coated Low-Impedance, Ultra-Flexible, and Brain-Conformable Micro-ECoG Arrays, *IEEE Transactions on Neural Systems and Rehabilitation Engineering* 23(3) (2015) 342-350.
- [87] D. Hukins, A. Mahomed, S. Kukureka, Accelerated aging for testing polymeric biomaterials and medical devices, *Medical engineering & physics* 30(10) (2008) 1270-1274.
- [88] B.J. Lambert, F.-W. Tang, Rationale for practical medical device accelerated aging programs in AAMI TIR 17, *Radiation Physics and Chemistry* 57(3-6) (2000) 349-353.
- [89] A. International, Standard Guide for Accelerated Aging of Sterile Barrier Systems for Medical Devices, www.astm.org, 2016.
- [90] P. Takmakov, K. Ruda, K. Scott Phillips, I.S. Isayeva, V. Krauthamer, C.G. Welle, Rapid evaluation of the durability of cortical neural implants using accelerated aging with reactive oxygen species, *J Neural Eng* 12(2) (2015) 026003.
- [91] Y.Y. Duan, G.M. Clark, R.S. Cowan, Factors determining and limiting the impedance behavior of implanted bioelectrodes, *Smart Structures and Devices, International Society for Optics and Photonics*, 2001, pp. 498-508.
- [92] F.B. Karp, N.A. Bernotski, T.I. Valdes, K.F. Bohringer, B.D. Ratner, Foreign body response investigated with an implanted biosensor by in situ electrical impedance spectroscopy, *IEEE Sensors Journal* 8(1) (2008) 104-112.
- [93] J.C. Williams, J.A. Hippensteel, J. Dilgen, W. Shain, D.R. Kipke, Complex impedance spectroscopy for monitoring tissue responses to inserted neural implants, *Journal of neural engineering* 4(4) (2007) 410.

- [94] M.M. Straka, B. Shafer, S. Vasudevan, C. Welle, L. Rieth, Characterizing longitudinal changes in the impedance spectra of in-vivo peripheral nerve electrodes, *Micromachines (Basel)* 9(11) (2018) 587.
- [95] J. Zhou, D.H. Anjum, L. Chen, X. Xu, I.A. Ventura, L. Jiang, G. Lubineau, The temperature-dependent microstructure of PEDOT/PSS films: insights from morphological, mechanical and electrical analyses, *Journal of Materials Chemistry C* 2(46) (2014) 9903-9910.
- [96] Y. Kuramochi, X. Guo, D.B. Sawyer, C.C. Lim, Rapid electrical stimulation induces early activation of kinase signal transduction pathways and apoptosis in adult rat ventricular myocytes, *Exp Physiol* 91(4) (2006) 773-80.
- [97] Z. Allahyari, N. Haghighipour, F. Moztarzadeh, L. Ghazizadeh, M. Hamrang, M.A. Shokrgozar, S. Gholizadeh, Optimization of electrical stimulation parameters for MG-63 cell proliferation on chitosan/functionalized multiwalled carbon nanotube films, *RSC Advances* 6(111) (2016) 109902-109915.
- [98] C. Chen, X. Bai, Y. Ding, I.-S. Lee, Electrical stimulation as a novel tool for regulating cell behavior in tissue engineering, *Biomaterials Research* 23(1) (2019) 25.
- [99] A. Puiggali-Jou, L.J. Del Valle, C. Alemán, Cell Responses to Electrical Pulse Stimulation for Anticancer Drug Release, *Materials (Basel)* 12(16) (2019) 2633.
- [100] E. Castagnola, A. Ansaldo, E. Maggiolini, G.N. Angotzi, M. Skrap, D. Ricci, L. Fadiga, Biologically Compatible Neural Interface To Safely Couple Nanocoated Electrodes to the Surface of the Brain, *ACS Nano* 7(5) (2013) 3887-3895.
- [101] D.B. McCreery, W.F. Agnew, T.G.H. Yuen, L.A. Bullara, Comparison of neural damage induced by electrical stimulation with faradaic and capacitor electrodes, *Annals of Biomedical Engineering* 16(5) (1988) 463-481.
- [102] T.D. Kozai, K. Catt, Z. Du, K. Na, O. Srivannavit, R.U. Haque, J. Seymour, K.D. Wise, E. Yoon, X.T. Cui, Chronic In Vivo Evaluation of PEDOT/CNT for Stable Neural Recordings, *IEEE Trans Biomed Eng* 63(1) (2016) 111-9.
- [103] T.D.Y. Kozai, A.S. Jaquins-Gerstl, A.L. Vazquez, A.C. Michael, X.T. Cui, Brain Tissue Responses to Neural Implants Impact Signal Sensitivity and Intervention Strategies, *ACS Chemical Neuroscience* 6(1) (2015) 48-67.

- [104] X. Zheng, K.M. Woepfel, A.Y. Griffith, E. Chang, M.J. Looker, L.E. Fisher, B.J. Clapsaddle, X.T. Cui, Soft Conducting Elastomer for Peripheral Nerve Interface, *Advanced Healthcare Materials* 8(9) (2019) 1801311.
- [105] X.S. Zheng, N.R. Snyder, K. Woepfel, J.H. Barengo, X. Li, J. Eles, C.L. Kolarcik, X.T. Cui, A superoxide scavenging coating for improving tissue response to neural implants, *Acta Biomaterialia* 99 (2019) 72-83.
- [106] B. Bent, C. Chiang, C. Wang, N. Lad, A. Kent, J. Viventi, Simultaneous Recording and Stimulation Instrumentation for Closed Loop Spinal Cord Stimulation, 2019 9th International IEEE/EMBS Conference on Neural Engineering (NER), 2019, pp. 694-697.
- [107] M.E.J. Obien, K. Deligkaris, T. Bullmann, D.J. Bakkum, U. Frey, Revealing neuronal function through microelectrode array recordings, *Frontiers in Neuroscience* 8(423) (2015).
- [108] S. Takahashi, S. Muramatsu, J. Nishikawa, K. Satoh, S. Murakami, T. Tateno, Laminar responses in the auditory cortex using a multielectrode array substrate for simultaneous stimulation and recording, *IEEJ Transactions on Electrical and Electronic Engineering* 14(2) (2019) 303-311.
- [109] D.J. O'Shea, K.V. Shenoy, ERAASR: an algorithm for removing electrical stimulation artifacts from multielectrode array recordings, *Journal of neural engineering* 15(2) (2018) 026020-026020.
- [110] K.W. King, W.F. Cusack, A.C. Nanivadekar, C.A. Ayers, M.A. Urbin, R.A. Gaunt, L.E. Fisher, D.J. Weber, DRG microstimulation evokes postural responses in awake, standing felines, *Journal of Neural Engineering* 17(1) (2019) 016014.
- [111] C. Newbold, R. Richardson, R. Millard, P. Seligman, R. Cowan, R. Shepherd, Electrical stimulation causes rapid changes in electrode impedance of cell-covered electrodes, *Journal of neural engineering* 8(3) (2011) 036029-036029.
- [112] A. Gonzalez-Calle, J.D. Weiland, Evaluation of Effects of Electrical Stimulation in the Retina with Optical Coherence Tomography, *Annu Int Conf IEEE Eng Med Biol Soc* 2016 (2016) 6182-6185.
- [113] Y.-C. Chang, J.D. Weiland, Stimulation Strategies for Selective Activation of Retinal Ganglion Cells, *Int IEEE EMBS Conf Neural Eng* 2017 (2017) 345-348.

- [114] M.H. Histed, V. Bonin, R.C. Reid, Direct activation of sparse, distributed populations of cortical neurons by electrical microstimulation, *Neuron* 63(4) (2009) 508-522.
- [115] N.J. Michelson, J.R. Eles, A.L. Vazquez, K.A. Ludwig, T.D.Y. Kozai, Calcium activation of cortical neurons by continuous electrical stimulation: Frequency-dependence, temporal fidelity and activation density, *bioRxiv* (2018) 338525.
- [116] K.C. Stieger, J.R. Eles, K.A. Ludwig, T.D.Y. Kozai, In vivo microstimulation with cathodic and anodic asymmetric waveforms modulates spatiotemporal calcium dynamics in cortical neuropil and pyramidal neurons of male mice, *Journal of Neuroscience Research* 98(10) (2020) 2072-2095.
- [117] J.R. Eles, T.D.Y. Kozai, In vivo imaging of calcium and glutamate responses to intracortical microstimulation reveals distinct temporal responses of the neuropil and somatic compartments in layer II/III neurons, *Biomaterials* 234 (2020) 119767.
- [118] J.R. Eles, A.L. Vazquez, T.D.Y. Kozai, X.T. Cui, In vivo imaging of neuronal calcium during electrode implantation: Spatial and temporal mapping of damage and recovery, *Biomaterials* 174 (2018) 79-94.
- [119] J.K. Trevathan, A.J. Asp, E.N. Nicolai, J.M. Trevathan, N.A. Kremer, T.D.Y. Kozai, D. Cheng, M.J. Schachter, J.J. Nassi, S.L. Otte, Calcium imaging in freely-moving mice during electrical stimulation of deep brain structures, *bioRxiv* (2020) 460220.
- [120] T.D.Y. Kozai, J.R. Eles, A.L. Vazquez, X.T. Cui, Two-photon imaging of chronically implanted neural electrodes: Sealing methods and new insights, *Journal of neuroscience methods* 258 (2016) 46-55.
- [121] J. Lecoq, N. Orlova, B.F. Grewe, Wide. fast. deep: recent advances in multiphoton microscopy of in vivo neuronal activity, *Journal of Neuroscience* 39(46) (2019) 9042-9052.
- [122] K.E. Jones, P.K. Campbell, R.A. Normann, A glass/silicon composite intracortical electrode array, *Annals of biomedical engineering* 20(4) (1992) 423-437.
- [123] M. Ferguson, D. Sharma, D. Ross, F. Zhao, A Critical Review of Microelectrode Arrays and Strategies for Improving Neural Interfaces, *Advanced Healthcare Materials* 8(19) (2019) 1900558.

- [124] S. Negi, R. Bhandari, L. Rieth, F. Solzbacher, In vitro comparison of sputtered iridium oxide and platinum-coated neural implantable microelectrode arrays, *Biomedical materials* 5(1) (2010) 015007.
- [125] E.K. Brunton, B. Winther-Jensen, C. Wang, E.B. Yan, S. Hagh Gooie, A.J. Lowery, R. Rajan, In vivo comparison of the charge densities required to evoke motor responses using novel annular penetrating microelectrodes, *Frontiers in neuroscience* 9 (2015) 265.
- [126] A. Ghazavi, J. Maeng, M. Black, S. Salvi, S. Cogan, Electrochemical characteristics of ultramicro-dimensioned SIROF electrodes for neural stimulation and recording, *Journal of neural engineering* 17(1) (2020) 016022.
- [127] C. Chen, S. Ruan, X. Bai, C. Lin, C. Xie, I.-S. Lee, Patterned iridium oxide film as neural electrode interface: biocompatibility and improved neurite outgrowth with electrical stimulation, *Materials Science and Engineering: C* 103 (2019) 109865.
- [128] P.H. Peckham, D.M. Ackermann Jr, C.W. Moss, The role of biomaterials in stimulating bioelectrodes, *Biomaterials Science*, Elsevier2013, pp. 981-996.
- [129] S.F. Cogan, P.R. Troyk, J. Ehrlich, T.D. Plante, In vitro comparison of the charge-injection limits of activated iridium oxide (AIROF) and platinum-iridium microelectrodes, *IEEE Transactions on Biomedical Engineering* 52(9) (2005) 1612-1614.
- [130] R.A. Green, P.B. Matteucci, R.T. Hassarati, B. Giraud, C.W.D. Dodds, S. Chen, P.J. Byrnes-Preston, G.J. Suaning, L.A. Poole-Warren, N.H. Lovell, Performance of conducting polymer electrodes for stimulating neuroprosthetics, *Journal of Neural Engineering* 10(1) (2013) 016009.
- [131] D.E. Arreaga-Salas, A. Avendaño-Bolívar, D. Simon, R. Reit, A. Garcia-Sandoval, R.L. Rennaker, W. Voit, Integration of high-charge-injection-capacity electrodes onto polymer softening neural interfaces, *ACS applied materials & interfaces* 7(48) (2015) 26614-26623.
- [132] Y.-M. Chen, T.-W. Chung, P.-W. Wu, P.-C. Chen, A cost-effective fabrication of iridium oxide films as biocompatible electrostimulation electrodes for neural interface applications, *Journal of Alloys and Compounds* 692 (2017) 339-345.
- [133] S.F. Cogan, A.A. Guzelian, W.F. Agnew, T.G.H. Yuen, D.B. McCreery, Over-pulsing degrades activated iridium oxide films used for intracortical neural stimulation, *Journal of Neuroscience Methods* 137(2) (2004) 141-150.

- [134] S. Meijs, M. Fjorback, N.J. Rijkhoff, Chronic electrochemical investigation of titanium nitride stimulation electrodes in vivo, *Converging clinical and engineering research on neurorehabilitation*, Springer2013, pp. 421-425.
- [135] N.A. Steinmetz, C. Koch, K.D. Harris, M. Carandini, Challenges and opportunities for large-scale electrophysiology with Neuropixels probes, *Current opinion in neurobiology* 50 (2018) 92-100.
- [136] B. Dutta, A. Andrei, T. Harris, C. Lopez, J. O'Callahan, J. Putzeys, B. Raducanu, S. Severi, S. Stavisky, E. Trautmann, The Neuropixels probe: A CMOS based integrated microsystems platform for neuroscience and brain-computer interfaces, 2019 IEEE International Electron Devices Meeting (IEDM), IEEE, 2019, pp. 10.1. 1-10.1. 4.
- [137] J. Maeng, B. Chakraborty, N. Geramifard, T. Kang, R.T. Rihani, A. Joshi-Imre, S.F. Cogan, High-charge-capacity sputtered iridium oxide neural stimulation electrodes deposited using water vapor as a reactive plasma constituent, *Journal of Biomedical Materials Research Part B: Applied Biomaterials* 108(3) (2020) 880-891.
- [138] F. Deku, Y. Cohen, A. Joshi-Imre, A. Kanneganti, T.J. Gardner, S.F. Cogan, Amorphous silicon carbide ultramicroelectrode arrays for neural stimulation and recording, *Journal of neural engineering* 15(1) (2018) 016007.
- [139] S.F. Cogan, A.A. Guzelian, W.F. Agnew, T.G. Yuen, D.B. McCreery, Over-pulsing degrades activated iridium oxide films used for intracortical neural stimulation, *Journal of neuroscience methods* 137(2) (2004) 141-150.
- [140] R. Atmaramani, B. Chakraborty, R.T. Rihani, J. Usoro, A. Hammack, J. Abbott, P. Nnoromele, B.J. Black, J.J. Pancrazio, S.F. Cogan, Ruthenium oxide based microelectrode arrays for in vitro and in vivo neural recording and stimulation, *Acta biomaterialia* 101 (2020) 565-574.
- [141] M.R. Abidian, J.M. Corey, D.R. Kipke, D.C. Martin, Conducting-polymer nanotubes improve electrical properties, mechanical adhesion, neural attachment, and neurite outgrowth of neural electrodes, *small* 6(3) (2010) 421-429.
- [142] E. Seker, Y. Berdichevsky, M.R. Begley, M.L. Reed, K.J. Staley, M.L. Yarmush, The fabrication of low-impedance nanoporous gold multiple-electrode arrays for neural electrophysiology studies, *Nanotechnology* 21(12) (2010) 125504.
- [143] T. Nyberg, A. Shimada, K. Torimitsu, Ion conducting polymer microelectrodes for interfacing with neural networks, *Journal of neuroscience methods* 160(1) (2007) 16-25.

- [144] M. Vázquez, J. Bobacka, A. Ivaska, A. Lewenstam, Influence of oxygen and carbon dioxide on the electrochemical stability of poly(3,4-ethylenedioxythiophene) used as ion-to-electron transducer in all-solid-state ion-selective electrodes, *Sensors and Actuators B: Chemical* 82(1) (2002) 7-13.
- [145] X. Cui, D.C. Martin, Electrochemical deposition and characterization of poly(3,4-ethylenedioxythiophene) on neural microelectrode arrays, *Sensors and Actuators B: Chemical* 89(1) (2003) 92-102.
- [146] J. Bobacka, A. Lewenstam, A. Ivaska, Electrochemical impedance spectroscopy of oxidized poly(3,4-ethylenedioxythiophene) film electrodes in aqueous solutions, *Journal of Electroanalytical Chemistry* 489(1) (2000) 17-27.
- [147] H. Vara, J.E. Collazos-Castro, Enhanced spinal cord microstimulation using conducting polymer-coated carbon microfibers, *Acta Biomaterialia* 90 (2019) 71-86.
- [148] A.S. Pranti, A. Schander, A. Bödecker, W. Lang, PEDOT: PSS coating on gold microelectrodes with excellent stability and high charge injection capacity for chronic neural interfaces, *Sensors and Actuators B: Chemical* 275 (2018) 382-393.
- [149] R.A. Green, R.T. Hassarati, L. Bouchinet, C.S. Lee, G.L. Cheong, F.Y. Jin, C.W. Dodds, G.J. Suaning, L.A. Poole-Warren, N.H. Lovell, Substrate dependent stability of conducting polymer coatings on medical electrodes, *Biomaterials* 33(25) (2012) 5875-5886.
- [150] X. Cui, D.C. Martin, Fuzzy gold electrodes for lowering impedance and improving adhesion with electrodeposited conducting polymer films, *Sensors and Actuators A: Physical* 103(3) (2003) 384-394.
- [151] R.A. Green, R.T. Hassarati, L. Bouchinet, C.S. Lee, G.L.M. Cheong, J.F. Yu, C.W. Dodds, G.J. Suaning, L.A. Poole-Warren, N.H. Lovell, Substrate dependent stability of conducting polymer coatings on medical electrodes, *Biomaterials* 33(25) (2012) 5875-5886.
- [152] M. Vomero, E. Castagnola, F. Ciarpella, E. Maggiolini, N. Goshi, E. Zucchini, S. Carli, L. Fadiga, S. Kassegne, D. Ricci, Highly Stable Glassy Carbon Interfaces for Long-Term Neural Stimulation and Low-Noise Recording of Brain Activity, *Scientific Reports* 7(1) (2017) 40332.
- [153] C. Bodart, N. Rossetti, J.E. Hagler, P. Chevreau, D. Chhin, F. Soavi, S.B. Schougaard, F. Amzica, F. Cicoira, Electropolymerized Poly(3,4-ethylenedioxythiophene) (PEDOT) Coatings for Implantable Deep-Brain-Stimulating Microelectrodes, *ACS Applied Materials & Interfaces* 11(19) (2019) 17226-17233.

- [154] Z.J. Du, X. Luo, C.L. Weaver, X.T. Cui, Poly (3, 4-ethylenedioxythiophene)-ionic liquid coating improves neural recording and stimulation functionality of MEAs, *Journal of Materials Chemistry C* 3(25) (2015) 6515-6524.
- [155] A. Guiseppi-Elie, G. Wnek, Stability of iodine-doped polyacetylene in aqueous environments, *Le Journal de Physique Colloques* 44(C3) (1983) C3-193-C3-197.
- [156] J.J. Clark, Toxicology of perchlorate, *Perchlorate in the Environment*, Springer2000, pp. 15-29.
- [157] S.-M. Kim, N. Kim, Y. Kim, M.-S. Baik, M. Yoo, D. Kim, W.-J. Lee, D.-H. Kang, S. Kim, K. Lee, M.-H. Yoon, High-performance, polymer-based direct cellular interfaces for electrical stimulation and recording, *NPG Asia Materials* 10(4) (2018) 255-265.
- [158] K. Matsumoto, C. Sato, Y. Naka, R. Whitby, N. Shimizu, Stimulation of neuronal neurite outgrowth using functionalized carbon nanotubes, *Nanotechnology* 21(11) (2010) 115101.
- [159] T.I. Chao, S. Xiang, C.S. Chen, W.C. Chin, A.J. Nelson, C. Wang, J. Lu, Carbon nanotubes promote neuron differentiation from human embryonic stem cells, *Biochem Biophys Res Commun* 384(4) (2009) 426-30.
- [160] H.-C. Tian, J.-Q. Liu, D.-X. Wei, X.-Y. Kang, C. Zhang, J.-C. Du, B. Yang, X. Chen, H.-Y. Zhu, Y.-N. NuLi, Graphene oxide doped conducting polymer nanocomposite film for electrode-tissue interface, *Biomaterials* 35(7) (2014) 2120-2129.
- [161] S. Carli, L. Lambertini, E. Zucchini, F. Ciarpella, A. Scarpellini, M. Prato, E. Castagnola, L. Fadiga, D. Ricci, Single walled carbon nanohorns composite for neural sensing and stimulation, *Sensors and Actuators B: Chemical* 271 (2018) 280-288.
- [162] T.D. Kozai, A.S. Jaquins-Gerstl, A.L. Vazquez, A.C. Michael, X.T. Cui, Dexamethasone retrodialysis attenuates microglial response to implanted probes in vivo, *Biomaterials* 87 (2016) 157-169.
- [163] C. Boehler, C. Kleber, N. Martini, Y. Xie, I. Dryg, T. Stieglitz, U.G. Hofmann, M. Asplund, Actively controlled release of Dexamethasone from neural microelectrodes in a chronic in vivo study, *Biomaterials* 129 (2017) 176-187.
- [164] N.A. Alba, Z.J. Du, K.A. Catt, T.D.Y. Kozai, X.T. Cui, In Vivo Electrochemical Analysis of a PEDOT/MWCNT Neural Electrode Coating, *Biosensors (Basel)* 5(4) (2015) 618-646.

- [165] X. Luo, C. Matranga, S. Tan, N. Alba, X.T. Cui, Carbon nanotube nanoreservoir for controlled release of anti-inflammatory dexamethasone, *Biomaterials* 32(26) (2011) 6316-6323.
- [166] C.L. Weaver, J.M. LaRosa, X. Luo, X.T. Cui, Electrically controlled drug delivery from graphene oxide nanocomposite films, *ACS nano* 8(2) (2014) 1834-1843.
- [167] K.M. Woepfel, X.S. Zheng, Z.M. Schulte, N.L. Rosi, X.T. Cui, Nanoparticle Doped PEDOT for Enhanced Electrode Coatings and Drug Delivery, *Advanced Healthcare Materials* 8(21) (2019) 1900622.
- [168] N. Peixoto, K. Jackson, R. Samiyi, S. Minnikanti, Charge Storage: Stability measures in implantable electrodes, 2009 Annual International Conference of the IEEE Engineering in Medicine and Biology Society, 2009, pp. 658-661.
- [169] L. Du, T. Li, F. Jin, Y. Wang, R. Li, J. Zheng, T. Wang, Z.-Q. Feng, Design of high conductive and piezoelectric poly(3,4-ethylenedioxythiophene)/chitosan nanofibers for enhancing cellular electrical stimulation, *Journal of Colloid and Interface Science* 559 (2020) 65-75.
- [170] X. Luo, C.L. Weaver, D.D. Zhou, R. Greenberg, X.T. Cui, Highly stable carbon nanotube doped poly(3,4-ethylenedioxythiophene) for chronic neural stimulation, *Biomaterials* 32(24) (2011) 5551-7.
- [171] M. Vomero, E. Castagnola, F. Ciarpella, E. Maggiolini, N. Goshi, E. Zucchini, S. Carli, L. Fadiga, S. Kassegne, D. Ricci, Highly stable glassy carbon interfaces for long-term neural stimulation and low-noise recording of brain activity, *Scientific reports* 7(1) (2017) 1-14.
- [172] N.V. Apollo, M.I. Maturana, W. Tong, D.A. Nayagam, M.N. Shivdasani, J. Foroughi, G.G. Wallace, S. Praver, M.R. Ibbotson, D.J. Garrett, Soft, flexible freestanding neural stimulation and recording electrodes fabricated from reduced graphene oxide, *Advanced Functional Materials* 25(23) (2015) 3551-3559.
- [173] K. Wang, H.A. Fishman, H. Dai, J.S. Harris, Neural stimulation with a carbon nanotube microelectrode array, *Nano letters* 6(9) (2006) 2043-2048.
- [174] F. Vitale, S.R. Summerson, B. Aazhang, C. Kemere, M. Pasquali, Neural stimulation and recording with bidirectional, soft carbon nanotube fiber microelectrodes, *ACS nano* 9(4) (2015) 4465-4474.

- [175] M. Losurdo, M.M. Giangregorio, P. Capezzuto, G. Bruno, Graphene CVD growth on copper and nickel: role of hydrogen in kinetics and structure, *Physical Chemistry Chemical Physics* 13(46) (2011) 20836-20843.
- [176] A.T. Murdock, C.D. Van Engers, J. Britton, V. Babenko, S.S. Meysami, H. Bishop, A. Crossley, A.A. Koos, N. Grobert, Targeted removal of copper foil surface impurities for improved synthesis of CVD graphene, *Carbon* 122 (2017) 207-216.
- [177] E. Terrado, M. Redrado, E. Munoz, W. Maser, A. Benito, M. Martinez, Carbon nanotube growth on cobalt-sprayed substrates by thermal CVD, *Materials Science and Engineering: C* 26(5-7) (2006) 1185-1188.
- [178] E. Castagnola, A. Ansaldo, E. Maggiolini, T. Ius, M. Skrap, D. Ricci, L. Fadiga, Smaller, softer, lower-impedance electrodes for human neuroprosthesis: a pragmatic approach, *Frontiers in neuroengineering* 7 (2014) 8.
- [179] E. Castagnola, A. Ansaldo, L. Fadiga, D. Ricci, Chemical vapour deposited carbon nanotube coated microelectrodes for intracortical neural recording, *physica status solidi (b)* 247(11-12) (2010) 2703-2707.
- [180] T.D.Y. Kozai, N.B. Langhals, P.R. Patel, X. Deng, H. Zhang, K.L. Smith, J. Lahann, N.A. Kotov, D.R. Kipke, Ultrasmall implantable composite microelectrodes with bioactive surfaces for chronic neural interfaces, *Nature materials* 11(12) (2012) 1065.
- [181] P.R. Patel, K. Na, H. Zhang, T.D. Kozai, N.A. Kotov, E. Yoon, C.A. Chestek, Insertion of linear 8.4 μm diameter 16 channel carbon fiber electrode arrays for single unit recordings, *Journal of neural engineering* 12(4) (2015) 046009.
- [182] H.N. Schwerdt, M. Kim, E. Karasan, S. Amemori, D. Homma, H. Shimazu, T. Yoshida, R. Langer, A.M. Graybiel, M.J. Cima, Subcellular electrode arrays for multisite recording of dopamine in vivo, 2017 IEEE 30th International Conference on Micro Electro Mechanical Systems (MEMS), IEEE, 2017, pp. 549-552.
- [183] H.N. Schwerdt, H. Shimazu, K.-i. Amemori, S. Amemori, P.L. Tierney, D.J. Gibson, S. Hong, T. Yoshida, R. Langer, M.J. Cima, Long-term dopamine neurochemical monitoring in primates, *Proceedings of the National Academy of Sciences* 114(50) (2017) 13260-13265.
- [184] P.R. Patel, H. Zhang, M.T. Robbins, J.B. Nofar, S.P. Marshall, M.J. Kobylarek, T.D. Kozai, N.A. Kotov, C.A. Chestek, Chronic in vivo stability assessment of carbon fiber microelectrode arrays, *Journal of neural engineering* 13(6) (2016) 066002.

- [185] H.N. Schwerdt, E. Zhang, M.J. Kim, T. Yoshida, L. Stanwicks, S. Amemori, H.E. Dagdeviren, R. Langer, M.J. Cima, A.M. Graybiel, Cellular-scale probes enable stable chronic subsecond monitoring of dopamine neurochemicals in a rodent model, *Communications biology* 1(1) (2018) 144.
- [186] H.N. Schwerdt, E. Zhang, M.J. Kim, T. Yoshida, L. Stanwicks, S. Amemori, H.E. Dagdeviren, R. Langer, M.J. Cima, A.M. Graybiel, Cellular-scale probes enable stable chronic subsecond monitoring of dopamine neurochemicals in a rodent model, *Communications biology* 1(1) (2018) 1-11.
- [187] E.J. Welle, P.R. Patel, J.E. Woods, A. Petrossians, E. della Valle, A. Vega-Medina, J.M. Richie, D. Cai, J.D. Weiland, C.A. Chestek, Ultra-small carbon fiber electrode recording site optimization and improved in vivo chronic recording yield, *Journal of Neural Engineering* 17(2) (2020) 026037.
- [188] N.T. Alvarez, E. Buschbeck, S. Miller, A.D. Le, V.K. Gupta, C. Ruhunage, I. Vilinsky, Y. Ma, Carbon Nanotube Fibers for Neural Recording and Stimulation, *ACS Applied Bio Materials* 3(9) (2020) 6478-6487.
- [189] K. Wang, C.L. Frewin, D. Esrafilzadeh, C. Yu, C. Wang, J.J. Pancrazio, M. Romero-Ortega, R. Jalili, G. Wallace, High-Performance Graphene-Fiber-Based Neural Recording Microelectrodes, *Advanced Materials* 31(15) (2019) 1805867.
- [190] C. Yang, C.B. Jacobs, M.D. Nguyen, M. Ganesana, A.G. Zestos, I.N. Ivanov, A.A. Puretzky, C.M. Rouleau, D.B. Geohegan, B.J. Venton, Carbon nanotubes grown on metal microelectrodes for the detection of dopamine, *Analytical chemistry* 88(1) (2016) 645-652 <https://doi.org/10.1021/acs.analchem.5b01257>.
- [191] E. Castagnola, N.W. Vahidi, S. Nimbalkar, S. Rudraraju, M. Thielk, E. Zucchini, C. Cea, S. Carli, T.Q. Gentner, D. Ricci, In vivo dopamine detection and single unit recordings using intracortical glassy carbon microelectrode arrays, *MRS advances* 3(29) (2018) 1629-1634.
- [192] M. Vomero, A. Oliveira, D. Ashouri, M. Eickenscheidt, T. Stieglitz, Graphitic carbon electrodes on flexible substrate for neural applications entirely fabricated using infrared nanosecond laser technology, *Scientific reports* 8(1) (2018) 1-13.
- [193] N. Goshi, E. Castagnola, M. Vomero, C. Gueli, C. Cea, E. Zucchini, D. Bjanec, E. Maggiolini, C. Moritz, S. Kassegne, Glassy carbon MEMS for novel origami-styled 3D integrated intracortical and epicortical neural probes, *Journal of Micromechanics and Microengineering* 28(6) (2018) 065009.

- [194] N.W. Vahidi, S. Rudraraju, E. Castagnola, C. Cea, S. Nimbalkar, R. Hanna, R. Arvizu, S.A. Dayeh, T.Q. Gentner, S. Kassegne, Epi-intra neural probes with glassy carbon microelectrodes help elucidate neural coding and stimulus encoding in 3D volume of tissue, *Journal of Neural Engineering* (2020).
- [195] M.A. Hejazi, W. Tong, A. Stacey, A. Soto-Breceda, M.R. Ibbotson, M. Yunzab, M.I. Maturana, A. Almasi, Y.J. Jung, S. Sun, Hybrid diamond/carbon fiber microelectrodes enable multimodal electrical/chemical neural interfacing, *Biomaterials* 230 (2020) 119648.
- [196] Y.H. Luo, L. da Cruz, The Argus(®) II Retinal Prosthesis System, *Prog Retin Eye Res* 50 (2016) 89-107.
- [197] J. Menzel-Severing, T. Laube, C. Brockmann, N. Bornfeld, W. Mokwa, B. Mazinani, P. Walter, G. Roessler, Implantation and explantation of an active epiretinal visual prosthesis: 2-year follow-up data from the EPIRET3 prospective clinical trial, *Eye (Lond)* 26(4) (2012) 501-9.
- [198] K. Stingl, K.U. Bartz-Schmidt, D. Besch, C.K. Chee, C.L. Cottrill, F. Gekeler, M. Groppe, T.L. Jackson, R.E. MacLaren, A. Koitschev, A. Kusnyerik, J. Neffendorf, J. Nemeth, M.A. Naeem, T. Peters, J.D. Ramsden, H. Sachs, A. Simpson, M.S. Singh, B. Wilhelm, D. Wong, E. Zrenner, Subretinal Visual Implant Alpha IMS--Clinical trial interim report, *Vision Res* 111(Pt B) (2015) 149-60.
- [199] D. De Ridder, G. De Mulder, E. Verstraeten, K. Van der Kelen, S. Sunaert, M. Smits, S. Kovacs, J. Verlooy, P. Van de Heyning, A.R. Moller, Primary and secondary auditory cortex stimulation for intractable tinnitus, *ORL J Otorhinolaryngol Relat Spec* 68(1) (2006) 48-54; discussion 54-5.
- [200] S. Flesher, J. Collinger, J. Weiss, C. Hughes, S. Bensmaia, M. Boninger, R. Gaunt, Restoring Touch through Intracortical Microstimulation of Human Somatosensory Cortex, 2017 New Generation of CAS (NGCAS), 2017, pp. 185-188.
- [201] M.C. Genovese, N. Gaylis, D. Sikes, A. Kivitz, D.M. Horowitz, C. Peterfy, Y. Levine, D. Chernoff, LB0009 FIRST-IN-HUMAN STUDY OF NOVEL IMPLANTED VAGUS NERVE STIMULATION DEVICE TO TREAT RHEUMATOID ARTHRITIS, BMJ Publishing Group Ltd, 2019.
- [202] P. Staats, C. Emala, B. Simon, J. Errico, Neurostimulation for asthma, *Neuromodulation*, Elsevier 2018, pp. 1339-1345.

- [203] E.B. Masi, T. Levy, T. Tsaava, C.E. Bouton, K.J. Tracey, S.S. Chavan, T.P. Zanos, Identification of hypoglycemia-specific neural signals by decoding murine vagus nerve activity, *Bioelectronic Medicine* 5(1) (2019) 9.
- [204] M. Tykocinski, Y. Duan, B. Tabor, R.S. Cowan, Chronic electrical stimulation of the auditory nerve using high surface area (HiQ) platinum electrodes, *Hearing Research* 159(1) (2001) 53-68.
- [205] C. Boehler, F. Oberueber, T. Stieglitz, M. Asplund, Nanostructured platinum as an electrochemically and mechanically stable electrode coating, 2017 39th Annual International Conference of the IEEE Engineering in Medicine and Biology Society (EMBC), 2017, pp. 1058-1061.
- [206] R. Hornig, T. Laube, P. Walter, M. Velikay-Parel, N. Bornfeld, M. Feucht, H. Akguel, G. Rössler, N. Alteheld, D.L. Notarp, A method and technical equipment for an acute human trial to evaluate retinal implant technology, *Journal of neural engineering* 2(1) (2005) S129.
- [207] G. Richard, M. Feucht, N. Bornfeld, T. Laube, G. Rössler, M. Velikay–Parel, R. Hornig, Multicenter study on acute electrical stimulation of the human retina with an epiretinal implant: clinical results in 20 patients, *Investigative Ophthalmology & Visual Science* 46(13) (2005) 1143-1143.
- [208] S.F. Cogan, A.A. Guzelian, W.F. Agnew, T.G. Yuen, D.B. McCreery, Over-pulsing degrades activated iridium oxide films used for intracortical neural stimulation, *J Neurosci Methods* 137(2) (2004) 141-50.
- [209] K.A. Ludwig, N.B. Langhals, M.D. Joseph, S.M. Richardson-Burns, J.L. Hendricks, D.R. Kipke, Poly(3,4-ethylenedioxythiophene) (PEDOT) polymer coatings facilitate smaller neural recording electrodes, *Journal of neural engineering* 8(1) (2011) 014001-014001.
- [210] Z.J. Du, X. Luo, C.L. Weaver, X.T. Cui, Poly(3,4-ethylenedioxythiophene)-ionic liquid coating improves neural recording and stimulation functionality of MEAs, *Journal of Materials Chemistry C* 3(25) (2015) 6515-6524.
- [211] Z. Aqrawe, N. Patel, Y. Vyas, M. Bansal, J. Montgomery, J. Travas-Sejdic, D. Svirskis, A simultaneous optical and electrical in-vitro neuronal recording system to evaluate microelectrode performance, *PLOS ONE* 15(8) (2020) e0237709.

- [212] S. Wilks, S. Richardson-Burn, J. Hendricks, D. Martin, K. Otto, Poly(3,4-ethylene dioxothiophene) (PEDOT) as a micro-neural interface material for electrostimulation, *Frontiers in Neuroengineering* 2(7) (2009).
- [213] R. Samba, T. Herrmann, G. Zeck, PEDOT–CNT coated electrodes stimulate retinal neurons at low voltage amplitudes and low charge densities, *Journal of neural engineering* 12(1) (2015) 016014.
- [214] R. Gerwig, K. Fuchsberger, B. Schroepfel, G.S. Link, G. Heusel, U. Kraushaar, W. Schuhmann, A. Stett, M. Stelzle, PEDOT–CNT composite microelectrodes for recording and electrostimulation applications: fabrication, morphology, and electrical properties, *Frontiers in neuroengineering* 5 (2012) 8.
- [215] A. Liu, M. Vöröslakos, G. Kronberg, S. Henin, M.R. Krause, Y. Huang, A. Opitz, A. Mehta, C.C. Pack, B. Krekelberg, A. Berényi, L.C. Parra, L. Melloni, O. Devinsky, G. Buzsáki, Immediate neurophysiological effects of transcranial electrical stimulation, *Nature Communications* 9(1) (2018) 5092.
- [216] R.J. Racine, Modification of seizure activity by electrical stimulation: I. after-discharge threshold, *Electroencephalography and Clinical Neurophysiology* 32(3) (1972) 269-279.
- [217] E.J. Tehovnik, Electrical stimulation of neural tissue to evoke behavioral responses, *Journal of neuroscience methods* 65(1) (1996) 1-17.
- [218] B. Bland, C. Vanderwolf, Electrical stimulation of the hippocampal formation: Behavioral and bioelectrical effects, *Brain Research* 43(1) (1972) 89-106.
- [219] A. Scheiner, J.T. Mortimer, U. Roessmann, Imbalanced biphasic electrical stimulation: muscle tissue damage, *Annals of biomedical engineering* 18(4) (1990) 407-425.
- [220] D.B. McCreery, W.F. Agnew, T.G.H. Yuen, L. Bullara, Charge density and charge per phase as cofactors in neural injury induced by electrical stimulation, *IEEE Transactions on Biomedical Engineering* 37(10) (1990) 996-1001.
- [221] C. Stosiek, O. Garaschuk, K. Holthoff, A. Konnerth, In vivo two-photon calcium imaging of neuronal networks, *Proceedings of the National Academy of Sciences* 100(12) (2003) 7319-7324.

- [222] E. Castagnola, A. Ansaldo, E. Maggiolini, T. Ius, M. Skrap, D. Ricci, L. Fadiga, Smaller, softer, lower-impedance electrodes for human neuroprosthesis: a pragmatic approach, *Frontiers in Neuroengineering* 7(8) (2014).
- [223] H. Dana, T.-W. Chen, A. Hu, B.C. Shields, C. Guo, L.L. Looger, D.S. Kim, K. Svoboda, Thy1-GCaMP6 Transgenic Mice for Neuronal Population Imaging In Vivo, *PLOS ONE* 9(9) (2014) e108697.
- [224] J.L. Devore, *Probability and statistics for engineering and the sciences*, 8th ed. ed., Brooks/Cole, Cengage Learning, Australia ;, 2012.
- [225] E. Tehovnik, A. Tolias, F. Sultan, W. Slocum, N. Logothetis, Direct and indirect activation of cortical neurons by electrical microstimulation, *Journal of neurophysiology* 96 (2006) 512-21.
- [226] P.K. Shetty, F. Galeffi, D.A. Turner, Cellular Links between Neuronal Activity and Energy Homeostasis, *Front Pharmacol* 3 (2012) 43-43.
- [227] X.F. Wei, W.M. Grill, Current density distributions, field distributions and impedance analysis of segmented deep brain stimulation electrodes, *Journal of neural engineering* 2(4) (2005) 139.
- [228] A. Hånell, J.E. Greer, K.M. Jacobs, Increased Network Excitability Due to Altered Synaptic Inputs to Neocortical Layer V Intact and Axotomized Pyramidal Neurons after Mild Traumatic Brain Injury, *J Neurotrauma* 32(20) (2015) 1590-1598.
- [229] X.F. Wei, W.M. Grill, Analysis of high-perimeter planar electrodes for efficient neural stimulation, *Frontiers in neuroengineering* 2 (2009) 15-15.
- [230] C.M. McKay, H.J. McDermott, The perceptual effects of current pulse duration in electrical stimulation of the auditory nerve, *The Journal of the Acoustical Society of America* 106(2) (1999) 998-1009.
- [231] S. Kim, T. Callier, G.A. Tabot, R.A. Gaunt, F.V. Tenore, S.J. Bensmaia, Behavioral assessment of sensitivity to intracortical microstimulation of primate somatosensory cortex, *Proc Natl Acad Sci U S A* 112(49) (2015) 15202-15207.
- [232] S. Hiremath, E. Tyler-Kabara, J. Wheeler, D. Moran, R. Gaunt, J. Collinger, S. Foldes, D. Weber, W. Chen, M. Boninger, W. Wang, Human perception of electrical stimulation on the surface of somatosensory cortex, *PLoS ONE* 12 (2017).

- [233] D.G. Ouzounov, T. Wang, M. Wang, D.D. Feng, N.G. Horton, J.C. Cruz-Hernández, Y.-T. Cheng, J. Reimer, A.S. Tolia, N. Nishimura, In vivo three-photon imaging of activity of GCaMP6-labeled neurons deep in intact mouse brain, *Nature methods* 14(4) (2017) 388-390.
- [234] L. Luan, X. Wei, Z. Zhao, J.J. Siegel, O. Potnis, C.A. Tuppen, S. Lin, S. Kazmi, R.A. Fowler, S. Holloway, Ultraflexible nanoelectronic probes form reliable, glial scar-free neural integration, *Science advances* 3(2) (2017) e1601966.
- [235] M. Lee, H.-O. Kim, J.-H. Boo, Y.-J. Kim, Thermo-mechanical characteristics of the stretchable serpentine-patterned microelectrode, *Functional Materials Letters* 11(03) (2018) 1850054.
- [236] H.H. Draz, S.R.I. Gabran, M. Basha, H. Mostafa, M.F. Abu-Elyazeed, A. Zaki, Comparative mechanical analysis of deep brain stimulation electrodes, *BioMedical Engineering OnLine* 17(1) (2018) 123.
- [237] A. Balasubramani, Design, Microfabrication and Mechanical Characterization of Polymer-Based Microelectrode Arrays, San Diego State University, 2018.
- [238] J.P. Seymour, N.B. Langhals, D.J. Anderson, D.R. Kipke, Novel multi-sided, microelectrode arrays for implantable neural applications, *Biomedical microdevices* 13(3) (2011) 441-451.
- [239] R. GONG, Z. ZHAO, H.e. HUANG, J. WANG, Finite Element Simulation on the Mechanical and Electrical Properties of Double-Sided Microelectrode Array Chip, (2017).
- [240] C.W. Lu, K.A. Malaga, K.L. Chou, C.A. Chestek, P.G. Patil, High density microelectrode recording predicts span of therapeutic tissue activation volumes in subthalamic deep brain stimulation for Parkinson disease, *Brain Stimulation* 13(2) (2020) 412-419.
- [241] H. Park, P. Takmakov, H. Lee, Electrochemical Evaluations of Fractal Microelectrodes for Energy Efficient Neurostimulation, *Scientific Reports* 8(1) (2018) 4375.
- [242] R. Zhang, Y. Zhang, Q. Zhang, H. Xie, W. Qian, F. Wei, Growth of half-meter long carbon nanotubes based on Schulz-Flory distribution, *Acs Nano* 7(7) (2013) 6156-6161.
- [243] Y.-x. Liu, H. Liu, J.-P. Wang, X. Zhang, Thermoelectric behavior of PEDOT:PSS/CNT/graphene composites, *Journal of Polymer Engineering* 38 (2017) 381 - 389.

[244] H.M. Yuxue Liu, Takashi Goto, Electrical and Optical Properties of IrO₂ Thin Films Prepared by Laser-ablation, *Materials Transactions* 45(10) (2004).

[245] C. González, C. Villanueva, C. Vera, O. Flores, R. Reyes, B. Rubinsky, The detection of brain ischaemia in rats by inductive phase shift spectroscopy, *Physiological measurement* 30 (2009) 809-19.

[246] E. Poverenov, M. Li, A. Bitler, M. Bendikov, Major Effect of Electropolymerization Solvent on Morphology and Electrochromic Properties of PEDOT Films, *Chemistry of Materials* 22(13) (2010) 4019-4025.

[247] D.H. Daniels, C.R. Powell, M.R. Braasch, K.J. Kreder, Sacral neuromodulation in diabetic patients: success and complications in the treatment of voiding dysfunction, *Neurourology and Urodynamics: Official Journal of the International Continence Society* 29(4) (2010) 578-581.

[248] J.R. Eles, T.D. Kozai, In vivo imaging of calcium and glutamate responses to intracortical microstimulation reveals distinct temporal responses of the neuropil and somatic compartments in layer II/III neurons, *Biomaterials* 234 (2020) 119767.

[249] K. Chen, S.M. Wellman, Y. Yaxiaer, J.R. Eles, T.D.Y. Kozai, In vivo spatiotemporal patterns of oligodendrocyte and myelin damage at the neural electrode interface, *Biomaterials* 268 (2021).

[250] J.R. Eles, A.L. Vazquez, N.R. Snyder, C. Lagenaur, M.C. Murphy, T.D.Y. Kozai, X.T. Cui, Neuroadhesive L1 coating attenuates acute microglial attachment to neural electrodes as revealed by live two-photon microscopy, *Biomaterials* 113 (2017) 279-292.

[251] S.M. Wellman, T.D. Kozai, In vivo spatiotemporal dynamics of NG2 glia activity caused by neural electrode implantation, *Biomaterials* 164 (2018) 121-133.

[252] C.G. Welle, Y.-R. Gao, M. Ye, A. Lozzi, A. Boretsky, E. Abliz, D.X. Hammer, Longitudinal neural and vascular structural dynamics produced by chronic microelectrode implantation, *Biomaterials* 238 (2020) 119831.

[253] J. Bisquert, G.G. Belmonte, F.F. Santiago, N.S. Ferriols, M. Yamashita, E.C. Pereira, Application of a distributed impedance model in the analysis of conducting polymer films, *Electrochemistry Communications* 2(8) (2000) 601-605.

- [254] Y. Duan, G.M. Clark, R. Cowan, A study of intra-cochlear electrodes and tissue interface by electrochemical impedance methods in vivo, *Biomaterials* 25(17) (2004) 3813-3828.
- [255] T.-W. Chen, T.J. Wardill, Y. Sun, S.R. Pulver, S.L. Renninger, A. Baohan, E.R. Schreier, R.A. Kerr, M.B. Orger, V. Jayaraman, L.L. Looger, K. Svoboda, D.S. Kim, Ultrasensitive fluorescent proteins for imaging neuronal activity, *Nature* 499(7458) (2013) 295-300.
- [256] E. Katz, O. Stoler, A. Scheller, Y. Khrapunsky, S. Goebbels, F. Kirchhoff, M.J. Gutnick, F. Wolf, I.A. Fleidervish, Role of sodium channel subtype in action potential generation by neocortical pyramidal neurons, *Proceedings of the National Academy of Sciences* 115(30) (2018) E7184.
- [257] J.E. Greer, J.T. Povlishock, K.M. Jacobs, Electrophysiological abnormalities in both axotomized and nonaxotomized pyramidal neurons following mild traumatic brain injury, *J Neurosci* 32(19) (2012) 6682-6687.
- [258] A. Campbell, C. Wu, Chronically Implanted Intracranial Electrodes: Tissue Reaction and Electrical Changes, *Micromachines (Basel)* 9(9) (2018) 430.
- [259] E. Azemi, C.F. Lagenaur, X.T. Cui, The surface immobilization of the neural adhesion molecule L1 on neural probes and its effect on neuronal density and gliosis at the probe/tissue interface, *Biomaterials* 32(3) (2011) 681-692.
- [260] J.W. Salatino, A.P. Kale, E.K. Purcell, Alterations in Ion Channel Expression Surrounding Implanted Microelectrode Arrays in the Brain, *bioRxiv* (2019) 518811.
- [261] G.V. Goddard, Development of epileptic seizures through brain stimulation at low intensity, *Nature* 214(5092) (1967) 1020-1021.
- [262] H.L. Grabenstatter, T.P. Sutula, MODELS | Kindling: A Phenomenon of Seizure-Induced Plasticity and a Model of Focal and Limbic Epilepsy, in: P.A. Schwartzkroin (Ed.), *Encyclopedia of Basic Epilepsy Research*, Academic Press, Oxford, 2009, pp. 762-767.
- [263] S.-J. Yoo, S. Ryu, S. Kim, H.S. Han, C. Moon, Reference module in neuroscience and biobehavioral psychology, Elsevier 2017.
- [264] M. Jalilifar, A. Yadollahpour, A.A. Moazedi, Z. Ghotbeddin, Low Frequency Electrical Stimulation Either Prior to Or after Rapid Kindling Stimulation Inhibits the Kindling-Induced Epileptogenesis, *Biomed Res Int* 2017 (2017) 8623743.

- [265] E. Cela, A.R. McFarlan, A.J. Chung, T. Wang, S. Chierzi, K.K. Murai, P.J. Sjöström, An Optogenetic Kindling Model of Neocortical Epilepsy, *Scientific Reports* 9(1) (2019) 5236.
- [266] C.H. Cho, New mechanism for glutamate hypothesis in epilepsy, *Front Cell Neurosci* 7 (2013) 127.
- [267] S. Kim, T. Callier, S.J. Bensmaia, A computational model that predicts behavioral sensitivity to intracortical microstimulation, *J Neural Eng* 14(1) (2017) 016012.
- [268] M. Deprez, K. Luyck, L. Luyten, T. Tambuyzer, B. Nuttin, M. Mc Laughlin, An evaluation of the effect of pulse-shape on grey and white matter stimulation in the rat brain, *Scientific Reports* 8(1) (2018) 752.
- [269] Y. Huang, B. Hajnal, L. Entz, D. Fabó, J.L. Herrero, A.D. Mehta, C.J. Keller, Intracortical Dynamics Underlying Repetitive Stimulation Predicts Changes in Network Connectivity, *J Neurosci* 39(31) (2019) 6122-6135.
- [270] A.P. Yadav, S. Li, M.O. Krucoff, M.A. Lebedev, M.M. Abd-El-Barr, M.A.L. Nicolelis, Generating Artificial Sensations with Spinal Cord Stimulation in Primates and Rodents, *bioRxiv* (2020) 2020.05.09.085647.
- [271] X. Wei, L. Luan, Z. Zhao, X. Li, H. Zhu, O. Potnis, C. Xie, Nanofabricated Ultraflexible Electrode Arrays for High-Density Intracortical Recording, *Advanced Science* 5(6) (2018) 1700625.
- [272] S.S. Mehta, *Commercializing successful biomedical technologies: basic principles for the development of drugs, diagnostics and devices*, Cambridge University Press 2008.
- [273] C.L. Pulliam, S.R. Stanslaski, T.J. Denison, Industrial perspectives on brain-computer interface technology, *Handbook of Clinical Neurology*, Elsevier 2020, pp. 341-352.
- [274] F.G. Rathjen, M. Schachner, Immunocytological and biochemical characterization of a new neuronal cell surface component (L1 antigen) which is involved in cell adhesion, *The EMBO journal* 3(1) (1984) 1-10.
- [275] K. Webb, E. Budko, T.J. Neuberger, S. Chen, M. Schachner, P.A. Tresco, Substrate-bound human recombinant L1 selectively promotes neuronal attachment and outgrowth in the presence of astrocytes and fibroblasts, *Biomaterials* 22(10) (2001) 1017-1028.

- [276] C.L. Kolarcik, D. Bourbeau, E. Azemi, E. Rost, L. Zhang, C.F. Lagenaur, D.J. Weber, X.T. Cui, In vivo effects of L1 coating on inflammation and neuronal health at the electrode–tissue interface in rat spinal cord and dorsal root ganglion, *Acta biomaterialia* 8(10) (2012) 3561-3575.
- [277] J.R. Eles, A.L. Vazquez, N.R. Snyder, C. Lagenaur, M.C. Murphy, T.D. Kozai, X.T. Cui, Neuroadhesive L1 coating attenuates acute microglial attachment to neural electrodes as revealed by live two-photon microscopy, *Biomaterials* 113 (2017) 279-292.
- [278] J. Emerit, M. Edeas, F. Bricaire, Neurodegenerative diseases and oxidative stress, *Biomedicine & pharmacotherapy* 58(1) (2004) 39-46.
- [279] C.A. Piantadosi, J. Zhang, Mitochondrial generation of reactive oxygen species after brain ischemia in the rat, *Stroke* 27(2) (1996) 327-332.
- [280] X.S. Zheng, N.R. Snyder, K. Woeppel, J.H. Barengo, X. Li, J. Eles, C.L. Kolarcik, X.T. Cui, A superoxide scavenging coating for improving tissue response to neural implants, *Acta Biomater* 99 (2019) 72-83.
- [281] C.L. Ballestrasse, R.T. Ruggeri, T.R. Beck, Calculations of the pH changes produced in body tissue by a spherical stimulation electrode, *Annals of biomedical engineering* 13(5) (1985) 405-424.
- [282] L. Peruzzotti-Jametti, M. Cambiaghi, M. Bacigaluppi, M. Gallizioli, E. Gaude, S. Mari, S. Sandrone, M. Corsi, L. Teneud, G. Comi, Safety and efficacy of transcranial direct current stimulation in acute experimental ischemic stroke, *Stroke* 44(11) (2013) 3166-3174.